2011-05-09

Volumetric Analysis of Brain MRI for Alzheimer’s Disease

Qian Shen
University of Miami, qshen624@gmail.com

Recommended Citation
Shen, Qian, "Volumetric Analysis of Brain MRI for Alzheimer’s Disease" (2011). *Open Access Dissertations*. 526.
https://scholarlyrepository.miami.edu/oa_dissertations/526

UNIVERSITY OF MIAMI

VOLUMETRIC ANALYSIS OF BRAIN MRI FOR ALZHEIMER'S DISEASE

By

Qian Shen

A DISSERTATION

Submitted to the Faculty
of the University of Miami
in partial fulfillment of the requirements for
the degree of Doctor of Philosophy

Coral Gables, Florida

May 2011

UNIVERSITY OF MIAMI

A dissertation submitted in partial fulfillment of
the requirements for the degree of
Doctor of Philosophy

VOLUMETRIC ANALYSIS OF BRAIN MRI FOR ALZHEIMER'S DISEASE

Qian Shen

Approved:

Weizhao Zhao, Ph.D. Professor of Biomedical Engineering	Terri A. Scandura, Ph.D. Dean of the Graduate School
Özcan Özdamar, Ph.D. Professor of Biomedical Engineering	Jorge E. Bohórquez, Ph.D. Professor of Biomedical Engineering
Ranjan Duara, M.D. Medical Director of Wien Center Mount Sinai Medical Center	Mohamed Abdel-Mottaleb, Ph.D. Professor of Electrical and Computer Engineering

SHEN, QIAN (Ph.D., Biomedical Engineering)
Volumetric Analysis of Brain MRI for Alzheimer's Disease (May 2011)

Abstract of a dissertation at the University of Miami.

Dissertation supervised by Professor Weizhao Zhao.
No. of pages in text. (124)

Alzheimer's disease (AD), the most common cause of dementia in the elderly, is a gradually progressive degenerative neurological disorder that is characterized by increasing cognitive impairment, characteristic degenerative pathology and brain atrophy. Studies have shown that the progression of AD pathology in the brain develops in a predictable pattern and the pathological changes that take place in brain begin at the microscopic level long before the first signs of memory loss. Structural Magnetic Resonance Imaging (MRI), which has exceptional soft tissue contrast and detailed resolution, is the best way to noninvasively examine changes which occur early in the course of AD. For this dissertation, our aim is to improve the methods for measuring the atrophy of brain structures in AD, as seen on MRI, and to apply these methods to subjects with cognitive impairment.

This study has established a new coordinate template to replace the widely used Montreal Neurological Institute (MNI) template for the atlas-based segmentation procedure. The new template was derived from the same structural image as the one used by the Automated Anatomical Labeling (AAL) procedure. The agreement of the newly

developed coordinate template and AAL helps to estimate accurate spatial transformation parameters used in warping the AAL to individual subject images. The new template combines the spatial information of the structural image and the frequency information of MNI template. Based on the same principle, a set of customized templates has been developed. The customized template, associated atlas and customized priors match more closely the aging population than the previous template, so as to improve the atlas-based segmentation of regions of interest in AD assessment.

Visual Rating System (VRS) of a single coronal slice (MB slice) in MRI has been another valuable method in the assessment of medial temporal lobe atrophy. An automated procedure has been developed in this study to measure the hippocampal area on the same coronal slice so that the labor of human experts in the VRS assessment of hippocampus will be significantly reduced.

Finally the methods and materials (template and atlas) developed in this dissertation were applied to cross-sectional studies of subjects with cognitive impairment. We conducted volumetric analysis on subjects and conclude that the data from the new approaches have higher correlations with clinical data, and therefore can be reliably used as part of an AD assessment tool.

ACKNOWLEDGMENT

I would like to express my deepest respect and gratitude to my advisor, Professor Weizhao Zhao, for giving me the opportunity to start my Ph.D. program in his laboratory and for his continued support, guidance, encouragement and patience throughout my Ph.D. study at the University of Miami.

I also want to convey thanks to my internship supervisor and research collaborator, Dr. Ranjan Duara, for allowing me to work at the Wien Center for Alzheimer's Disease and Memory Disorders, Mount Sinai Medical Center, and from whom I have learned a lot about Alzheimer's Disease and human brain anatomy. Without him this study would not have been possible.

I am also grateful to Professor Jorge E. Bohorquez for teaching me LabView and for cheering me on and inspiring me with his enthusiasm when I felt overwhelmed.

I also wish to thank Professor Özcan Özdamar and Professor Mohamed Abdel-Mottaleb for their suggestions and comments during the preparation of this dissertation.

Thanks to my fellow Ph.D. students Ta-Cheng Chang, Tai Yi Yuan, and Decho Surangsrirat for all the helpful discussions, fun times and activities. I have no doubt you will succeed in all you undertake.

I would like to thank the members of the Wien Center for Alzheimer's Disease and Memory Disorders at Mount Sinai Medical Center: Warren Barker, Elizabeth Potter, Yirah Ochoa, Isael Santos, Maria Greig-Custo, Celeste Ramirez, Joscelyn Agron, and Daisy Wendy Acevedo. You are all so nice to me and it has been a pleasure working with all of you in a friendly atmosphere. I owe a tremendous debt of gratitude to Warren

Barker for teaching me how to use statistical analysis tools and for doing the English proof-reading of my dissertation.

Finally, I would like to extend my deepest grateful to my parents, my husband, Tao, and my daughter, Qiqi, for their unconditional support. Without their constant love, understanding and encouragement, it would have been impossible to finish this study.

TABLE OF CONTENTS

1 Introduction

2 Development of a New Coordinate Template

3 Development of a Custom Elderly Template Set – Template E Set

4 Development of an Automated Area Measure on a Single Coronal Slice

5 Clinical Application of Cognitive Impairment

LIST OF FIGURES

LIST OF TABLES

LIST OF ABBREVIATIONS

AAL	Automated Anatomical Labeling
AC	Anterior Commissure
aCC	Anterior Border of Corpus Callosum
AD	Alzheimer’s Disease
aMCI	amnestic MCI
AMG	Amygdala
ADRDA	Alzheimer's Disease and Related Disorder Association
ApoE	Apolipoprotein E
APP	Amyloid Precursor protein
ART	Automatic Registration Toolbox
AUC	Area Under the Curve for the receiver operator characteristics
CDR-sb	Clinical Dementia Rating – “sum of boxes”
CSF	Cerebrospinal Fluid
CT	Computed Tomography
EM	Expectation-Maximization
ERC	Entorhinal Cortices
FDA	Food and Drug Administration
FLIRT	Affine Inter-Modal Image Registration
fMRI	functional MRI positron emitting tomography
FTLD	Fronto-temporal Lobar Dementia
FWHM	Full Width at Half Maximum
GM	Gray Matter
HPC	Hippocampal cortex or Hippocampus
IBASPM	Individual Brain Atlases using Statistical Parametric Mapping
MB	Mammillary Bodies
MCI	Mild Cognitive Impairment
MMSE	Mini Mental State Examination
MNI	Montreal Neurological Institute
MRI	Magnetic Resonance Imaging
MTA	Medial Temporal Lobe Atrophy

MTL	Medial Temporal Lobe
naMCI	nonamnestic Mild Cognitive Impairment
NCI	No Cognitive Impairment
NFTs	Neurofibrillary Tangles
NINDS	National Institute of Neurological and Communicative Disorders and Stroke
PC	Posterior Commissure
pCC	Post border of Corpus Callosum
PET	Positron Emission Tomography
PiB	Pittsburgh Compound-B
PRC	Perirhinal Cortices
RHPA	Ratio of Hippocampal Area
ROC	Receiver Operator Characteristics
ROI	Regions of Interest
SPECT	Single Photon Emission Computed Tomography
SPM	Statistical Parametric Mapping
SPs	Senile Plaques
VBM	Voxel-based Morphometry
VRS	Visual Rating System
WM	White Matter

Chapter 1 Introduction

1.1 Dementia, AD and MCI

Dementia is a clinical syndrome characterized by "a global deterioration of mental functioning in its cognitive, emotional and cognitive aspects" (Mayer-Gross *et al.*, 1969). It is a major health problem, particularly in the elderly. Alzheimer's disease (AD) is the most common cause of dementia in the elderly population. There are many other causes of dementia, such as cerebro-vascular disease, Lewy body disease, Parkinson's disease, frontotemporal dementia syndromes, alcoholism and prion diseases (e.g., mad cow disease). The first clinical description of Alzheimer's diseases was reported in 1906 by German psychiatrist Alois Alzheimer. He had provided care for a 51 year old woman, Auguste Deter, who had shown a progressive decline in cognitive function, disorientation, aphasia, delusions, and psychosocial incompetence. She died within five years after the onset of illness and Alois Alzheimer examined her brain and observed unusual senile plaques (SPs) and neurofibrillary tangles (NFTs), which remain the pathological hallmarks of the disease and are used to this day to confirm the diagnosis. Although Alzheimer was the first to recognize the clinicopatholgical features of the disease, Alzheimer's colleague Emil Kraepelin introduced the disease as Alzheimer's disease in the category of presenile dementias in the 1910 edition of his textbook (Kraepelin, 1910). Scientists now believe that Auguste Deter had a rare genetic mutation, identified in Volga Germans in the 1990s, that can cause Alzheimer's disease at an early age.

Alzheimer's disease, is the most common cause of dementia among people 65 years and older. The prevalence of AD is expected to increase dramatically as populations around the globe continue to age. According to the Center for Strategic and International Studies' 2003 Aging Vulnerability Index, "Ten years ago, global aging barely registered as a policy issue. Today, with the retirement of the large post–war baby-boom generations looming over the horizon, it is the focus of growing concern among political and policy leaders worldwide" (http://www.csis.org/media/csis/pubs/aging_index.pdf). A new report from the Alzheimer's Association shows that the number of Americans age 65 and older who have Alzheimer's disease will increase from 5.1 million today to 13.5 million by mid-century and the cumulative costs of care for people with Alzheimer's from 2010 to 2050 will exceed $20 trillion, in today's dollars (http://www.alz.org). These demographic changes speak to the importance of early detection and accurate diagnosis of Alzheimer's disease, allowing intervention in the incipient phase of the disease.

AD is a progressive neurodegenerative disorder, whose first symptoms usually include deficits in recent or short-term memory. Subsequently, other cognitive domains, such as language, orientation, judgment and long-term memory are affected. Behavioral problems such as social withdrawal, agitation and delusions increase and most patients eventually require total care. The disease eventually contributes to death (Fradinger and Bitan, 2005). The diagnosis of AD usually involves clinical assessments, cognitive tests, and a brain scan. The average AD patient lives eight to ten years after the onset of illness. Survival can range from three to 20 years, depending on age and other health conditions. The disease has a major effect on the quality of life of patients, as well as the quality of life of family members and caregivers. Early and accurate diagnosis of AD can help patients delay decline in functioning for months to years and to be more involved in treatments and decisions, such as when to stop driving and where to live. Thus, there is a great need for new diagnostic tools for earlier and more accurate detection of AD.

1.1.1. Neuropathology of AD

It is known that neuropathological changes of Alzheimer's disease may be present years or even decades before the onset of the clinical manifestations of the disease. Cognitive and functional reserve capacity, genetic factors and medical (especially cerebrovascular) co-morbidity may determine when the symptoms and functional impairment associated with AD are clinically manifest. As demonstrated in Figure 1.1 below, AD is characterized pathologically by the presence of abundant extracellular β amyloid (Aβ) neuritic plaques and intracellular neurofibrillary tangles (NFTs) (Khachaturian, 1985; Braak and Braak, 1991; Mirra *et al.*, 1991).

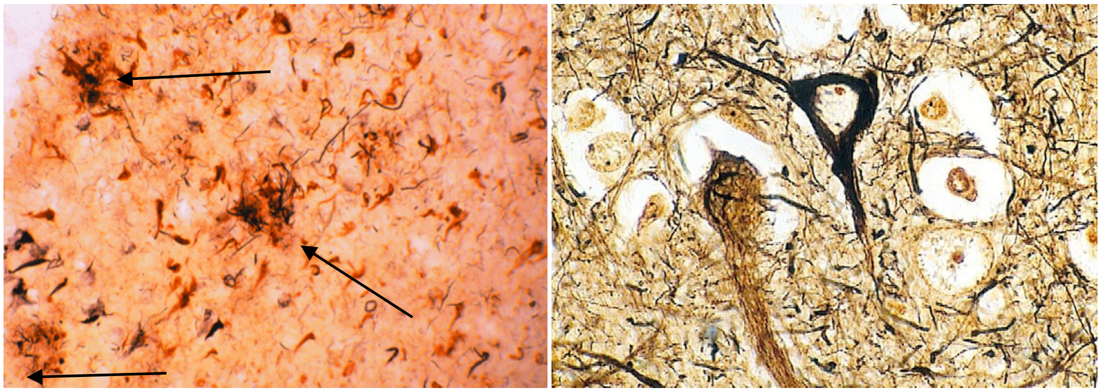

Figure 1.1 Neuropathology of AD. Large extracellular amyloid plaques (left, McGeer *et al.*) and dense intracellular neurofibrillary tangles (right) are well-known histological indicators of Alzheimer's disease. The figure on the right shows a dark black neurofibrillary tangle stained with Bielschowsky silver stain.

Six stages of disease propagation can be distinguished with respect to the location of the NFTs as shown in Figure 1.2 below: "transentorhinal stages I-II: clinically silent cases; limbic stages III-IV: incipient Alzheimer's disease; neocortical stages V-VI: fully developed Alzheimer's disease" (Braak and Braak, 1995).

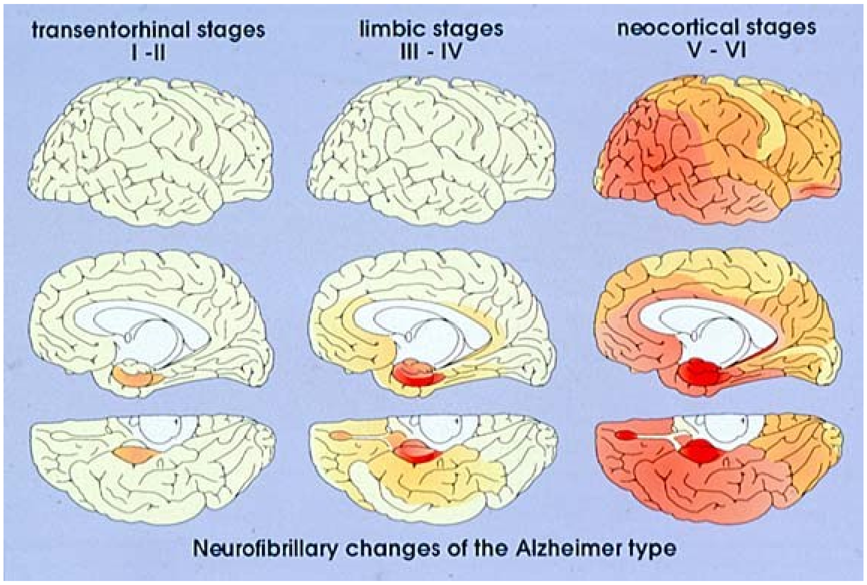

Figure 1.2 Stages of Alzheimer’s Disease

1.1.2. Clinico - Pathological Correlations in AD

Current criteria for the diagnosis of AD require the presence of a clinical syndrome. However, it is evident that the pathology of AD must pre-date the appearance of the clinical features, much like atherosclerosis pre-dates a diagnosis of ischemic heart disease. Indeed, many studies have shown that the pathological changes of AD may begin many years before the patient is diagnosed with dementia (Braak and Braak, 1997; Crystal *et al.*, 1988; Silverman *et al.*, 1997). Among elderly clinically normal individuals who have been classified pathologically as Braak and Braak stage II or less, amyloid or diffuse plaques are frequently present, but neuritic plaques are rare. Subjects diagnosed with Mild Cognitive Impairment (MCI, a condition characterized by subtle cogntive deficits) during life have greater tau and neurofibrillary pathology (which correlates closely with cognitive function), but cortical plaque densities that are similar to that in patients with AD. Although AD pathology is almost universally present among subjects classified clinically to have MCI, about 30% also have other pathologies, such as Lewy bodies, argyrophillic grain disease or hippocampal sclerosis affecting the medial temporal lobe.

On the other hand, about 30% of individuals who meet neuropathologic criteria for AD, and are classified as Braak and Braak stage V or VI at autopsy, remain non-demented during life (Snowdon *et al.*, 1997). This suggests that the disease can reach a relatively advanced pathological stage, without significant symptomatology in some people. Factors that may modify the onset of the clinical manifestations of AD include cognitive reserve capacity, which is generally measured by educational and occupational achievement (Stern, 2003; Stern *et al.*, 1994; Manly *et al.*, 2003; Schofield *et al.*, 1995; Mortimer *et al.*, 2003; Graves *et al.*, 1996), the presence and severity of co-existing cerebrovascular (Tatemichi *et al.*, 1994; Schneider *et al.*, 2004; Snowdon *et al.*, 1997), degenerative and other diseases of the brain, and systemic diseases, such as hypertension, congestive heart failiure and diabetes mellitus (even borderline diabetes) (Xu *et al.* 2007). Appropriate treatment of various conditions, such as hypertension, diabetes mellitus, hyperlipidemia and obesity, as well as an optimal diet and level of physical, social and cognitive activities may determine when and if Alzheimer's disease becomes clinically apparent during life in an individual harboring the pathology of AD (Pope *et al.*, 2003; Graves, 2004).

1.1.3. Clinical Diagnosis of AD

Established Criteria for the Diagnosis of AD

Currently, the most widely used clinical criteria for the diagnosis of AD are the National Institute of Neurological and Communicative Disorders and Stroke-Alzheimer's Disease and Related Disorder Association (NINDS-ADRDA) Criteria (McKhann *et al.*, 1984).

NINCDS-ADRDA criteria have been found to have high sensitivity (range 0.81 to 0.98), but relatively low specificity (range 0.41 to .84), against a histopathological diagnosis (Kukull *et al.*, 1990; Nagy *et al.*, 1998; Gold *et al.*, 1994). A computerized application of NINCDS-ADRDA criteria has been found to have significantly improved specificity, with equivalent sensitivity, as compared to the standard consensus diagnosis system (Hogervorst *et al.*, 2003).

Major advances have occurred in understanding the epidemiology, genetics and the biological basis of Alzheimer's disease since 1984, when NINCDS-ADRDA criteria for AD were developed. Numerous cross-sectional and longitudinal studies, especially those that included clinico-pathological confirmation of the diagnosis, have improved our knowledge of the clinical features and the differential diagnosis of Alzheimer's disease. The current generation of neuropsychological tests can detect impairment in recent memory with much greater sensitivity than in the past (Duara *et al.*, 2010). The discovery of several genetic risk factors for AD, especially the Apolipoprotein E (ApoE) ε4 genotype, are likely to improve the accuracy of the diagnosis of AD, by identifying those who are at higher risk for the disease. The use of brain imaging and cerebrospinal fluid (CSF) biomarkers, that are surrogates for AD pathology, should furher enhance the likelihood that an earlier and more specific clinical diagnosis of AD can be made.

Pre-Dementia and Pre-Alzheimer Syndromes and Mild Cognitive Impairment (MCI)

An earlier diagnosis of AD can only be achieved by lowering the thresholds of cognitive and functional impairments currently required for a diagnosis of AD. A transitional, pre-dementia state, between normal cognition and established dementia is likely to exist for most recognizable dementing diseases. A number of studies have suggested that impairment of recent memory may be the best cognitive biomarker of AD in its pre-dementia state (Grober *et al.*, 2000; Howieson *et al.*, 1997; Small *et al.*, 2003; Duara *et al.*, 2010), even among asymptomatic, community-dwelling elders (Assal and Cummings, 2002). The accuracy of the diagnosis of early AD is likely to depend on the severity of cognitive impairment, especially in the memory domain. Although memory-related symptoms are by far the most common presentation of early AD, variations in the onset and progression of AD are also well known, including an aphasic/anomic, a visual agnosic and a frontal (abulic or disinhibited) onset (Galton *et al.*, 2000). It also remains important to consider pre-dementia conditions other than AD, including Vascular Cognitive Impairment, Lewy Body Disease and various forms of fronto-temporal lobar degeneration.

Cognitive impairment among non-demented elderly individuals may also be caused by a variety of systemic medical conditions, effects of medications and toxins, neuropsychiatric disorders, as well as by the effects of educational and socio-cultural deprivation and “frailty-related” factors.

Mild Cognitive Impairment (MCI) (Petersen *et al.*, 1999; 2003; 2004), which requires impairment in recent memory and a history of decline in cognition, in the face of intact global cognition and functional ability, is a pre-dementia condition that has been shown to have a high likelihood of progression to Probable AD. Based on the clinical presentation, MCI could divided two subtypes: amnestic MCI (aMCI), if the impairment includes the memory domain, and nonamnestic MCI (naMCI), if the impairment is in one or more non memory domains such as attention/executive functioning, language, and visuospatial processing (Kantarci *et al.*, 2008). Patients with the aMCI subtype have a higher risk of progression to AD compared with normal aging or naMCI. Patients with naMCI are likely to have far more variability in terms of symptomatology and progression to various forms of dementia (e.g., frontotemporal dementia, primary progressive aphasia). In clinic cohorts, the annual rate of progression to full-blown AD in patients with MCI is generally reported to be around 15%–20%, meaning that in 3 years about half of the patients with MCI will develop clinical AD (Karas *et al.*, 2008). As strategies to delay disease progression, and possibly prevent or offset the onset of AD are under development, it is extremely important to recognize individuals at high risk for developing AD who may particularly benefit from early therapeutic interventions (Mosconi *et al.*, 2007).

Neuropsychological testing is included in the standard medical workup for AD. Mini-Mental Status Examination (MMSE) is one of the commonly used neuropsychological tests. It offers a brief 30-point questionnaire test that is used to quantify cognitive function and screen for cognitive impairment. This test evaluates the individual's orientation, attention, calculation, recall, language and motor skills. Each section of the test involves a related series of questions or commands. The individual receives one point for each correct answer. A score below 24 usually indicates cognitive impairment. Figure 1.3 demonstrates that progressive declines in the functional abilities that correlate with MMSE scores during the clinical course of AD (Petrella *et al.*, 2003).

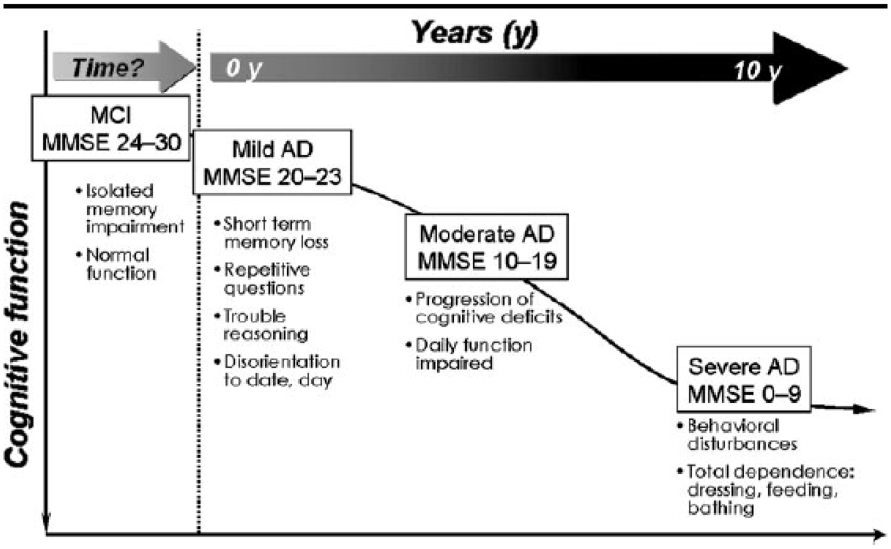

Figure 1.3 Demonstration of the progressive declines in the functional abilities correlate with MMSE scores during the clinical course of AD. MCI (mild cognitive impairment) is coined to describe the transitional phase between normal aging and AD. (Petrella *et al.*, 2003)

Another commonly used scale for evaluation of staging severity of dementia is Clinical Dementia Rating (CDR) scale. It was developed primarily for use in persons with dementia of the Alzheimer type (the equivalent of probable AD) and it can also be used to stage dementia in other illnesses as well. It assesses six domains: memory; orientation; judgment and problem-solving; community affairs; home and hobbies; and personal care (Burns *et al.*, 2002). The global CDR score is the weighted average of the category ratings. Ratings are 0 for healthy people, 0.5 for questionable dementia and 1, 2 and 3 for mild, moderate and severe dementia as defined in the CDR scale. The “sum of boxes” scores (CDR-sb) are the sum of the category ratings.

1.1.4. Treatment of AD

There is no cure available for patients suffering from AD. However, careful assessment and the development of comprehensive multidisciplinary care plans to address personal, social, medical and behavioral problems associated with dementia have become the mainstay of treatment and care program for people with AD and their caregivers. For example, common psychosocial issues addressed by clinicians dealing with AD patients are “when to stop driving”, “how to take care of mom”, and “where to live”.

So far, two main types of drugs are currently approved by the Food and Drug Administration (FDA) for use in Alzheimer's. These drugs do not alter the course of disease, but can improve some of the cognitive and behavioral symptoms of AD for several years. Cholinesterase inhibitors temporarily boost the amount of a neurotransmitter important for learning and short-term memory (acetylcholine) in the brain. The most commonly prescribed cholinesterase inhibitors are donepezil (Aricept®), galantamine (Razadyne®) and rivastigmine (Exelon®). The other type of drug for AD works by regulating the activity of glutamate, a messenger chemical involved in all brain function, including learning and memory. One such drug, Memantine (Namenda®), is approved only for the treatment of moderate to severe AD.

It is possible that disease-modifying treatments for AD will become available in the near future, providing hope that the disease process will be arrested or reversed, especially if treatment is initiated early. However, it is likely that pharmacological treatment of AD in a pre-dementia stage of the disease (i.e., Prodromal AD) will be approved by the FDA only when a secure diagnosis of AD can be made at this early stage.

1.1.5. Use of Biomarkers for Diagnosis of Prodromal (PreClinical) AD

Biomarker tests that indicate the presence of underlying AD pathology could be used to increase the sensitivity and specificity of the diagnosis of a pre-dementia syndrome, such as MCI.

Neuroimaging assessments of entorhinal cortex volume and hippocampal volume on structural MRI scans are highly correlated with the future rate of progression of MCI to AD. Smaller hippocampal and entorhinal cortical size on MRI (de Leon *et al.*, 1997) has been related to memory impairment in normal aging and future AD risk. The presence of MCI or mild dementia versus normal cognition has been associated specifically with atrophy of the hippocampus, parahippocampal gyrus and amygdala (Bobinski *et al.*, 2000; Jarvenpaa *et al.*, 2004; Salamon *et al.*, 2004). The histopathologics correlate of these imaging findings appears to be the accumulation of neurofibrillary tangles, neuritic plaques and the loss of neurons and dendritic arbor in the transentorhinal cortex, and the hippocampus cortex (Bobinski *et al.*, 2000; Gosche *et al.*, 2001, Jack *et al.*, 2002). The presence of medial temporal atrophy is not specific for AD and conditions, such as Fronto-temporal Lobar Dementia (FTLD), vascular dementia and hippocampal sclerosis may also demonstrate brain atrophy in these regions.

Other imaging techniques, such as positron emission tomography (PET) with radiolabeled [18F]-2-fluoro-deoxy-D-glucose (PET-FDG) may provide additional sensitivity though probably not specificity to the diagnosis of AD. Using FDG-PET, with an automated method of image analysis to study the hippocampus, de Leon and colleagues showed that baseline measurements predicted decline from normal to MCI or AD six to seven years in advance of symptoms with 71% and 81% accuracy, respectively (de Leon *et al.*, 2007). An extrapolation of these results suggests that AD can be identified 12 years before the patient is symptomatic. PET imaging using the amyloid-binding agent Pittsburgh Compound-B (PiB) may provide high sensitivity to early AD pathology, but it may have many false positives; that is, many normal elderly subjects may have a lot of amyloid in their brain and be able to function normally for 10 years or more.

CT (X-ray computerized tomography) is mainly used to rule out treatable causes of dementia that can be treated surgically, such as tumors and hydrocephalus. CT scans can be used to identify enlargement of CSF spaces, lateral ventricles, particularly the temporal horn of the lateral ventricle, and cortical sulci (Lehéricy *et al.*, 2007). Functional MRI (fMRI), a functional imaging technique, can evaluate changes in blood flow in different areas of the brain over time in association with a cognitive task. By using fMRI, Sperling (2007) studied the cognitive–behavioral functions in early phases of neurodegenerative disorders and identified the neuroanatomical networks affected by these diseases (Sperling, 2007). Another study of verbal short-term memory utilizing fMRI reports that alternative recognition mechanisms happens in left parahippocampus and hippocampus (Peters *et al.*, 2009). These studies demonstrate that AD patients have different functional networks for short-term memory processing.

Biomarkers in CSF are related to the pathological hallmarks of AD. Tau proteins in CSF are correlated with the number of neurofibrillary tangles in the brain, and "pathogenic" sections of the amyloid beta peptide ($A\beta_{42}$) in CSF contribute to amyloid plaques in the brain. A marked increase in CSF tau with a marked decrease in CSF $A\beta_{42}$ is found in AD, providing high sensitivity (90%) for the disease (De Meyer *et al.*, 2010). One study showed that 95% of MCI cases with an AD signature on CSF progressed to AD over a four to six year period (Hansson *et al.*, 2006). The high rate of AD CSF biomarkers among normal elderly controls is likely related to preclinical pathology.

The use of neuroimaging and other biomarkers for the diagnosis of presymptomatic disease and for monitoring disease progression has been demonstrated by de Leon et al. among clinic patients. Using MRI and an automated regional boundary shift method, the assessment of medial temporal lobe (MTL) atrophy predicted progression of MCI and AD with an accuracy of 89%. Baseline FDG-PET measurements predicted decline from MCI to AD in 81% of cases. Changes in hippocampal metabolism correctly classify 76% of the future decliners among normal and MCI subjects. Laurent and Dubois (2006) suggested that specific neuropsychological assessments, neuroimaging and biomarkers tests would allow demonstration of the underlying pathological process before AD patients meet the criteria of dementia, thus enabling the subgroup of MCI subjects who had Prodromal AD to be identified.

1.2 Structural MRI in Detection of Atrophy in AD

Alterations occurring in the brain in various neurodegenerative diseases can be detected and quantified by several brain neuroimaging techniques, such as CT, MRI, fMRI, PET and single photon emission computed tomography (SPECT). Neuroimaging has been shown by some to be superior to neuro-psychological tests for early diagnosis of AD (Zamrini *et al.*, 2004).

Structural MRI is the best way to examine changes which occur early in the course of AD in regions such as the hippocampus. It is routinely requested during the clinical work-up diagnosis. MRI scanning is noninvasive, has exceptional soft tissue contrast and detailed resolution which allows the investigation of normal anatomical variability bounds, as well as the quantization of volumetric changes accompanying neurological conditions.

There are two main methods of analyzing MR images, so as to identify regional abnormalities or alterations from a normative group: voxel-based morphometry (VBM) and region of interest methods. VBM uses a statistical method to identify alterations in tissue density on a voxel by voxel basis across the entire brain. No a priori hypothesis is required to identify morphological abnormalities. It treats MRIs as continuous scalar measurements and tests for local differences at the appropriate spatial scale (Ashburner and Friston, 2009). Recent VBM techniques have demonstrated that the progressive MCI subjects who convert from MCI to clinical AD present not only medial temporal lobe but also widespread neocortical atrophy compared to the cognitively stable MCI subjects (Jack *et al.*, 2008; Fan *et al.*, 2008). Although VBM has shown new possibilities in the early identification of subjects with MCI, it does not provide single-subject level information which would be clinically important. In addition, the currently used segmentation algorithms in VBM are not particularly adept in taking into account the partial volume effect when classifying the voxels into different tissue types. As a result, there may be voxel intensity changes which may lead to erroneous tissue classification results (Julkunen, *et al.*, 2009).

Visual rating method and volumetric analysis are two widely used ROI analytic methods. Visual rating methods allow assessment of regional atrophy on one or more standard coronal slices in an MR scan (Scheltens *et al.*, 1995, Urs, 2006, Duara *et al.*, 2008, Urs *et al.*, 2009). It is simple to use and very practical for clinical application. Studies by Urs *et al.* (Urs, 2006, Duara *et al.*, 2008, Urs *et al.*, 2009) have demonstrated that visual rating of just one standard coronal slice in an MR scan provides semiquantitative measures which nevertheless have been shown to have high sensitivity and specificity for distinguishing patients with AD from those with no cognitive impairment, and similar sensitivity and specificity levels have been obtained for diagnosing aMCI (Urs, 2006, Duara *et al.*, 2008, Urs *et al.*, 2009).

Volumetric methods are quantitative and have been used to demonstrate significant reductions in volumes of specific medial temporal lobe structures, such as the hippocampus and amygdala among cognitive diagnostic groups (e.g. cognitive normal versus AD) (Barnes *et al.*, 2006; den Heijer *et al.*, 2006; Basso *et al.*, 2006). Because they provide regional brain volumes, they allow comparisons of volume changes in different pathological states or changes in regional volumes longitudinally (Ishii *et al.*, 2006). Manual outlining of ROIs for volumetric analysis is currently considered to be the gold standard method, although it is time consuming, very labor intensive and may have high intra and inter-rater variability in measurement. Further, a high level of training is required for manual tracing methods. Also, the definition of the boundary of the hippocampus has varied between studies, so there is an effort to use consistent anatomical landmarks among Alzheimer's researchers (http://www.hippocampal-protocol.net/public/file/jack-protocol.pdf). As a result, automatic delineation techniques have been developed and validated in AD related studies (Morey *et al.*, 2009; Carmichael *et al.*, 2005; Tae *et al.*, 2008; van der Lijn *et al.*, 2008; Rodionov *et al.*, 2009). However, there is still room for improvement. More accuracy in automatic delineation results in more accuracy of volumetric measurement.

1.2.1 Visual Rating Methods

The goal for the visual rating methods is to achieve an accurate and reliable assessment using a human "expert" rater. Scheltens *et al.* (1995) initially demonstrated that visual rating methods could be helpful in distinguishing early AD subjects from those with no cognitive impairment (NCI), and it also predicted which subjects would convert from MCI to AD (Scheltens *et al.*, 1995). The visual rating scale developed by Scheltens *et al.* was used to assess medial temporal lobe atrophy on six coronal slices of MRI parallel to the brainstem axis. The score is assigned based on visual rating of the width of the choroid fissure, width of the temporal horn, and height of the hippocampal formation. The resulting scores are 0=absent, 1=minimal, 2=mild, 3=moderate, and 4=severe medial temporal lobe atrophy.

Visual rating system (VRS) software developed at the Wien Center for Alzheimer's Diseases and Memory Disorders in Mount Sinai Medical Center (Miami Beach, Florida) expands the scope and utility of the Scheltens method, as well as a method of standardization of the ratings of atrophy in the entorhinal and perirhinal cortices (ERC and PRC) and hippocampus (HPC) structures of the medial temporal lobe (Urs, 2006; Duara *et al.*, 2008, Urs *et al.*, 2009). These regions are clearly outlined in Figure 1.4 (below) on a coronal section of the brain, demonstrating the anatomy of this region and the relative ease with which the landmarks for these brain regions can be used to demarcate the structures of interest for distinguishing the earliest changes that occur in neurodegenerative diseases. Ratings are based on a five point scale, with “0” signifying no atrophy, and “4” signifying the most severe atrophy (see Figure 1.5). Medial temporal lobe atrophy (MTA) ratings for each hemisphere are calculated by summing the ratings for the HPC, ERC and PRC on each side. A library of reference images that defines the anatomical boundaries of each brain structure and depicts different levels of atrophy are provided from a drop-down menu in the system interface; this facilitates a direct comparison of each structure on the subject's MRI. VRS enables digital entry of atrophy ratings that are automatically saved to an Excel file. It has been tested with excellent inter-rater (kappa, 0.75 to 0.94) and intra-rater (kappa, 0.84 to 0.94) reliabilities for VRS ratings of atrophy in the HPC, ERC, and PRC (Urs *et al.*, 2009). It has also been shown to have high sensitivity and specificity for distinguishing patients with AD from those with no cognitive impairment, and similar sensitivity and specificity levels for patients with aMCI (Urs, 2006; Duara *et al.*, 2008, Urs *et al.*, 2009). The coronal slice used for rating the hippocampus is standardized by using the mammillary bodies (an easily visualized structure which has constant relationships to the medial temporal regions that show atrophy early in the AD disease process. Using the mammillary bodies (MB) slice also ensures that the only the anterior aspects of these medial temporal structures are rated.

VRS-MTA has been further validated in several studies in which VRS was compared to APOE ε4 (genetic risk factors for AD) genotype frequency, global cognitive scores and memory scores (Urs, 2006; Duara *et al.*, 2008, Urs *et al.*, 2009). Thus far, VRS-MTA scores have performed about the same as volumetric measures of the hippocampus for distinguishing diagnostic groups (Shen *et al.*, 2011a). Further, VRS-MTA is user-friendly, easily operates on a PC or radiology console, and does not require special technical support, which is a major obstacle in the routine use of volumetric methods. Also image artifacts, including those resulting from patient movement or aberrant positioning, have a much smaller impact on VRS-MTA ratings than on volumetric methods. These advantages allow VRS-MTA to be easily adopted for the clinical diagnostic tests.

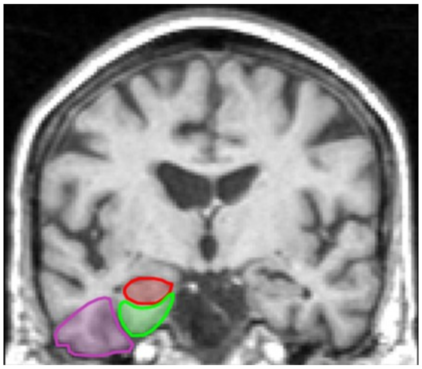

Figure 1.4 Medial Temporal Anatomy. Hippocampus (HPC) is red; Entorhinal Cortex (ERC) is in green and Perirhinal Cortex (PRC) is in purple.

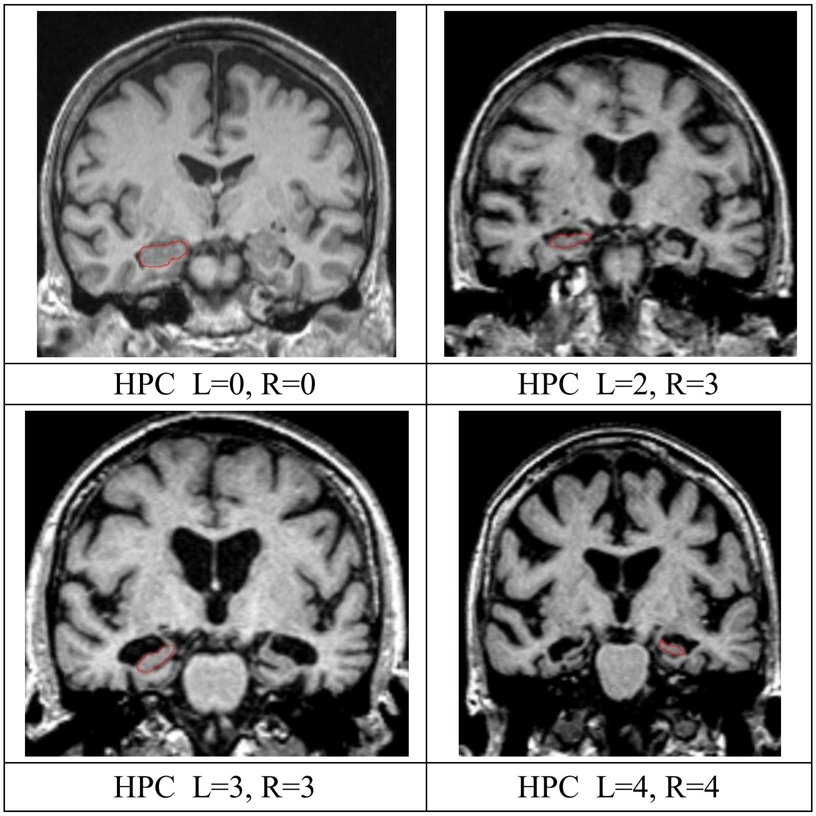

HPC L=0, R=0

HPC L=2, R=3

HPC L=3, R=3

HPC L=4, R=4

Figure 1.5 An illustration of the different levels of atrophy of the hippocampal cortex (HPC), outlined in red, that is a recognizable “signature” of the atrophy associated with AD pathology. Atrophy Grades are: 0= no atrophy; 1=Minimal atrophy; 2=Mild atrophy; 3=Moderate atrophy; 4= Severe atrophy

VRS Visual rating scales, although simple to use, making them practical for clinical application, were not designed to detect atrophy progression on serial imaging; their quantized nature makes them insensitive to change over time. A technique that combines the simplicity of visual rating scales and the ability of volumetric measurement to track disease progression would be desirable.

1.2.2 Volumetric Analysis

Volumetric analyses of brain structures have become increasingly common for diagnostic purposes and for identifying disease progression. It has been demonstrated that atrophy of the MTL memory structures, where the pathological changes of AD in terms of neurofibrillary tangles and neuronal loss first occur (Braak and Braak, 1991; Kordower *et al.*, 2001), can be detected even in subjects with MCI (De Santi *et al.*, 2001; Du *et al.*, 2007; Pennanen *et al.*, 2004). Atrophy of the MTL structures has also been claimed to predict the conversion from MCI to clinical AD (Uotani *et al.*, 2006; Tapiola *et al.*, 2008; Jack *et al.*, 2004).

Some previous volumetric studies of hippocampus and amygdala are shown in Table 1.1. Most of these studies are about AD or MCI verse normal control, few are about depression, Lewy body dementia or vascular dementia, which we include here, because those references are comparing the manual segment with the automated segment of hippocampus and amygdala. These listed studies shown that the significant volume loss of hippocampus and amygdale for people with AD (de Jong *et al.*, 2008; Colliot, *et al.*, 2008 Teipel *et al.*, 2006; Müller *et al.*, 2005) and volumes of the medial temporal structures correlated with memory performance (Mori *et al.*, 1997). Also, most of the listed studies in Table 1.1 demonstrated that the automated segments were high agreement with manually segments (Morey *et al.*, 2009; Ishii *et al.*, 2006; Leung *et al.*, 2010), though Tae *et al.*, (2008), Firbank *et al.* (2008) shown the automated segments were not very accuracy comparing with manually segments.

In order to obtain the volumetric measurements for various structures, accurate regional segmentation on MR images is necessary. The segmentation of an image into a number of different and disjoint sets of voxels that correspond to anatomically meaningful regions is a challenging task, due to the poor definition of regional boundaries on MRI scans, such as the cortical structures, hippocampus, amygdale, thalamus, putamen, etc. Signal intensity alone is not sufficient to distinguish between different cortical grey matter structures as observed and characterized by Fischl *et al.* (2002).

Attempts have been made to improve the methodology of segmentation of brain MRI. The simplest is slice by slice manual delineation. It has been used for hippocampus and amygdala volumetric studies (Barnes *et al.*, 2006; den Heijer *et al.*, 2006; Basso *et al.*, 2006). This operator-dependent approach is very time consuming, requires expert neuroanatomical knowledge and high inter-operator reliability. Currently, it is still being used mainly as a “gold-standard” for evaluation of segmentation methods. Semi-automated segmentation methods reduce manual labor by having an operator provide landmarks (Colliot *et al.*, 2008), seed-points or bounding boxes (Chupin *et al.*, 2007) to initiate or constrain a subsequent automated segmentation process. However, for a large-scale study with many subjects, manual delineation may not be feasible. As a result, much research effort has been devoted to fully automated segmentation. Automated atlas-based segmentation (also called label propagation) is one commonly used approach and it has given promising results in the volumetric analysis of AD or MCI atrophy. (Morey *et* *al.*, 2009; Carmichael *et al.*, 2005; Tae *et al.*, 2008; van der Lijn *et al.*, 2008; Rodionov *et al.*, 2009).

Atlas-based Segmentation in Volumetric Analysis

By using this method, prior knowledge is introduced through an anatomical structural atlas created by neuroanatomical experts who manually delineates the brain structures of interest. Then the labeling of the anatomical atlas is subsequently "warped" to the to-be-segmented images to delineate the labeling of the to-be-segmented images. In this approach, a spatial registration is employed to obtain the information on the magnitude and direction required to transform a point in the anatomical atlas to the appropriate point in the to-be-segmented brain images.

Two factors may influence the performance of this approach: the way the atlas is created and the registration algorithm for estimating the spatial registration parameters used to deform the atlas labels to the to-be segment images.

Atlas in Atlas-based Segmentation

The neuroanatomical atlas used in this standard approach is typically created by manually delineating the region of interest in a single subject image in the standard space (Haller *et al.*, 1997; Hayashi *et al.* 2009; Tae *et al.*, 2008; García-Vázquez *et al.*, 2008; Seixas *et al.*, 2010). However, if the single subject is not representative of the investigated population, the accuracy of the segmentation may be reduced (Carmichael *et al.*, 2005). A possible solution to this problem is to use multiple atlases, or an atlas which contain probabilistic information from multiple templates. (Fischl *et al.*, 2002)

Table 1.1 Some volumetric studies' results of hippocampus and amygdala

Author	Methods	Age means ± SD	Diagnosis	Right HPC means ± SD	Left HPC means ± SD	Total HPC means ± SD	Right AMG means ± SD	Left AMG means ± SD	Total AMG means ± SD	Results
de Jong *et al.*, 2008	Automated Software: FIRST	65±13(M)	Memory Complainers	4.21±0.71 (M)	4.20±0.60 (M)		1.72±0.28 (M)	1.66±0.28 (F)		Hippocampus, putamen and thalamus of probable Alzheimer's disease subjects are significantly smaller than those of memory complainers. The volume of the left hippocampus correlates significantly to the MMSE score
		67±12(F)		3.97±0.72 (F)	3.83±0.74 (F)		1.47±0.26 (F)	1.44±0.22 (F)		
	Automated Software: FIRST	76±5.8(M)	Probable AD	3.57±0.78 (M)	3.73±0.67 (M)		1.57±0.32 (M)	1.67±0.35 (F)		
		77±8.2(F)		3.32±0.65 (F)	3.43±0.69 (F)		1.48±0.37 (F)	1.36±0.27 (F)		
Tae *et al.*, 2008	Manually traced	41.9±10.3	Controls	2.87±0.28	2.81±0.23					Automated methods could detect hippocampal atrophy in the patients with depression. Volume measured using FreeSurfer was agreement with manual hippocampal volumetry, though 35% larger. Volume measured using IBASPM was was questionable with manual hippocampal volumetry.
	Automated Software: FreeSufer	41.9±10.3	Controls	4.02±0.41	3.80±0.33					
	Automated Software: IBASPM	41.9±10.3	Controls	2.98±0.36	3.46±0.39					
	Manually traced	41.7±11	Depression	2.87±0.28	2.81±0.23					
Mori *et al.*, 1997	Semi-automatic	70.3±7.1	Controls	2.41±0.23	2.22±0.19		1.94±0.17	1.76±0.13		Volumes of the amygdaloid complex correlated with memory performance.
	Semi-automatic	70.3±7.1	AD	2.03±0.46	1.87±0.36		1.57±0.30	1.43±0.34		
Firbank *et al.*, 2008	Automated Software: SPM	75±6	Lewy body dementia			2.20±0.48				Atlas-based automated segments were agreement with manually segmented of hippocampus, but not very accuracy.
	Automated Software: SPM	75±6	AD			1.62±0.55				
	Automated Software: SPM	60±6	Vascular dementia			1.84±0.23				
	Automated Software: SPM	75±4	Controls			2.88±0.37				

Colliot, *et al.*, 2008	Semi-automatic		Controls			2.86±0.46				Significant hippocampal volume reductions were detected (-32% in AD patients vs controls, *P*< .001; -19% in MCI patients vs controls, *P*<.001; and -15% in AD patients vs MCI patients, *P*< .01). Individual classification on the basis of hippocampal volume resulted in 84% correct classification between AD vs. controls and 73% between MCI vs. controls.
	Semi-automatic		MCI			2.30±0.46				
	Semi-automatic		AD			1.95±0.46				
Morey *et al.*, 2009	Automated Software: FreeSufer	37.2±8.5 (Depression) 37.2±8.5 (Controls)	Depression or Controls			4.19±0.53			1.95±0.27	Compared to manually tracing, automated segmentation using FreeSurfer were outperformance than using FIRST.
	Automated Software: FIRST	37.2±8.5 (Depression) 37.2±8.5 (Controls)	Depression or Controls			4.40±0.73			1.53±0.30	
Ishii *et al.*, 2006	Manually traced	63.4±6.9	AD			3.50±0.79				Atlas-based automated segments using AVSIS (adopted registration function in SPM99) shown great agreement with manually segments
	Manually traced	61.3±5.9	Controls			4.83±0.64				
	Automated Software: AVSIS (adopted SPM99)	63.4±6.9	AD			3.78±0.67				
	Automated Software: AVSIS (adopted SPM99)	61.3±5.9	Controls			5.09±0.55				
	Semi-automatic	63.4±6.9	AD							
	Semi-automatic	61.3±5.9	Controls							
Devanand *et al.*, 2008		73.2±7.1	Converters to AD			3.77±0.72				Hippocampal volume and MRI entorhinal cortex volume. For 10% false positives (90% specificity), this five-predictor combination showed 85.2% sensitivity,
		64.9±9.9	Nonconverters to AD			4.37±0.62				
		65.7±9.3	Controls			4.34±0.57				

Teipel *et al.*, 2006	Manually	65.7±9.4	Controls	3.32±0.54	3.16±0.58					Volumes of medial temporal lobe structures were significantly smaller in AD patients than in controls with exception of the left entorhinal cortex.Diagnostic
	Manually	61.5±8.9	AD	2.24±0.67	2.23±0.64					
Müller*et al.*, 2005	Manually traced	67.3±8.7	MCI	3.21±0.37	2.83±0.34					Left hippocampal volume was significantly lower (-11%, P = 0.02) in MCI patients than in control subjects. No significant differences were found for the right hippocampus (-4%). Mean diffusivity (MD) was significantly elevated in MCI patients vs. controls in left (+10%, P = 0.002) and right hippocampal areas (+13%, P = 0.02).
	Manually traced	66.9±9.0	Controls	3.34±0.48	3.13±0.43					
Babiloni *et al.*, 2009	Manually	67±1.1	MCI			5.6±0.05				Progressive atrophy of hippocampus is related toloss of resting alpha sources in the continuum along MCI and AD conditions.
	Manually	71±1.1	MCI			4.3±0.08				
	Manually	71±1.6	AD			4.2±0.09				
Kramer *et al.*, 2004	Semi-automatic (commercial software)	75.6±7.3	AD			3.5±0.9				Cortical gray matter but not hippocampal volume predicted immediate free recall. In contrast, hippocampal volume was the best predictor of how well information was retained over a delay, even after controlling for levels of immediate recall.
	Semi-automatic (commercial software)	74.5±7.5	Controls			4.6±0.5				
Chaoa *et al.*, 2010	Semi-automatic	67.5±5	Controls	2.33±0.22	2.31±0.20					Analyses revealed significant main group effects for both (*F*2,34 = 7.62, *p* = 0.002) and parahippocampal (*F*2,34 = 3.58, *p* = 0.04) volume.
	Semi-automatic	68.6±7.9	preMCI	2.30±0.34	2.27±0.36					
	Semi-automatic	78.8±7.4	MCI	2.10±0.25	2.03±0.34					
Leung *et al.*, 2010	Manual	82.7±4.3	Controls		2.53±0.53					Multiple-atlas automated segments can distinguished between control, MCI and AD groups
	Manual	76.6±7.1	MCI		2.23±0.34					
	Manual	75.6±7.2	AD		1.90±0.30					
	automatic	82.7±4.3	Controls		2.58±0.63					
	automatic	76.6±7.1	MCI		2.17±0.4					
	automatic	75.6±7.2	AD		1.80±0.22					

Note: unit of volume is cm^3. HPC: Hippocampus; AMG: amygdaloid; M: Male; F: Female;

Heckemann *et al.* (2006) used the result of a single atlas on a to-be-segmented image as a classifier, and the deformed labels were combined with decision fusion (Heckemann *et al.*, 2006). This study of 67 brain structures has shown that using multiple atlases combined with decision fusion better matched the manual segmentations than using single atlas propagations. Barnes *et al.* (2008) used a template library combined with morphological operations (intensity thresholding plus one conditional dilation) in hippocampus segmentation. His results have shown that the relative hippocampal volume change over time can be accurately quantified. Wu *et al.* (2007) used a family of brain template sets for atlas-based segmentation of anterior cingulate cortex and several subcortical structures. For each subject and each region, the template selection method automatically chooses the 'best' template with the highest local registration accuracy, based on normalized mutual information. The results have demonstrated that the template selection method produced higher segment agreement with manual tracings than the single template method. Segmentation methods using multiple atlases were also applied by Klein *et al.* in the automatic segmentation of prostate in 3D MR images. (Klein *et al.*, 2008)

The employment of multiple atlases in atlas-based segmentation has shown outperformance to a single atlas (Barnes *et al.*, 2008). However it also brings additional computational cost because the method involves the registering of several atlases with each of the to-be-segmented images and the processing of decision fusion or atlas selection step.

To encompass the inter-individual variability of investigated subjects, another possibility is to use a probabilistic atlas from a set of images. This technique has been applied to brain tissue, as well as brain structure segmentation (Fischl *et al.*, 2002; Hammers *et al.*, 2007). Once the average atlas has been constructed, the approach on the average atlas requires less computation than the multi-atlas approach. However, because it still relies on a single registration, average atlas segmentation is less accurate than registering multiple atlases (Heckemann *et al.* 2006).

Registration Algorithms in Atlas-based Segmentation

Another possible factor that may influence the performance of atlas-based segmentation approaches is the registration algorithm for estimating the spatial registration parameter, which would be used to deform the atlas labels to the to-be-segmented images.

Some authors have used affine (Carmichael *et al.*, 2005) or piecewise affine (Barnes *et al.*, 2006) registration algorithms. However, in order to achieve precise extraction, typically a high dimensional nonlinear registration algorithm is employed. An increase in degrees of freedom results in more flexibility to adapt the atlas to the target image, but it also increases computational cost and the risk, where the optimization may get stuck in a local minimum that is far away from the optimal solution. Since the similarity is computed over the entire image, atlas-based segmentations are prone to errors that do not have a large effect on this measure.

Much work has been done on the registration algorithms. There are several registration methods that are publicly available online. ANIMAL+INSECT of Collins and Evans (Collins *et al.* 1995, 1999) was one of the earliest automated labeling strategies. ANIMAL registration is a high degrees of freedom (around $6.9\text{x}10^4$) intensity based technique where the similarity measure is a normalized correlation statistic of the intensities within a local neighborhood, the constraint is affected by smoothing the deformation vectors at each iteration, and a multi-resolution scheme is used. Automatic Registration Toolbox (ART) (http://www.nitrc.org/projects/art/) generates around 7×10^6 parameters to describe the deformation field where the similarity measure is also a normalized correlation statistics of the intensities. Affine Inter-Modal Image Registration (FLIRT) employing a linear rigid technique to produce 9 affine transforms parameters. The image registration procedures of Statistical Parametric Mapping (SPM, http://www.fil.ion.ucl.ac.uk/spm/software/spm5/) includes two steps: (1) an affine transform which is a linear approach for finding the best combination of global translation, rotation, and scaling factors and (2) a higher-order (degrees of freedom is around 1200) nonlinear transform for estimating the deformation field at a regional level where the similarity measure is the mean squared difference of the intensities.

IBASPM (Individual Brain Atlases using SPM) (Alemán-Gómez *et al.*, 2006) is the one of the third-party toolboxes of the SPM. It employs the image registration function within the SPM and the Anatomical Automatic Labeling (AAL, Tzourio-Mazoyer *et al.*, 2002) to automatically segment 116 structures of brain. AAL is a predefined anatomical labeling by manually tracing 116 ROIs on an image from a young normal brain. These ROIs include the hippocampus, amygdala and parahippocampus, which are the regions where atrophy initially appears in AD and MCI. Some authors have used IBASPM in neurodegenerate disease studies. The study of Hayashi *et al.* (2009) showed that volumetric measurement using IBASPM can distinguish an AD group from a normal control group. Tae *et al.* (2008) compared the ability of FreeSurfer (Fischl *et al.*, 2002) and IBASPM in detecting hippocampal atrophy of the patients with major depressive disorder. The results indicated that both automated methods can detect hippocampal atrophy and that FreeSurfer is better. However Hasan KM (2009) questioned this results because the authors did not realize that the default atlas AAL of IBASPM is right-left swapped; that may have adversely affected the performance of IBASPM. García-Vázquez V *et al.* (2008) tested the influence of the atlas when segmenting normal and pathologic brains using IBASPM. They showed that overlap ratio and volumetry with manual segmentation were better in healthy controls than in patients. This indicated "that a critical point in the atlas-based automatic segmentation techniques and a possible cause of this difference is the registration to Montreal Neurological Institute T1-weighted template (MNI template), representing normal healthy brains which does not properly represent inter-group variability." Seixas F.Z. (2010) compared FreeSurfer, IBASPM and FSL in volumetric assessment of the hippocampus. They showed that Freesurfer and FSL presented better relative overlay indexes than IBASPM. Freesurfer and IBASPM, compared with IBASPM, also had greater agreement with manual methods as measured by intraclass coreelations. The authors also mentioned that the errors of segmentation using IBASPM arose from inaccurate image registration and use of the MNI single-subject for the manually predefined region of interest of the hippocampus.

1.3 Problem Statement

Studies have shown that atlas-based volumetric analysis and visual rating methods can detect the neurodegenerative atrophy associated with AD and can distinguish different diagnostic groups. However, the success of the automated volumetric analysis relies on the accuracy of segmentation by the ROIs. Some studies have also shown there are errors in atlas-based segmentation. We believed the inaccuracy in IBASPM (SPM) based anatomical segmentation was caused by the following:

(1)The standard template used in SPM (or IBASPM), known as the MNI template, was created at McGill University (http://www.mni.mcgill.ca/). The MNI template was averaged from the T1-weighted images of 152 healthy subjects, of which 57% were male, 90% were right handed and with a mean age of 25 years. The default anatomical atlas of IBASPM is AAL which was manually segmented using images from a young normal brain. Although AAL is in the same MNI space as the MNI template, the regional anatomy is different. Even the deformation field was estimated accurately by applying image registration to the to-be-segmented image and the MNI template, warping the atlas to the to-be-segmented image would cause errors.

(2) Either the MNI template or AAL is from the images of 'normal' brains. However, the success of atlas based segmentation methods which rely heavily on heuristic rules and a priori shape information can be attributed to the accuracy and reliability of the atlas. Therefore, using a template and atlas which are morphologically variant from the investigated group would cause the inherent systematic bias (i.e. the patient images will tend to undergo more warping than the control images). In this case, it is preferable to generate a study-specific template and anatomical atlas used in the particular study.

VRS rating of the MB coronal slice has been shown to be valuable in the assessment of medial temporal lobe atrophy. To reduce inter-rater variability caused by different operators manually picking different slices to assess atrophy in a specific structure, an automatic method to mimic what is done in the VRS assessment of HPC is included in our study.

1.4 Thesis Contributions

The goal of this research is to build robust and automated measurement methods for assessing atrophy of large cohorts of MRI scans from aged subjects. All regional volumes of interest and regional area measures on a single coronal slice of subjects' MRIs were used for cross-sectional studies of cognitive impairment subjects. Furthermore, different atrophy measurements were compared regarding their addition to the clinical assessments and ability to distinguish diagnostic groups. The main contributions of this work are the following:

1. The introduction of a method of producing a new standardized stereotactic template to improve the accurate of atlas-based segmentation based on IBASPM (SPM5).

2. The introduction of a customized template set specifically for our study.

3. The introduction of methodology for automated regional area measures at MB coronal slice of MRI to assess the AD pathology atrophy.

4. Cross-sectional studies of cognitive impairment using the ROI volumetric and regional areas measures.

Chapter 2 Development of a New Coordinate Template

2.1 Image Registration

In atlas-based segmentation, image registration procedure is performance to estimate the spatial transformation parameter that maps corresponding points of the to-be-segmented image to the coordinate template which is standardized a stereotaxic space. Our development is conducted under the SPM environment.

The image registration procedure of SPM includes two steps. The first step is affine transform which is a linear approach for finding the best combination of global translation, rotation, and scaling factors to transform a brain into a standardized stereotaxic space. The second step is a higher-order nonlinear transform for fining the deformation field between the to-be-segmented image and the coordinate template that cannot be accounted by the affine transformation in regional level (Ashburner and Friston, 1999).

2.1.1 Affine Transform

An affine transformation preserves the straightness of lines and planarity of surfaces, as well as parallelism, but changes the angles between lines. The objective is to fit the object image ***f*** to a template image ***g***. An affine transformation from coordinates **x** in object image ***f*** to coordinates ***y*** in template image ***g*** is defined by

$$\begin{pmatrix} y_1 \\ y_2 \\ y_3 \\ 1 \end{pmatrix} = \begin{pmatrix} m_1 & m_4 & m_7 & m_{10} \\ m_2 & m_5 & m_8 & m_{11} \\ m_3 & m_6 & m_9 & m_{12} \\ 0 & 0 & 0 & 1 \end{pmatrix} \begin{pmatrix} x_1 \\ x_2 \\ x_3 \\ 1 \end{pmatrix} \tag{2.1}$$

This mapping is referred as **y**=**Mx**. **M** is the combination by multiplying the matrices of translation, rotation, zoom and shear:

$$\mathbf{M} = \mathbf{M}_{\text{translation}} \times \mathbf{M}_{\text{rotation}} \times \mathbf{M}_{\text{zoom}} \times \mathbf{M}_{\text{shear}}$$

Where,

$$\mathbf{M}_{\text{translation}} = \begin{pmatrix} 1 & 0 & 0 & q_1 \\ 0 & 1 & 0 & q_2 \\ 0 & 0 & 1 & q_3 \\ 0 & 0 & 0 & 1 \end{pmatrix}$$

$$\mathbf{M}_{\text{rotation}} = \begin{pmatrix} 1 & 0 & 0 & 0 \\ 0 & \cos\theta & \sin\theta & 0 \\ 0 & -\sin\theta & \cos\theta & 0 \\ 0 & 0 & 0 & 1 \end{pmatrix} \times \begin{pmatrix} \cos\phi & 0 & \sin\phi & 0 \\ 0 & 1 & 0 & 0 \\ -\sin\phi & 0 & \cos\phi & 0 \\ 0 & 0 & 0 & 1 \end{pmatrix} \times \begin{pmatrix} \cos\varphi & \sin\varphi & 0 & 0 \\ -\sin\varphi & \cos\varphi & 0 & 0 \\ 0 & 0 & 1 & 0 \\ 0 & 0 & 0 & 1 \end{pmatrix}$$

$$\mathbf{M}_{\text{zoom}} = \begin{pmatrix} q_4 & 0 & 0 & 0 \\ 0 & q_4 & 0 & 0 \\ 0 & 0 & q_5 & 0 \\ 0 & 0 & 0 & 1 \end{pmatrix}$$

$$\mathbf{M}_{\text{shear}} = \begin{pmatrix} 1 & q_6 & q_7 & 0 \\ 0 & 1 & q_8 & 0 \\ 0 & 0 & 1 & 0 \\ 0 & 0 & 0 & 1 \end{pmatrix}$$

Without zoom and shear, the affine transformation turns into rigid body transformation which is used to co-register images of the same subject together. The general affine transformation parameters m_i ($i = 1, \ldots, 12$) in Equation 2.1 is the function of parameters q_1 to q_8, θ, ϕ and φ (θ, ϕ and φ in radians). Usually, there are intensity difference between the object image ***f*** and the template image ***g***, so an additional intensity scaling parameter m_{13} is used to estimate the intensity difference.

In most cases, object image ***f*** and template image ***g*** have anisotropic voxels. And the dimensions of the voxels are also likely to differ. This problem can be solved by interpolation. However a simpler way is to affine transform the images to a Euclidian space, where measures of distances are expressed in millimeters and the origin is at the center of the image. For example, if object image ***f*** is of size 120×130×45, and has voxels that are 1.02mm×1.02mm×1.5mm, the affine transformation of image ***f*** into Euclidian space is defined by following matrix:

$$\mathbf{M_f} = \begin{pmatrix} 1.02 & 0 & 0 & -\dfrac{1.02\times 120}{2} \\ 0 & 1.02 & 0 & -\dfrac{1.02\times 130}{2} \\ 0 & 0 & 1.5 & -\dfrac{1.5\times 45}{2} \\ 0 & 0 & 0 & 1 \end{pmatrix} = \begin{pmatrix} 1.02 & 0 & 0 & -61.2 \\ 0 & 1.02 & 0 & -66.3 \\ 0 & 0 & 1.5 & -33.75 \\ 0 & 0 & 0 & 1 \end{pmatrix}$$

For template image ***g***, a similar 4×4 matrix $\mathbf{M_g}$ is defined for the affine transformation of image ***g*** into the Euclidian space. Therefore, affine transformation of object image ***f*** to template ***g*** is given by:

$$\mathbf{M_f}^{-1}\times\mathbf{M}_{\text{translation}}\times\mathbf{M}_{\text{rotation}}\times\mathbf{M}_{\text{zoom}}\times\mathbf{M}_{\text{shear}}\times\mathbf{M_g}$$

The transformation parameters (**M**) are optimized by minimizing the sum of squared differences (σ^2) between the object image and template images. σ is given as:

$$\sigma^2 = \sum_{i=1}^{I} e_i(\mathbf{M})^2 \quad i = 1, \ldots, I \tag{2.2}$$

Where e_i describes the difference between the object image ***f*** and the template image ***g*** at voxel i, and is given as below. I is the number of voxels.

$$e_i(\mathbf{M}) = f(\mathbf{Mx}_j) - m_{13}g(\mathbf{x}_i) \quad i = 1, \ldots, I$$

The algorithm for searching the affine transformation parameters **M** used by SPM is similar to Gauss-Newton optimization and is as follows for iteration n:

$$\mathbf{M}^n = \mathbf{M}^{n-1} - (\mathbf{A}^T\mathbf{A})^{-1}(\mathbf{A}^T\mathbf{b})$$

Where,

$$a_{ij} = \frac{\partial e_i(\mathbf{M})}{\partial m_j} = \frac{\partial f(\mathbf{M}\mathbf{x}_i)}{\partial m_j} \quad i = 1, \dots, I; \;\; j = 1, \dots, 12$$

$$a_{ij} = \frac{\partial e_i(\mathbf{M})}{\partial m_j} = \frac{\partial(-m_{13}g(\mathbf{x}_i))}{\partial m_j} = -g(\mathbf{x}_i) \quad i = 1, \dots, I; \quad j = 13$$

$$b_i = e_i(\mathbf{M}) \quad i = 1, \dots, I$$

The iteration converges when the decrease of σ^2 is negligible or the pre-determined number of iterations is reached

2.1.2 Non-linear Registration

A linear combination of three dimensional basis functions performed after the affine registration is used to estimating the nonlinear deformations. The transformation from coordinates **x** to coordinates **y** is given by:

$$\begin{pmatrix} y_1 \\ y_2 \\ y_3 \end{pmatrix} = \begin{pmatrix} a_{11} & a_{12} & \dots & a_{1N} \\ a_{21} & a_{22} & \dots & a_{2N} \\ a_{31} & a_{32} & \dots & a_{3N} \end{pmatrix} \begin{pmatrix} \theta_1(x_2, x_2, x_3) \\ \theta_2(x_2, x_2, x_3) \\ \vdots \\ \theta_N(x_2, x_2, x_3) \end{pmatrix} \tag{2.3}$$

Where θ_j is the orthogonal basis function, a_{ij} is the *j*th coefficient for *i*th dimension. Orthogonal basis functions are independent of each other and each of them contributes to the function definition in a certain unique way. Orthonormal basis functions can be viewed as unit orthogonal vectors in the function space and they satisfy:

$$\sum_{\mathbf{x}\in\Omega} \Psi_j(\mathbf{x})\Psi_k(\mathbf{x}) = \begin{cases} 0 & for \;\; j \neq k \\ 1 & for \;\; j = k \end{cases}$$

where Ω is the complete domain. A common choice is to represent the deformation field using a set of orthonormal basis functions such as Fourier basis functions. Here, discrete cosine transform basis functions are used to represent warps in each of the directions.

The basis function coefficient a is optimized by minimizing the sum of squared differences between the object image ***f*** and the template image ***g***. The parameters are optimized requiring the derivatives of the function of the sum of squared differences between the object image ***f*** and the template image ***g***. These can be obtained using the chain rule.

$$\frac{\partial f(\mathbf{y}_i)}{\partial a_{kj}} = \frac{\partial f(\mathbf{y}_i)}{\partial y_{ki}} \frac{\partial y_{ki}}{\partial a_{1j}} = \frac{\partial f(\mathbf{y}_i)}{\partial a_{1j}} \theta_j(\mathbf{x}_i)$$

Where k = 1, 2 or 3, stands for the three dimensions. The parameters optimization involves iteratively computing.

To avoid unnecessary deformations that only reduce the residual sum of squares by a tiny amount, regularization is introduced in the parameters optimization (Ashburner and Friston, 1999). Therefore the parameter estimation problem is re-defined as below:

$$\hat{\mathbf{p}} = \arg\max_{\mathbf{p}} (\Phi(f(\mathbf{p},\mathbf{x}), g(\mathbf{y})) + \boldsymbol{\beta}\Re(\mathbf{p})) \tag{2.4}$$

where, $\Phi(f(\mathbf{p},\mathbf{x}), g(\mathbf{y}))$ is a similarity measure, $f(\mathbf{p},\mathbf{x})$ is the nonlinear transformation of object image ***f*** to template image ***g***, $\mathbf{p}$ denotes all the transformation parameter, $\boldsymbol{\beta}$ is a regularization parameter and $\Re(\mathbf{p})$ is *a priori* information. And the parameter estimation problem can be solved by maximizing a similarity measure and a priori information in a maximum *a posteriori* estimator framework. The similarity measure is defined in Equation 2.2. For this definition, the lower σ^2, the higher Φ. There are some possible energy forms can be used for describing priors $\Re(\mathbf{p})$. Bending energy is used in the SPM package. The 3D bending energy is defined as following, and it is computed using finite sum at grid points (Rueckert et al., 1999).

$$
\begin{aligned}
\iiint & \left(\frac{\partial^2 \mathbf{u}_1(x_1,x_2,x_3)}{\partial {x_1}^2}\right)^2 + \left(\frac{\partial^2 \mathbf{u}_1(x_1,x_2,x_3)}{\partial {x_2}^2}\right)^2 + \left(\frac{\partial^2 \mathbf{u}_1(x_1,x_2,x_3)}{\partial {x_3}^2}\right)^2 \\
& + \left(\frac{\partial^2 \mathbf{u}_2(x_1,x_2,x_3)}{\partial {x_1}^2}\right)^2 + \left(\frac{\partial^2 \mathbf{u}_2(x_1,x_2,x_3)}{\partial {x_2}^2}\right)^2 + \left(\frac{\partial^2 \mathbf{u}_2(x_1,x_2,x_3)}{\partial {x_3}^2}\right)^2 \\
& + \left(\frac{\partial^2 \mathbf{u}_3(x_1,x_2,x_3)}{\partial {x_1}^2}\right)^2 + \left(\frac{\partial^2 \mathbf{u}_3(x_1,x_2,x_3)}{\partial {x_1}^2}\right)^2 + \left(\frac{\partial^2 \mathbf{u}_3(x_1,x_2,x_3)}{\partial {x_1}^2}\right)^2 \\
& + 2(\left(\frac{\partial^2 \mathbf{u}_1(x_1,x_2,x_3)}{\partial x_1 \partial x_2}\right)^2 + \left(\frac{\partial^2 \mathbf{u}_1(x_1,x_2,x_3)}{\partial x_2 \partial x_3}\right)^2 + \left(\frac{\partial^2 \mathbf{u}_1(x_1,x_2,x_3)}{\partial x_3 \partial x_1}\right)^2 \\
& + \left(\frac{\partial^2 \mathbf{u}_2(x_1,x_2,x_3)}{\partial x_1 \partial x_2}\right)^2 + \left(\frac{\partial^2 \mathbf{u}_2(x_1,x_2,x_3)}{\partial x_2 \partial x_3}\right)^2 + \left(\frac{\partial^2 \mathbf{u}_2(x_1,x_2,x_3)}{\partial x_3 \partial x_1}\right)^2 \\
& + \left(\frac{\partial^2 \mathbf{u}_3(x_1,x_2,x_3)}{\partial x_1 \partial x_2}\right)^2 + \left(\frac{\partial^2 \mathbf{u}_3(x_1,x_2,x_3)}{\partial x_2 \partial x_3}\right)^2 \\
& + \left(\frac{\partial^2 \mathbf{u}_3(x_1,x_2,x_3)}{\partial x_3 \partial x_1}\right)^2)dx_1x_2x_3
\end{aligned}
$$

Where,

$$\mathbf{u}_i = \sum_{j}^{N} a_{ij}\theta_j(\mathbf{x}_i) \quad i = 1,2,3$$

2.2 Image Segmentation of Different Tissue Classes

2.2.1 Distribution of Gray Matter, White Matter and Cerebrospinal Fluid Intensities in MRI

The three types of brain tissue, i.e., gray matter (GM), white matter (WM), and cerebrospinal fluid (CSF), can be classified from a T1 MRI scan. Figure 2.1 (A) – (D) show a slice of T1 MRI in coronal view and its GM, WM and CSF of the same slice, respectively. The algorithm used in the SPM for segmenting these three types of tissue is called Gaussian (or normal) mixture model-based clustering. The expectation-maximization (EM) approach, a well-established maximum likelihood algorithm, is employed for estimating the unknown cluster parameters (Ashburner and Friston, 1997).

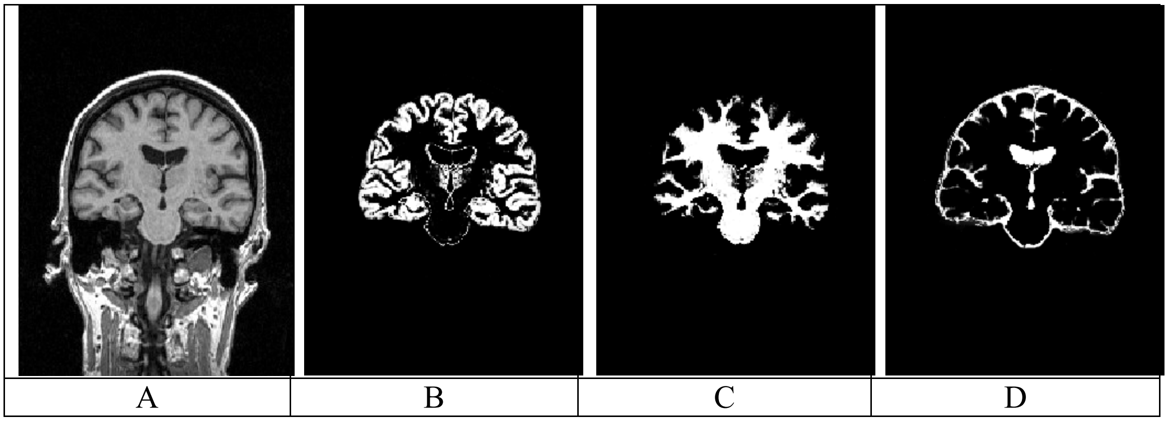

Figure 2.1 (A) One slice of a T1 weighted MRI in coronal view, and its gray matter (B), white matter (C) and cerebrospinal fluid (D) of the same slice in coronal view.

The voxel intensities belonging to GM, WM or CSF can be conformed to be a multivariate normal distribution (Ashburner and Friston, 1997). Figure 2.2 shows the intensity histograms of GM, WM and CSF of a T1 MRI. For each multivariate normal distribution, it can be described by a mean, a variance matrix and the number of voxels belonging to the distribution. So the entire data set (a to-be-segmented image) can be modeled by a mixture of these distributions.

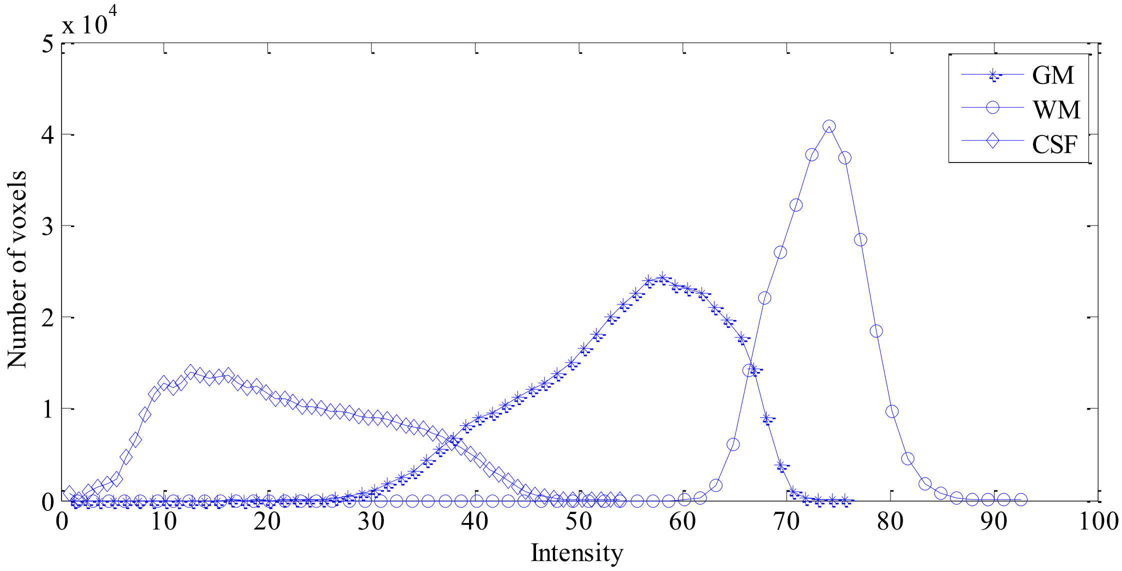

Figure 2.2 Intensity histograms for WM, GM and CSF of a randomly selected subject's T1 weighted MRI.

The EM algorithm performs an iterative computation of maximum likelihood estimation when the observed data are incomplete. Generally speaking, this approach is the iteration of "expectation" (the E step) and "maximization" (the M step). The E step is to evaluate the responsibilities using the current parameter values. The M step is to re-estimate the parameters using the responsibilities found in the E step.

2.2.2 Tissue Segmentation by EM for the Mixture of Gaussian

Some assumptions are made by the classification model. The to-be-segmented image is $f(\mathbf{x}_i)$, where $\mathbf{x}_i$ is the coordinate of image *f*, *i* denotes the index of voxels, from 1 to *I*. *K* is the known number of distinct tissue classes. Here *K* is three. To simply the algorithm, the distribution of the voxel intensities within each cluster is normal, and is described by the number of voxels within the cluster (h_k), the mean for that cluster (v_k), and the variance around that mean (c_k). The algorithm is described as follow.

1. Parameters initialization

   A belonging probability (p_{ik}) for each of the I voxels being drawn from each of the K clusters is initially assigned. To avoid leading the EM algorithm to converge to a "local" optimal point, the initialization of the mixture components is modified slightly by adding random noise.

2. Expectation step

   a. Compute the number of voxels belonging to each class (h_k) as

$$h_k = \sum_{i=1}^{I} p_{ik} \quad k = 1, \dots, K$$

   b. Calculate the mean voxel intensities for each class (v_k) as

$$v_k = \frac{\sum_{i=1}^{I} p_{ik} f(\mathbf{x}_i)}{h_k} \quad k = 1, \dots, K$$

   c. The variance of each class (c_k) is then computed as

$$c_k = \frac{\sum_{i=1}^{I} p_{ik} (f(\mathbf{x}_i) - v_k)^2}{h_k} \quad k = 1, \dots, K$$

3. Maximization step

   a. Compute the probability density functions for the classes at each voxel:

$$r_{ik} = \frac{1}{(2\pi c_k)^{0.5}} \exp\left(\frac{-(f(\mathbf{x}_i) - v_k)^2}{2c_k}\right) \quad i = 1, \dots, I; \quad k = 1, \dots, K$$

   b. The probabilities of cluster k for the voxel i is as:

$$s_{ik} = r_{ik} h_k \qquad i = 1, \dots, I; \;\; k = 1, \dots, K \tag{2.5}$$

c. The probabilities is normalized so that they integrate to 1 at each

$$p_{ik} = \frac{s_{ik}}{\sum_{l=1}^{K} s_{il}} \quad i = 1, \dots, I; \quad k = 1, \dots, K$$

4. Repeat

Re-evaluate the log-likelihood as below and check its change.

$$\sum_{i=1}^{I} \log(\sum_{k=1}^{K} s_{ik})$$

The algorithm converges when the change of the log-likelihood is less than a given threshold or the pre-determined number of iterations is reached.

Normal Mixture Models with high likelihood can be successfully used to create soft clustering boundaries around data. The component distributions tend to have the high “peaks”. However, image segmentation using this clustering algorithm, based on MRI intensities only, is very much challenged. Examining Figure 2.2, which shows the intensity histograms of GM, WM and CSF, there are apparent overlaps between the class distributions (e.g., CSF and GM, GM and WM). Adding additional information, such as the global position within the brain, can help to disambiguate the classification of different tissue. The use of spatial distributions of the different tissue can be facilitated by the construction of the probability images in the standard space. Here, b_k ($k = 1, \ldots, K$) denotes the *a priori* image of class (tissue) k in the below functions. Figure 2.3 shows coronal views of the *a priori* images of GM (A), WM (B) and CSF (C). These *a priori* images, provided by the Montreal Neurological Institute, are derived from scans of more than one hundred young healthy subjects (Ashburner and Friston, 1997).

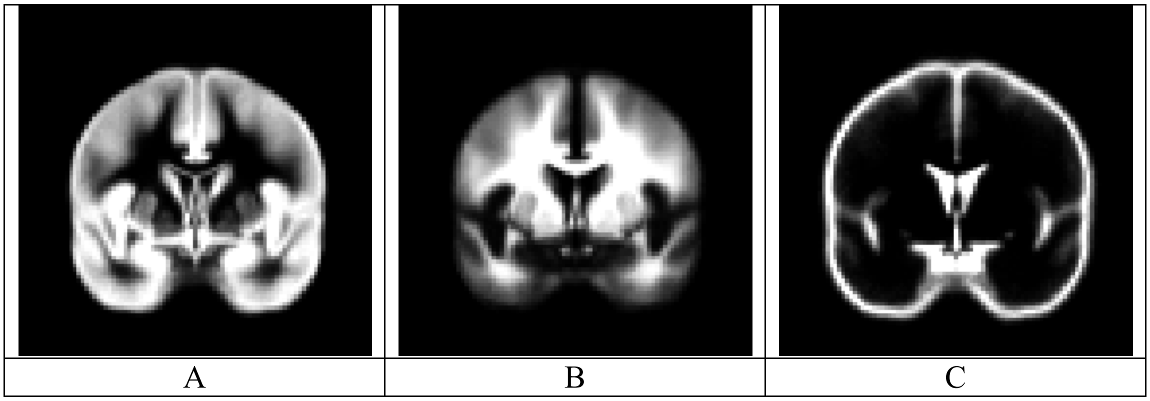

A B C

Figure 2.3 Coronal views of the *a priori* images of GM (A), WM (B) and CSF (C). These *a priori* images provided by the Montreal Neurological Institute are derived from scans of 152 young healthy subjects.

To utilize the *a priori* information, Equation 2.5 is replaced by:

$$s_{ik} = r_{ik} h_k \frac{b_k(\mathbf{M}^{-1}\mathbf{x}_i)}{\sum_{l=1}^{I} b_k(\mathbf{M}^{-1}\mathbf{x}_l)} \quad i = 1, \ldots, I; \quad k = 1, \ldots, K$$

Where, **M** is the spatial affine transformation parameter matrix which has been derived in the image registration step. Based on the information from the *a priori* probability images (see Figure 2.3), $\frac{b_k(\mathbf{M}^{-1}\mathbf{x}_i)}{\sum_{l=1}^{I} b_k(\mathbf{M}^{-1}\mathbf{x}_l)}$ effectively produces a weighted mean (h_k) of the image voxels. . This weight can be regarded as the probability density function of a voxel from cluster *k* being found at location *i*, irrespective of how many voxels of type *k* there are in the brain (Ashburner and Friston, 1997). This tissue segmentation algorithm can be more robust and accurate by including the tissue spatial *a priori* information for estimating the cluster parameters.

2.3 New Coordinate Template Design

2.3.1 Motivation

As mentioned in section 1.3, the most widely used standard MNI template (available in the templates directory of SPM99 and later versions) is the average of 152 normal MRI scans, each of which has been matched to the MNI305 space. The “averaging” process increases the signal to noise ratio, reduces the anatomic difference from subject to subject and maintains common spatial variability. This process is equivalent to a “low pass filter”, which enhances the “low frequency” component and decreases the “high frequency” component of the template in frequency domain. Since it only carries the common spatial variability, this template is widely used as a coordinate system for mapping individual object images to the same stereotaxic space. The image registration of the object image to the stereotaxic space in SPM5 is not the voxel-to-voxel mapping. It estimates less 1000 parameters. Using a high resolution image as coordinate template, the image registration process is unable to converge into a limited number of local minima. Sophisticated algorithms might have the capability, however, with time-consuming computation as trade-off. After the atlas-based segmentation method appears, MNI template also has been employed as coordinate template in the atlas-based segmentation procedures (Alemán-Gómez *et al.*, 2006; Hayashi *et al.,* 2009; Tae *et al.,* 2008; Seixas F.Z., 2010). However, the MNI template is an average brain. Without the detailed anatomical information, no atlas can be defined from it directly. Generally, the atlas used is defined from a high resolution image which has been aligned to the MNI template, such as AAL (Tzourio-Mazoyer *et al.* 2002). If the atlas is not “originated” from the same “source” of coordinate template used in atlas-based segmentation procedures, even the image registration (from the individual object MRI image to the coordinate template) parameters is estimated accurately, it will inevitably induce segmentation errors to deform the atlas to the individual object image using those image registration parameters.

AAL atlas (Tzourio-Mazoyer *et al.*, 2002) is a widely used atlas definition in the automatic atlas-based segmentation procedure. This atlas was manually delineated on a high resolution MNI (Montreal Neurological Institute) single subject MRI image, which was obtained from the MRI acquisition of a young man whose brain was scanned 27 times using a T1-weighted gradient echo sequence (TR/TE/FA = 18 ms/10 ms/30°). Each acquired image was spatially normalized by using a nine-parameter linear transformation to the MNI305 space (the first standard stereotactic template created by MNI). To facilitate the following discussion, the phrase “single-subject image” will specifically describe this image used for AAL definition. If this single-subject image could have the MNI template’s frequency information, the “origination” problem would have been solved. Based on this concept, following processing steps were designed.

2.3.2 Methods

Figures 2.4 and 2.5 show the intensity images (top rows) and frequency spectra (bottom rows) of the single-subject and the MNI template in spatial domain and frequency domain respectively. The following processing steps were designed to make single-subject image have the similar frequency spectrum to the MNI template’s.

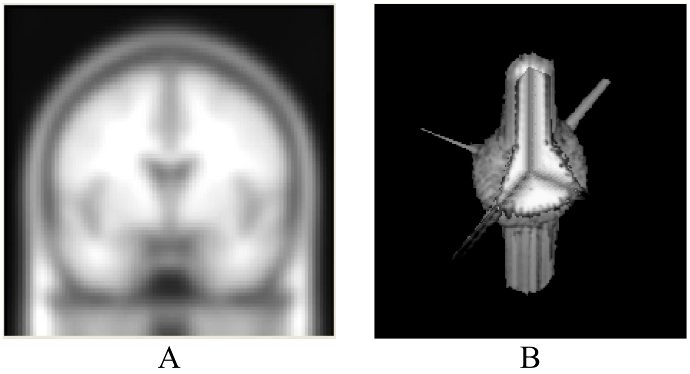

Figure 2.4 (A) The MNI template in spatial domain shows "blurring" of the image. (B) The 3D amplitude spectrum of the MNI template after Fourier transform shows the low frequency component dominates the spectrum. The most of the "high frequency" information has been filtered out by the "averaging-smoothing" process.

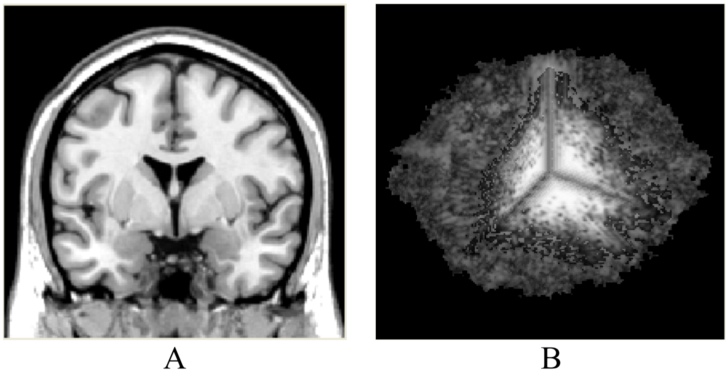

Figure 2.5 (A) The high resolution single-subject image shows anatomical structures clearly. (B) The 3D amplitude spectrum of the single-subject image after Fourier transform shows that both low frequency and high frequency components occupy the frequency domain.

<u>1) Gaussian Filter</u>

$$G(x_1) = \frac{1}{\sqrt{2\pi}\sigma} e^{-\frac{{x_x}^2}{2\sigma^2}} \tag{2.6}$$

where $G(x_1)$ is a normalized 1D Gaussian kernel, and σ is the standard deviation of the distribution (the size of σ is inversely related to the cut-off frequency). 3D Gaussian filter is a digital version of the product of three 1D Gaussian:

$$G(x_1, x_2, x_3) = G(x_1)G(x_2)G(x_3) = \frac{1}{\sqrt{2\pi}\sigma} e^{-\frac{x_1^2 + x_2^2 + x_3^2}{2\sigma^2}} \tag{2.7}$$

A convolution was performed three dimensionally between the Gaussian kernel and the single-subject image $I(x_1, x_2, x_3)$. This procedure is given by:

$$J(x_1, x_2, x_3) = G(x_1, x_2, x_3) \otimes I(x_1, x_2, x_3) \tag{2.8}$$

Where $\otimes$ denotes convolution, and $J(x_1, x_2, x_3)$ is the smoothed version of single-subject image $I(x_1, x_2, x_3)$. Through this convolution process, the low frequency component can be increased and the high frequency component is removed from the single-subject image.

2) Fourier Transformation

Fourier transform was three-dimensionally performed on the smoothed single-subject image I and MNI template image P.

$$J_F = \left|\mathrm{FT}(J(x_1, x_2, x_3))\right| \quad P_F = \left|\mathrm{FT}(P(x_1, x_2, x_3))\right| \tag{2.9}$$

Where FT denotes Fourier transform. J_F is the 3D amplitude spectrum of J in frequency domain, and P_F is the 3D amplitude spectrum of P in frequency domain.

3) Similarity Metrics

In this step, the similarity between the 3D amplitude spectrum J_F of the smoothed single-subject image and the 3D amplitude spectrum P_F of the MNI template image was measured. For a qualitative examination of the similarity, the metrics can either be a calculation over the whole images, or an estimation of specifically determined structures in these two 3D amplitude spectrum images. Normalized cross-correlation and cut-off frequency as two similarity measurements are here.

The cross-correlation measures the intensity difference between the images and sums the product, estimating the similarity of the images from this value. The normalized cross-correlation is calculated using the following equation:

$$NCC(P_F, J_F(\sigma)) = \frac{\sum (P_F - \bar{P}_F)(J_F(\sigma) - \bar{J}_F(\sigma))}{\sqrt{\sum (P_F - \bar{P}_F)^2 \sum (J_F(\sigma) - \bar{J}_F(\sigma))^2}} \tag{2.10}$$

where $\bar{P}_F$ and $\bar{J}_F$ are the mean magnitude values of 3D amplitude spectrum J_F and P_F respectively. The maximum normalized correlation coefficient between J_F and P_F is defined as the optimal matching criterion.

The cut-off frequency of 3D amplitude spectrum is defined as the radius of a sphere centered in the frequency domain (see Figure 2.6). The radius is chosen by specifying $\frac{1}{\sqrt{2}}$ of the total power enclosed by the sphere. The total power TP_F of 3D amplitude spectrum P_F is given by:

$$TP_F = \sum_{x_1} \sum_{x_2} \sum_{x_3} (P_F(x_1, x_2, x_3))^2 \tag{2.11}$$

Where r_P denotes the cut-off frequency of 3D amplitude spectrum P_F. r_J denotes the cut-off frequency of 3D amplitude spectrum J_F. The optimal matching criterion using cut-off frequency similarity is given by:

$$(\hat{\sigma}) = \arg\min_{\sigma} \, (r_P - r_J(\sigma))^2 \tag{2.12}$$

4) Optimization Process

The process for searching $\hat{\sigma}$ which is used to smooth the single-subject image is automated by varying σ as it matches the optimal criterion. σ starts from 1, with increments of 0.1, until the amplitude spectrum J_F of the smoothed single-subject image is most “similar” to the amplitude spectrum P_F of MNI template image.

Figure 2.7 shows the new coordinate template intensity images (left) and amplitude spectrum (right). Figure 2.8 shows the flowchart of the described procedure. In Figure 2.8, the normalized cross-correlation is employed for examination the similarity between the smoothed single-subject spectra and MNI template spectra in frequency domain. This similarity metrics can be replaced with cut-off frequency and the optimal matching criterion is given by Equation 2.10. Figure 2.9 shows that the normalized correlation coefficient between the spectra of the smoothed single-subject and MNI template reaches maximum when Sigma (σ) equals 1.9. Without smoothing (Sigma equals 0), the normalized correlation coefficient is as low as 0.52. Figure 2.10 shows that the smoothed single-subject image has the most similar cut-off frequency to the MNI template when Sigma (σ) equals 2.0.

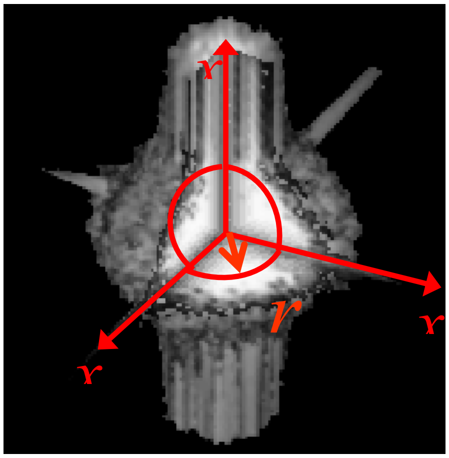

Figure 2.6 Cut-off frequency *r* of 3D amplitude spectrum is defined as the radius of a sphere centered in the frequency domain. The radius is chosen by specifying $1/\sqrt{2}$ of the total power enclosed by the sphere.

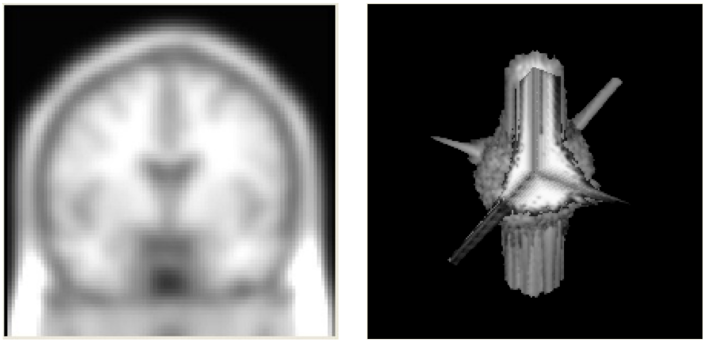

A B

Figure 2.7 (A) The single-subject image appears blurring after convolution with a Gaussian kernel. (B) The spectra of the smoothed single-subject with $\sigma=1.9$ are similar to the spectra of the MNI template in frequency domain.

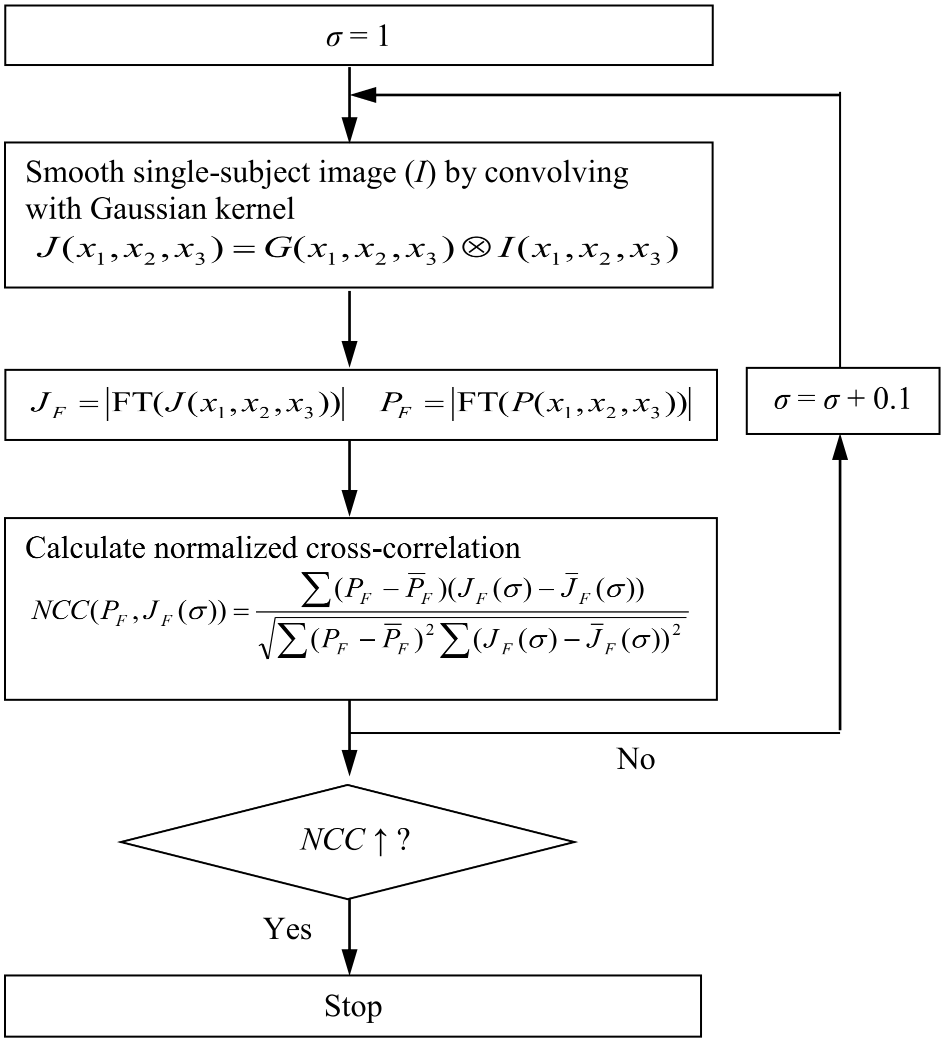

Figure 2.8 A schematic flow diagram for creation the new coordinate template. The single-subject image is smoothed by convolving the Gaussian kernel with σ=1. Similarity of the spectra of the smoothed single-subject and the MNI template is measured by calculating the normalized cross-correlation. The procedure stops when NCC yields the maximum.

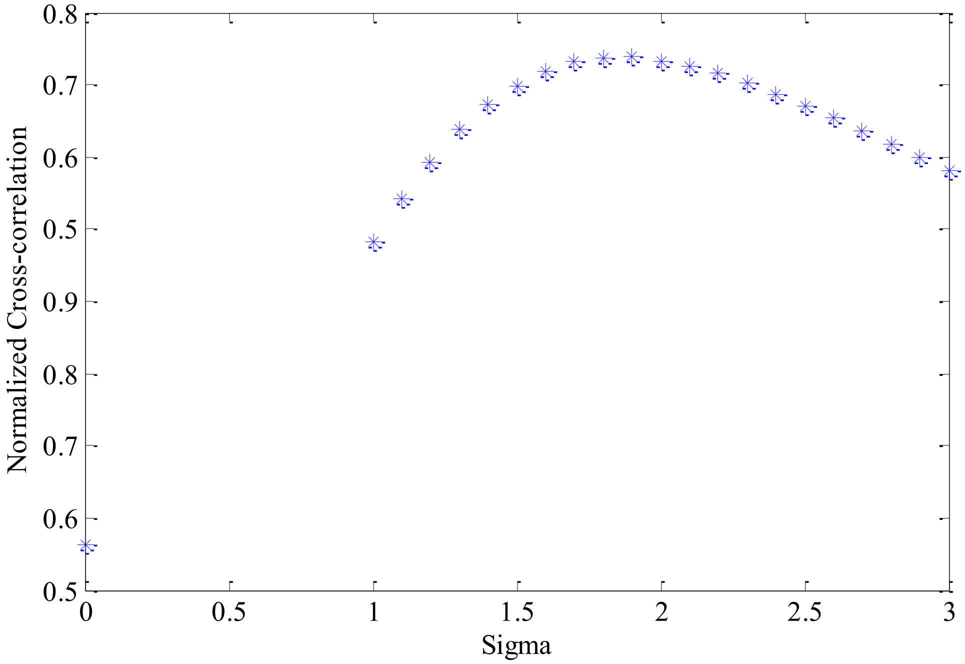

Figure 2.9 Normalized cross-correlation coefficient between the spectra of the smoothed single-subject and MNI template reaches maximum (0.869) when Sigma (σ) equals 1.9. Without smoothing (Sigma equals 0), the normalized correlation coefficient is low as 0.52.

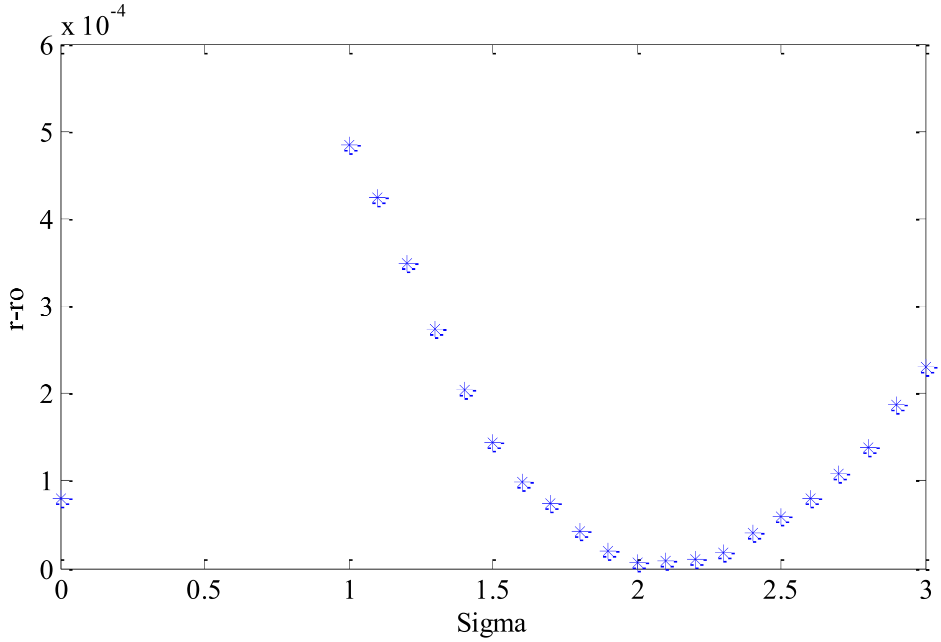

Figure 2.10 Plot for the difference of the cut-off frequency between the smoothed single-subject image and MNI template. Smoothed single-subject image has the most similar cut-off frequency with MNI template when Sigma (σ) equals 2.0.

2.4 ROI Segment Procedure

2.4.1 Manual Tracing

Manual segmentation by human expert is still regarded as the “gold standard”. The boundary definition of the ROIs followed the published protocol described by Tzourio-Mazoyer *et al.* (2002) which was applied on AAL. Manual tracing of a ROI on a T1-weighted MRI image was performed on each slice of coronal plane from anterior-to-posterior and corrected in the sagittal plane. The performance was done by using publicly available software MRIcroN (http://www.cabiatl.com/mricro/mricron/).

2.4.2 Automated Atlas-based Segment Procedure

Volumetric automatic segmentation of a to-be-segmented T1-weighted MRI scan includes following steps. 1) MRIs were segmented into gray matter, white matter and cerebral spinal fluid (see Figure 2.11); 2) MRI scans were spatially registered to coordinate templates using affine transformations for approximate registration, and nonlinear transformation for fine registration to obtain the deformation field (see Figure 2.12); 3) An automatic atlas was deformed to the to-be-segmented T1-weighted MRI and each structure encoded with an unique intensity value (see Figure 2.13); 4) Volume information for each structure was derived by summing the number of voxels assigned the same coding intensity value and then multiplying by the voxel size (see Figure 2.13); 5) Total intracranial volume (TIV) was calculated as the summation of gray matter, white matter, and cerebrospinal fluid volumes, and TIV was used to normalize each brain structure’s volume. The above procedures utilized the modified functions in SPM5 and IBASPM (Alemán-Gómez *et al.*, 2006)

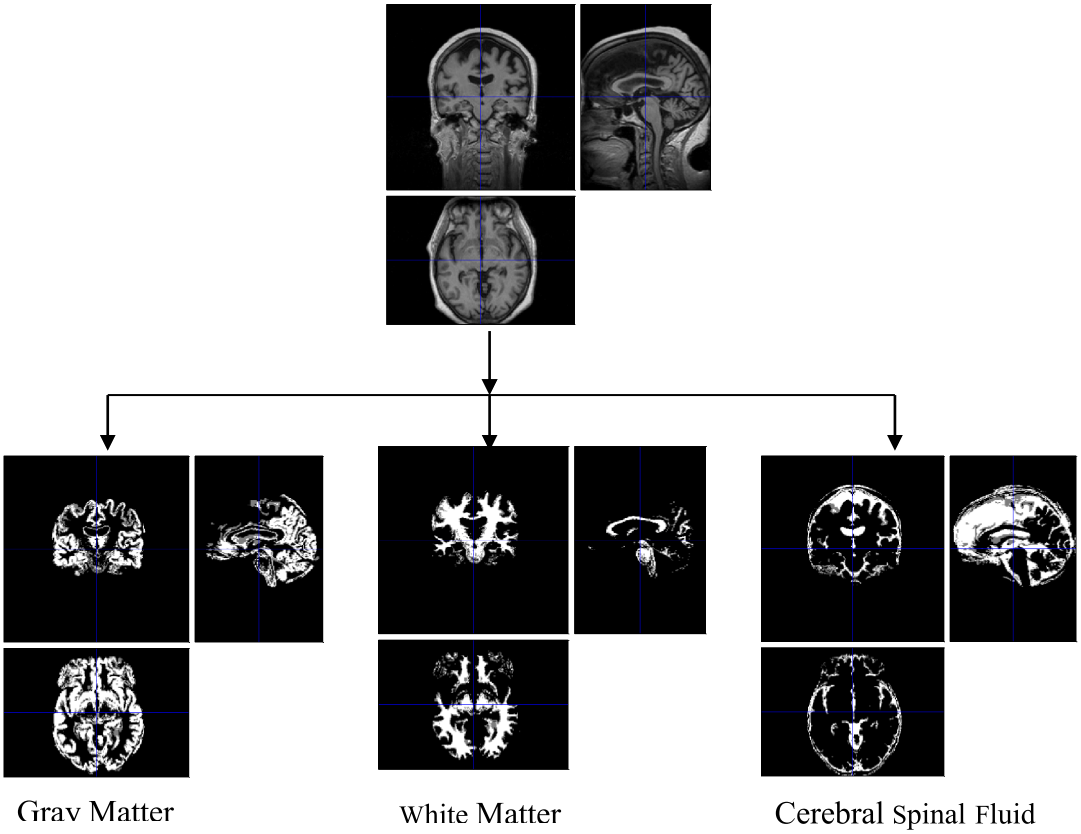

Figure 2.11 T1 weighted MRI segmentation of three tissues: gray matter, white matter and cerebral spinal fluid

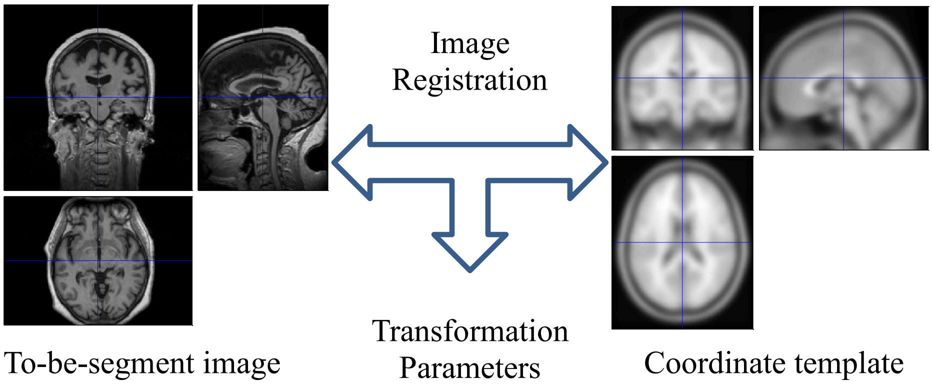

Figure 2.12 To-be-segmented T1 weighted MIR registration to the coordinate template.

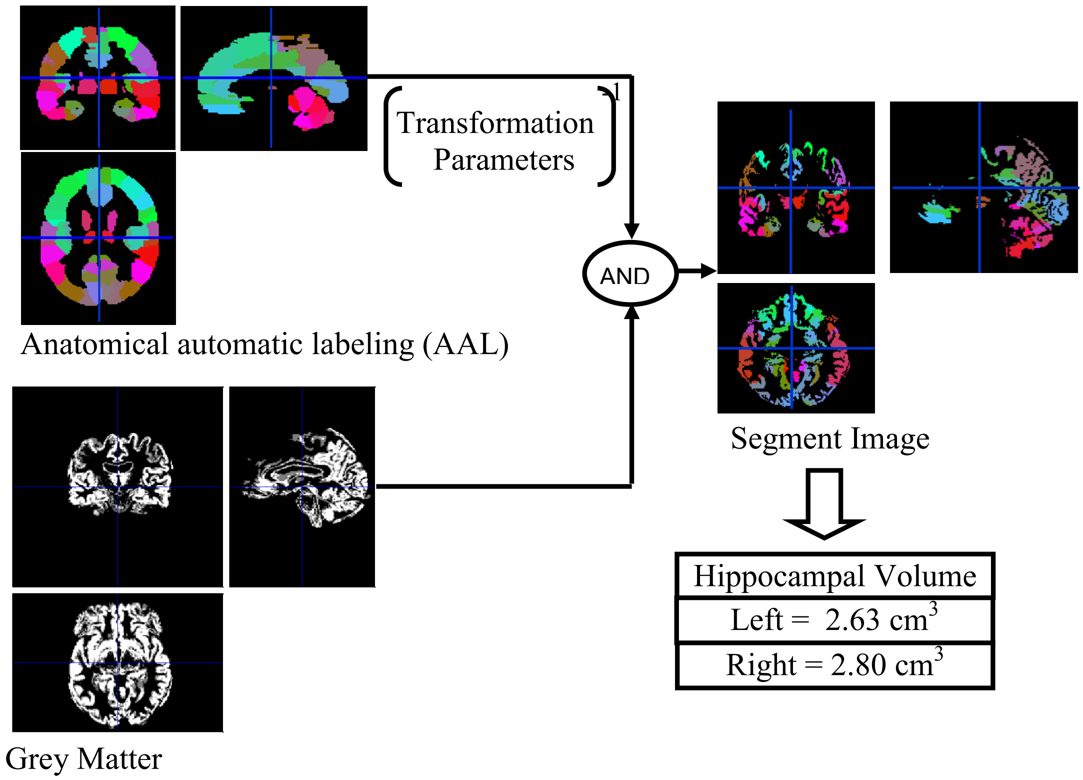

Figure 2.13 Anatomic atlas is warped to the to-be-segmented image and generates the automated regional segmented image for calculating the volume of the ROIs.

2.5 Validation

Since the single-subject image is the data source where AAL comes from, the new coordinate template has been validated on the single-subject image itself first.

2.5.1 Correspondence of HPC and AMG Volumes Using Manual and Automated Segmentation

Though AAL includes 116 regions, here we focus the validations on hippocampus and amygdale, since these two MTL substructures have been reported to be strongly correlated to the severity of AD pathology. In this validations the high resolution single-subject image was used as the “to-be-segmented image”. Volumetric segmentation by using the MNI template or the new coordinate template of the hippocampus (HPC) and amygdale (AMG) were performed. The automated atlas-based segment procedures were described in section 2.4.2. Segment volumes of HPC and AMG were superimposed to the high resolution single-subject image. One coronal slice was shown in Figure 2.14. The segment volumes of HPC and AMG were in red. HPCs were shown in the left column, whereas AMGs were shown in the right column. Atlas-based automated segments using new coordinate template were shown in the top row. Segments using MNI template were shown in the bottom row.

As is evident (visually checking slice by slice), the automated delineation of the hippocampus and amygdala on serial coronal slices was better matched the original image by using the new coordinate template than the MNI template.

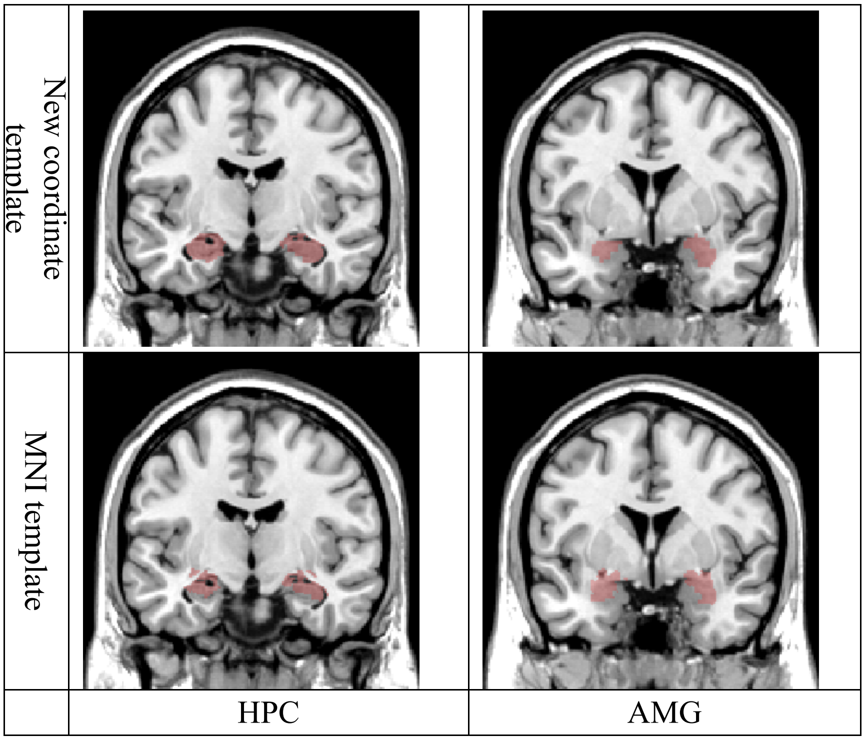

Figure 2.14 Comparison automated segments of hippocampus (HPC) and amygdale (AMG) using new coordinate template and MNI template. Automated segments (in red) are superimposed on the subject's MRI. HPCs are shown in left column, whereas AMGs are shown in right column. Atlas-based automated segments using new coordinate template are shown top row. Segments using MNI template are shown bottom row.

To further validate the new coordinate template, several quantitative measures were used. In the formulae presented below, the segmentation result is denoted as A and the gold standard is denoted as G (see Figure 2.15(A)). The gold standards are the manual segmentations of hippocampus and amygdala from the high resolution single-subject MR image. The manual segmentation procedures have been described in section 2.4.1.

<u>Volume Overlap</u>

Similarity indices (D) (Dice, 1945) and overlap ratios (J) (Jaccard, 1907) are two widely used spatial overlap agreement measures. Similarity index is defined as the intersection divided by the mean volume of the two volumes,

$$D = \sum \frac{2|A_i \cap G_i|}{|A_i| + |G_i|}, \qquad 2.10$$

where A_i and G_i are binary values for each voxel, i.e., 1 if the voxel is within the volume of interest, 0 if the voxel is outside the volume of interest, $\cap$ stands for logic "AND" operation. Similarity indices range between 0 (no overlap) and 1 (perfect agreement). Overlap ratio is the intersection over the union:

$$J = \sum \frac{|A_i \cap G_i|}{|A_i \cup G_i|} = \frac{D}{2-D} \qquad 2.11$$

where $\cup$ stands for logic "OR" operation. Overlap ratio can be derived from similarity indices.

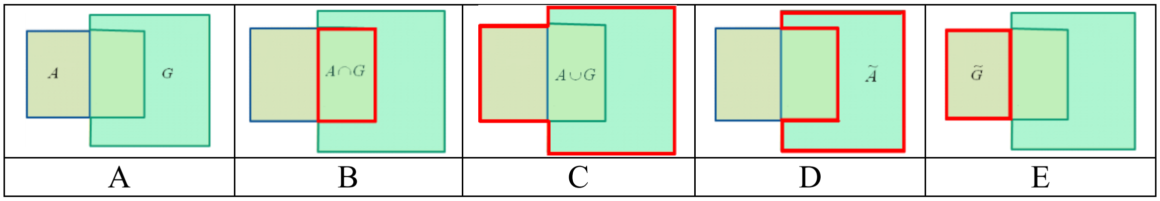

A B C D E

Figure 2.15 (A) A is for the automatic segment and B is for the gold standard. (B) $A \cap G$. (C). $A \cup G$. (D) $\tilde{A}$ (E) $\tilde{G}$.

False positive (FP) and false negative (FN) errors, which are two widely used spatial overlap disagreement measures, are used for evaluating how much over-segmentation or under-segmentation. False positive (FP) error for a given volume is the measure of how much of the volume outside volume of interest is incorrectly assigned to the volume's label. It is computed as the volume of a source region outside the corresponding target region divided by the volume of the source region (Klein *et al.*, 2009):

$$FP = \sum \frac{2\,|A_i \cap \tilde{G}_i|}{|A_i| + |G_i|} \qquad 2.12$$

where $\tilde{G}_i$ is logic "NOT" operation on G_i, i.e., 0 if G_i is 1 and 1 if G_i is 0. FP ranges from 0 (perfect overlap) to 1 (no overlap). A false negative error for a given region is the measure of how much of that region is incorrectly labeled. It is computed as the volume of a target region outside the corresponding source region divided by the volume of the target region (Klein *et al.*, 2009):

$$FN = \sum \frac{2\,|\bar{A} \cap G_i|}{|A| + |G_i|} \qquad 2.13$$

where $\tilde{A}_i$ is logic "NOT" operation on A_i, i.e., 0 if A_i is 1 and 1 if A_i is 0. FN ranges from 0 (perfect overlap) to 1 (no overlap).

Volume Similarity

Volume similarity coefficient, VS, is defined as the ratio of the absolute difference between the segmented volume V_a, obtained through the MNI template and the new single subject template, and the manual segmented volume V_g (gold standard) to the gold standard volume V_g. Although this measure does not reflect registration accuracy, it is a conventional measure included for retrospective evaluation of prior studies. VS is equal to 0, if no difference between V_a and V_g (perfect overlap).

$$VS = \frac{|V_a - V_g|}{V_g} \tag{2.14}$$

All quality measures are listed in Table 2.1. Segmentation of hippocampus and amygdala on the single-subject image, using the new coordinate template yielded better results than the MNI template in all quantitative volumetric measures. This validation indicates that even the single-subject image from which the AAL atlas was defined cannot be perfectly segmented by the same AAL atlas.

Table 2.1 Segmentation quality indices for the new coordinate template and MNI template

	ROI	D	J	FP	FN	VS
New coordinate template	Left HPC	0.969	0.973	0.048	0.015	0.033
	Right HPC	0.974	0.972	0.037	0.015	0.022
	Left AMG	0.986	0.939	0.026	0.001	0.025
	Right AMG	0.986	0.949	0.027	0.001	0.027
MNI template	Left HPC	0.617	0.446	0.344	0.421	0.074
	Right HPC	0.728	0.572	0.246	0.298	0.050
	Left AMG	0.601	0.429	0.393	0.406	0.013
	Right AMG	0.635	0.466	0.381	0.348	0.033

Regional segmentation of hippocampus and amygdala on single-subject image using the new coordinate template yielded better results than the MNI template in all quantitative volumetric measures, overlap ratio (D), similarity indices (J) false positive (FP), false negative (FN) and volume similarity coefficient (VS). HPC = hippocampus; AMG = amygdale.

2.5.2 Similarity Comparison using MNI Template and New Coordinate Template

Our hypothesis was that increased accuracy in deforming the high resolution single-subject image from which the AAL was derived to the to-be-segmented image, would lead to increased accuracy in warping the anatomic atlas labels (AAL) to the appropriate anatomic locations of the to-be-segmented image.

The deformed high resolution single-subject image was obtained by an inverse transformation to the to-be-segmented image space using the image registration parameters estimated in the spatial transformation step. The accuracy by using the deformed high resolution single-subject image was evaluated by the similarity between this deformed single-subject image and the to-be-segmented image. Normalized cross-correlation and sum of squared difference were employed to assess the image similarity. The cross-correlation is given by:

$$NCC(S,S_I)=\frac{\sum_{\mathbf{x}\in\Omega}(S-\bar{S})(S_I(T(\mathbf{x}))-\bar{S}_I)}{\sqrt{\sum_{\mathbf{x}\in\Omega}(S-\bar{S})^2\sum_{\mathbf{x}\in\Omega}(S_I(T(\mathbf{x}))-\bar{S}_I)^2}} \qquad 2.15$$

Where **x** is the coordinates of the single-subject image. $\bar{S}$ is the mean intensity of the to-be-segmented image. $\bar{S}_I$ is the mean intensity of the inversely transformed single-subject image in to-be-segmented image space.

The sum of squared difference is given by:

$$SSD(S,S_I)=\sum_{\mathbf{x}_i\in\Omega}(S-S_I(T(\mathbf{x}))^2 \qquad 2.16$$

In Equation 2.15 and Equation 2.16, Ω (see Figure 2.16) is a mask for defining the similarity measure region only inside of the skull, so as to avoid mis-evaluating outside of skull. T is the image registration matrix estimated from the spatial transformation step. The matrix T using the new coordinate template and the matrix T using MNI template were applied in Equation 2.15 and Equation 2.16. Both similarity comparisons were performed on 241 MR images which were chosen by convenience from the Wien Center for Alzheimer's Diseases and Memory Disorders at Mount Sinai Medical Center (Miami Beach, Florida) (see section 5.2). Results plotted in Figures 2.17 and Figure 2.18 show that the inversely transformed single-subject image was more correlated to the to-be-segmented image (see Figure 2.17) and had a lower sum of squared difference with to the to-be-segmented image (see Figure 2.17). Therefore, this image matched the to-be-segmented image better by using the new coordinate template than the MNI template, with the exception of two subjects.

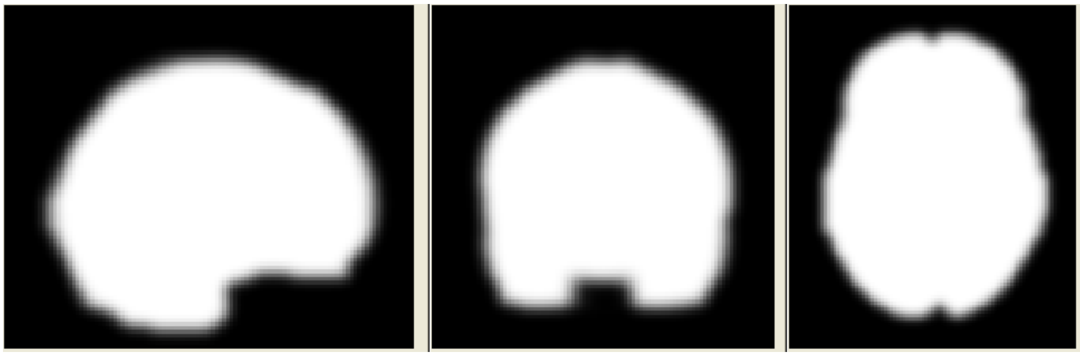

Figure 2.16 Mask Ω which only includes the part inside of skull is used to define the similarity measure region.

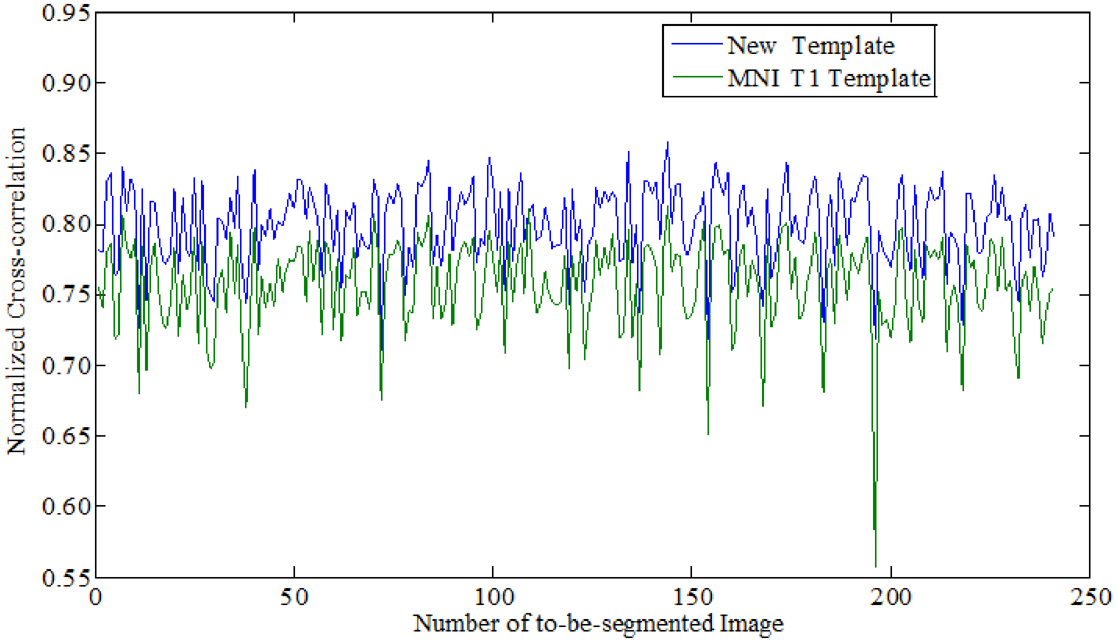

Figure 2.17 Similarity comparisons on 241 MR images using normalized cross-correlation.

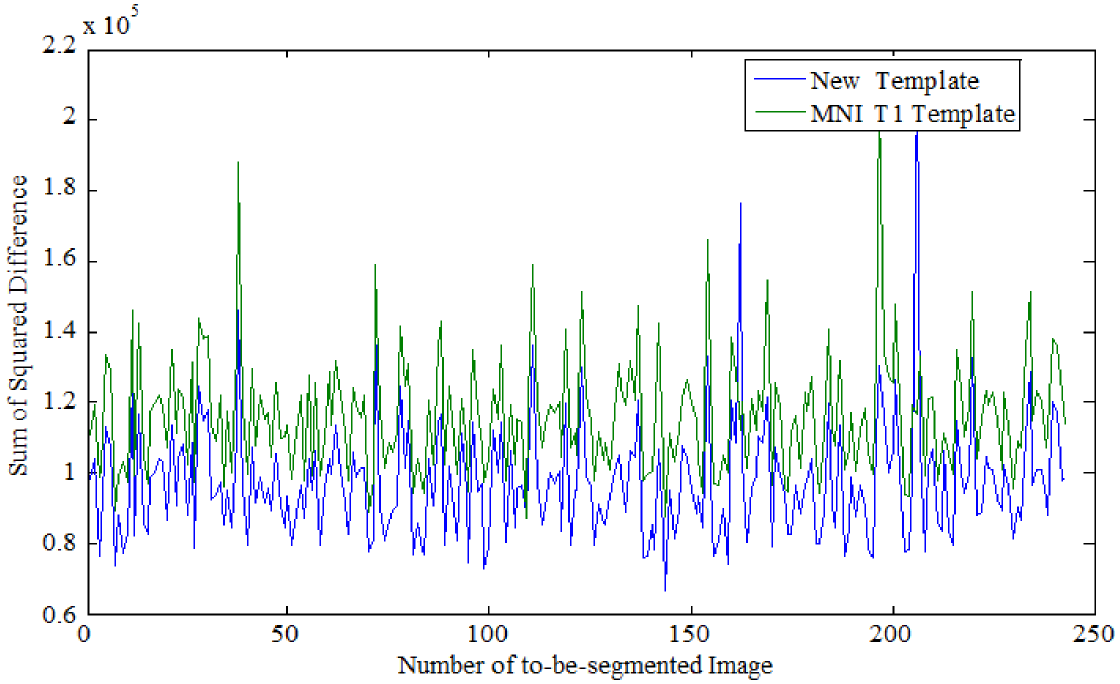

Figure 2.18 Similarity comparisons on 241 MR images using sum of squared difference.

Chapter 3 Development of a Custom Elderly Template Set – Template E Set

3.1 Motivation

Various studies show that as adults get older, their brains become smaller and the sulci visibly increase in size and depth. Autopsy studies confirm that brain weight in both men and women declines by at least 10% between the ages of 25 and 75+ years. In a postmortem study, Miller et al. (1980) found that brain volume decreases at the rate of about 2% per decade following the age of 50. MRI based studies also show that the rate of brain atrophy accelerates in older age groups, but there appears to be no sex differences in brain aging patterns (Allen *et. al*., 2005).

It has been confirmed by previous studies (Miller *et al*., 1980; Allen *et. al*., 2005), that there exist significant anatomic differences between young adult brains and aged adult brain If the anatomic labeling used in the atlas-based segmentation is defined on a young adult brain, the anatomic differences will induce measurement errors in the aged brains. For the volumetric studies on older subjects, it is important to establish an anatomic template specifically suited for the elderly who are being studied.

Many studies have confirmed that the severity of atrophy medial temporal lobe structures, such as hippocampus and amygdale, strongly correlate to the severity of AD pathology and to the severity of cognitive and functional impairment as well as to the subsequent rate of progression (de Jong *et al.*, 2008; Firbank *et al.*, 2008; Colliot, *et al.*, 2008; Mori *et al.*, 1997; Ishii *et al.*, 2006; Devanand *et al.*, 2008; Teipel *et al.*, 2006; Müller *et al.*, 2005 Babiloni *et al.*, 2009 Chao *et al.*, 2010 Leung *et al.*, 2010). In addition to confirming the well known presence of decreased grey matter in the MTL regions, this study will investigate the phenomenon in the other areas, such as deep brain structure putamen and thalamus. Questions are whether these regions suffer degeneration in Alzheimer's disease, and whether such degeneration is associated with cognitive deterioration. This study will also examine the ventricles to confirm that dilatation of ventricle is a feature of patients with AD or MCI (Jack *et al.*, 2004; Brewer *et al.*, 2009). Altogether, we will create an atlas of 26 regions, including the insula, hippocampus parahippocampal, amygdale, fusiform, precuneus, putamen, thalamus, superior temporal (temporal_Sup), superior temporal pole (temporal_Pole_Sup), middle temporal (temporal_Mid), inferior temporal (temporal_Inf) and ventricle on both hemispheres. Some of the regions are shown in Figure 3.1.

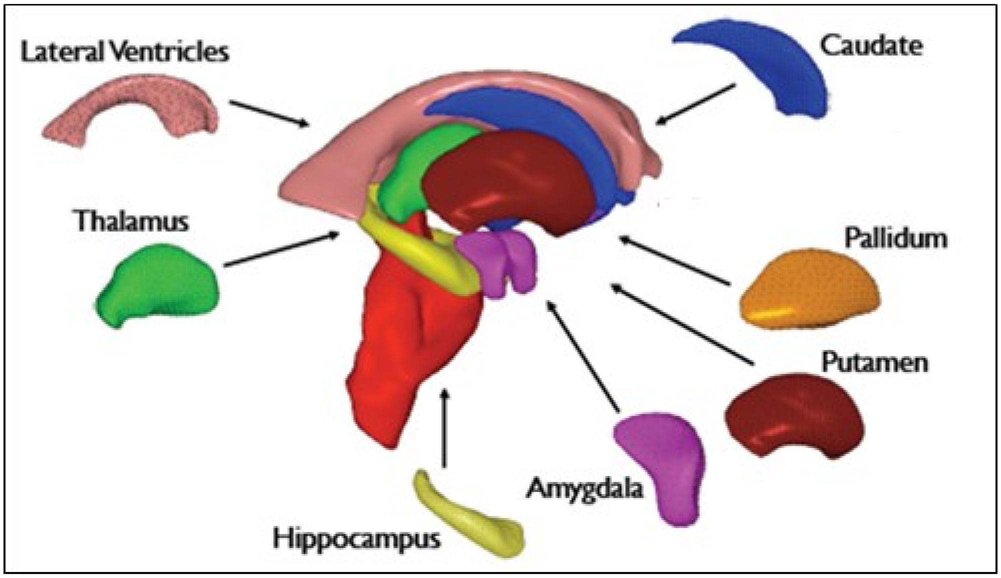

Figure 3.1 Regions will be included in custom elderly atlas. (http://www.fmrib.ox.ac.uk /fslcourse/)

3.2 Creation of Elderly Custom Anatomical Atlas

In order to establish the proposal template, we designed an automated procedure. The customized elderly template was created using the following steps.

1) A good quality MRI scan of a 70 years old, female with no cognitive impairment was chosen as a representative brain (Figure 3.2 (A)).
2) The anatomic template was obtained by normalizing the chosen image to MNI space using a 12-parameter affine transformation and nonlinear transformation within SPM5 (http://www.fil.ion.ucl.ac.uk/spm/software/spm5/), and then reslicing to a voxel size of $1x1x1mm^3$. (Figure 3.2 (B)). This processed image was used as anatomic template for defining our custom anatomic labeling in the following step.
3) The automated segments of ROI on the left and right sides of the anatomic template (Figure 3.2 (C)) were obtained using the "Atlasing" function in IBASPM.
4) The automated segments of 26 regions were examined in the coronal plane slice by slice from anterior-to-posterior and manually edited using publicly available software MRIcroN (http://www.cabiatl.com/mricro/mricron/). Later, each region (left and right) was coded with a specific intensity to obtain a 3D image with custom anatomic labeling (Figure 3.2 (D)). This manual editing of 26 regions followed the published protocol described by Tzourio-Mazoyer *et al.* (2002). However, we defined the anterior-to-posterior extent of the parahippocampal and fusiform region between the anterior commissure and the posterior commissure from the coronal slices for this study, whereas the AAL parahippocampal and fusiform regions extend further

posteriorly (Tzourio-Mazoyer *et al.*, 2002), including regions that are only minimally affected by AD pathology.

5) The normalized image (Figure 3.2 (B)) was smoothed to a lower resolution ($\sigma = 1.9$) so as to generate the custom coordinate template (Figure 3.2 (E))

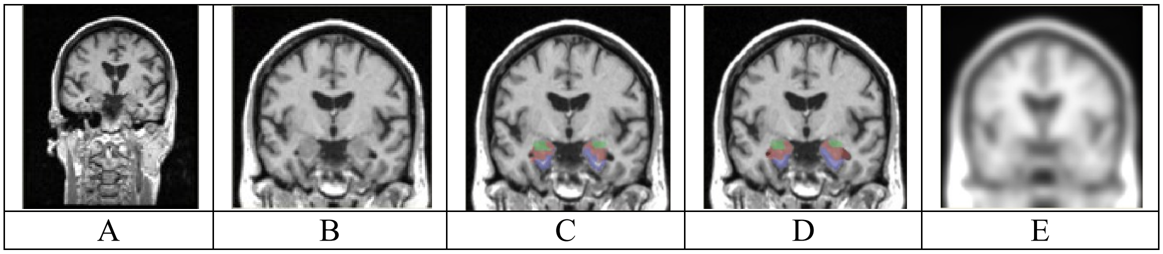

Figure 3.2 (A) A 70-year-old female subject's MRI scan was chosen for generating our custom elderly template set. (B) Anatomic template which is the chosen image normalized to MNI space. (C) Anatomic template with superimposed automated regional segmentation of the hippocampus (in red), parahippocampal gyrus (in violet) and amygdala (in green). (D) Anatomic template superimposed with customized segmentation of the hippocampus (in red), parahippocampal gyrus (in violet) and amygdala (in green). (E) Customized stereotactic template.

Figure 3.3 shows the flowchart of creating a customized elderly template set. It consists of a coordinate template and an anatomical atlas labeling which matches closely the population under our investigation. We name it Template Set E.

The customized elderly anatomical atlas was superimposed on the anatomic template which was a representative subject image spatial normalized to MNI space. Figure 3.4 shows coronal view of the custom elderly atlas superimposed on the anatomic template. Figure 3.5 is the horizontal view of the custom elderly atlas superimposed on the anatomic template. Figure 3.6 is the 3D rendering of the anatomic atlas. The customized elderly anatomical atlas includes 26 regions.

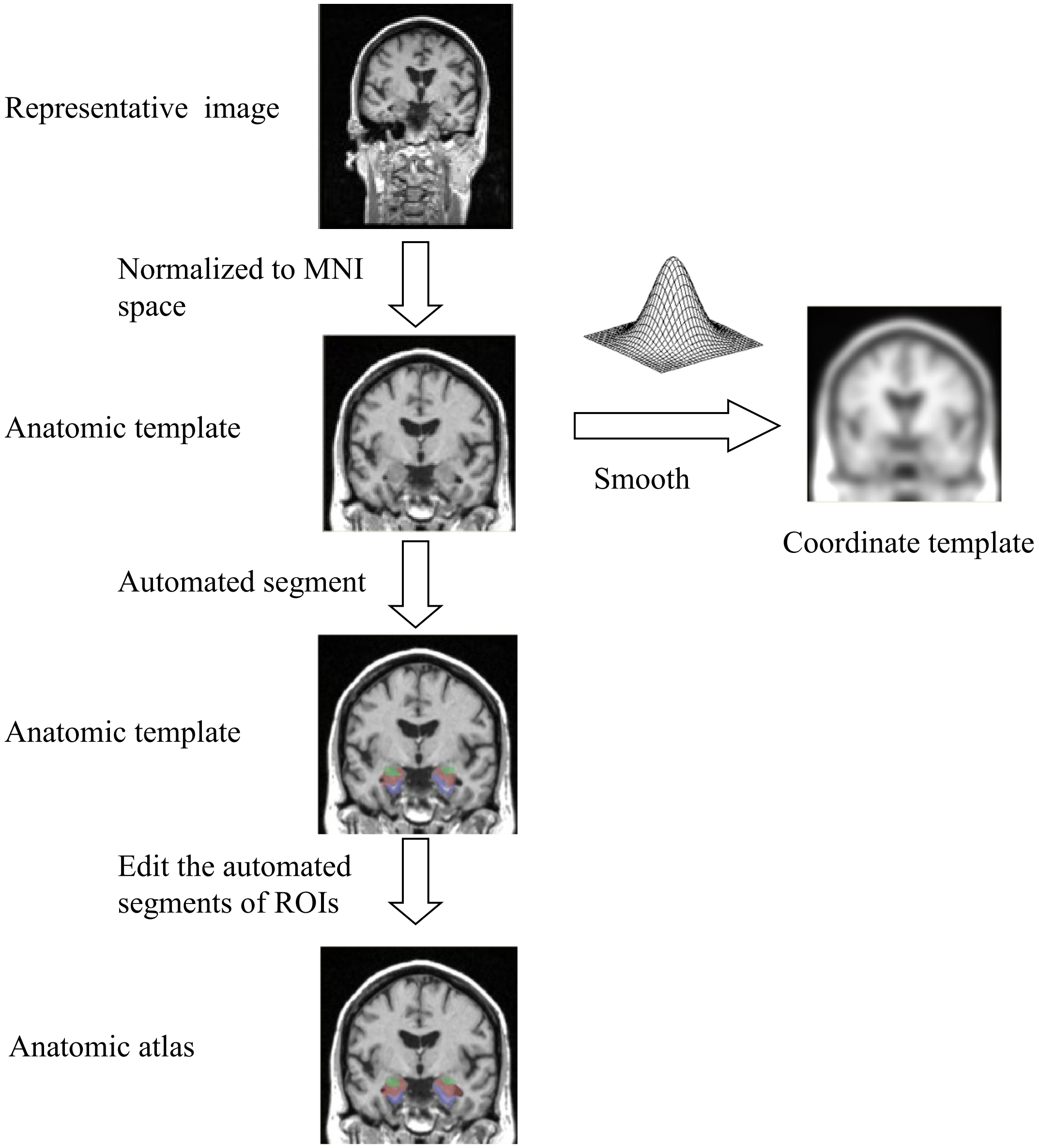

Figure 3.3 Flowchart of creating a customized elderly template set. It consists of a coordinate template and an anatomical atlas labeling which matches more closely the population under our investigation.

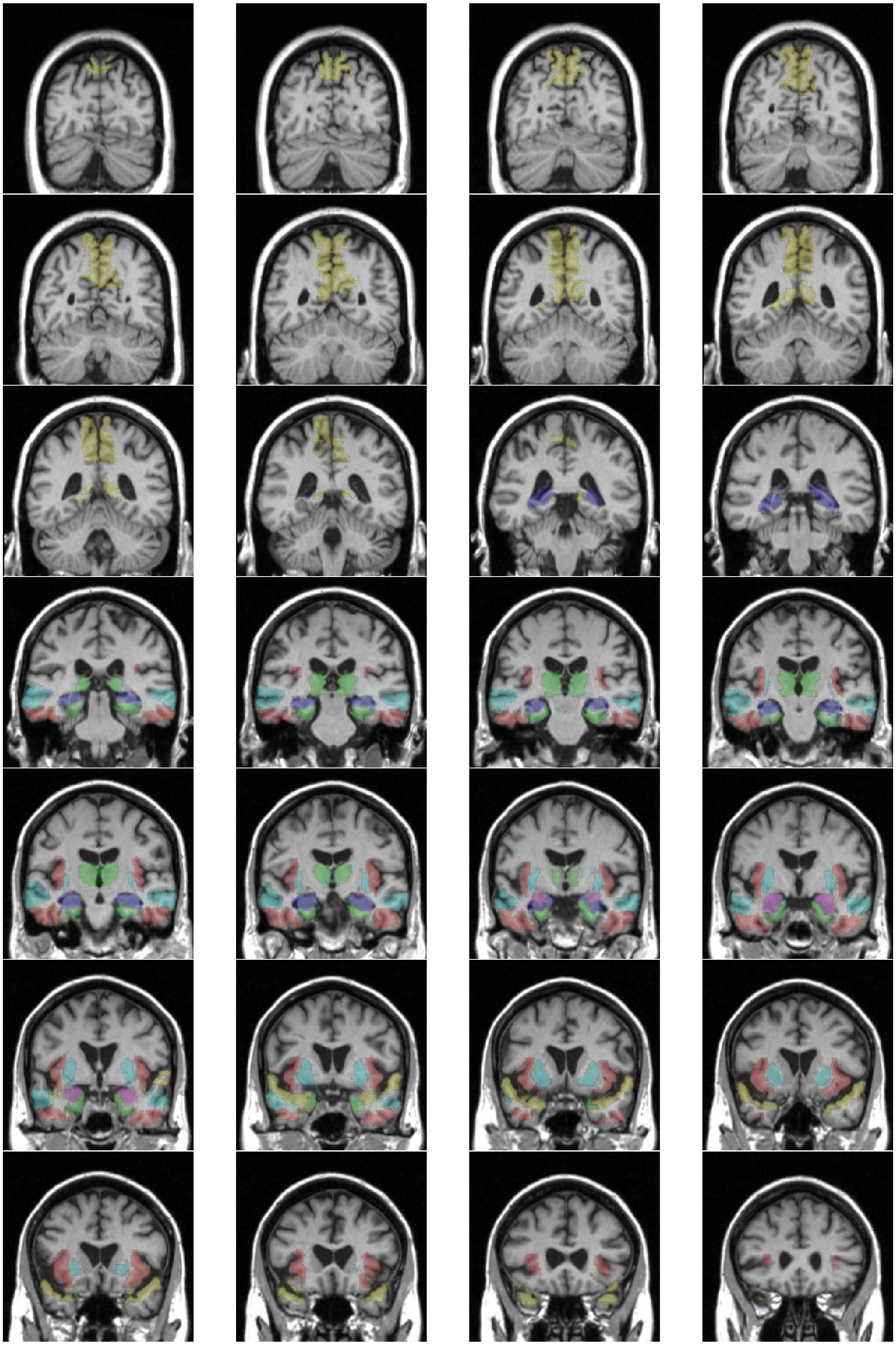

Figure 3.4 Coronal view of the custom elderly atlas superimposed on the anatomic template.

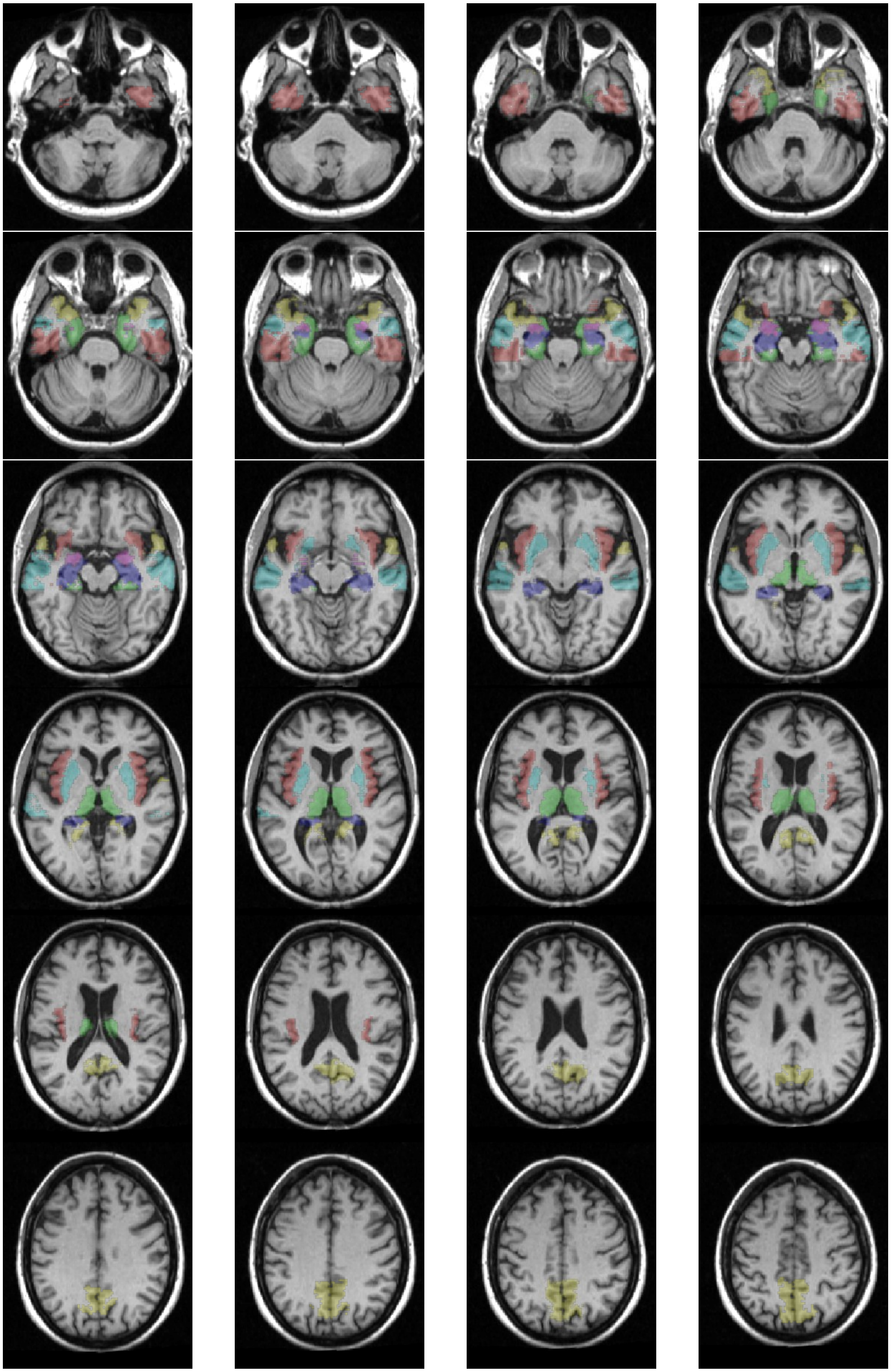

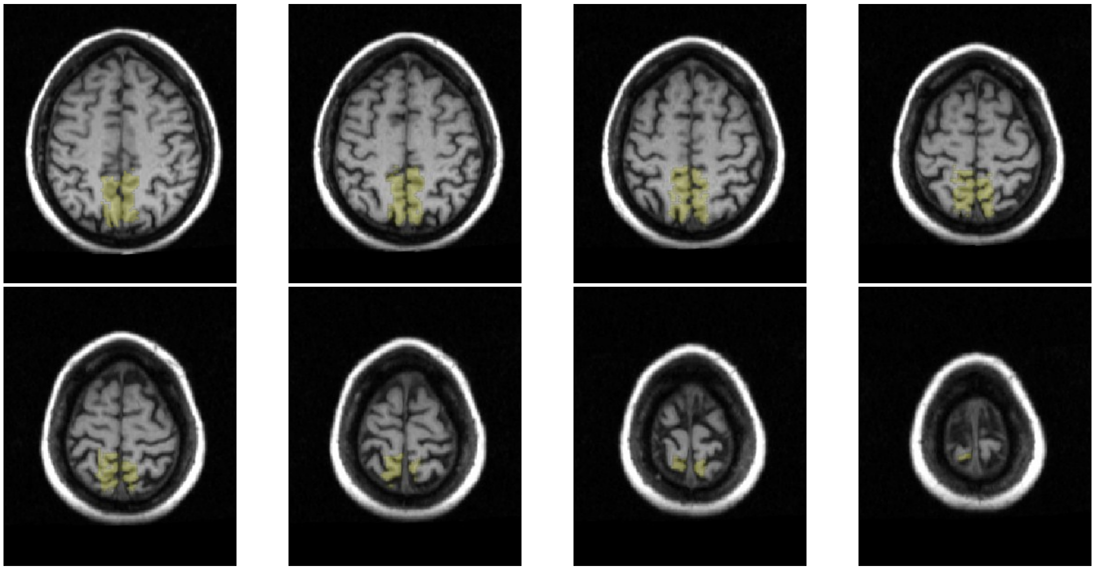

Figure 3.5 Horizontal view of the custom elderly atlas superimposed on the anatomic template.

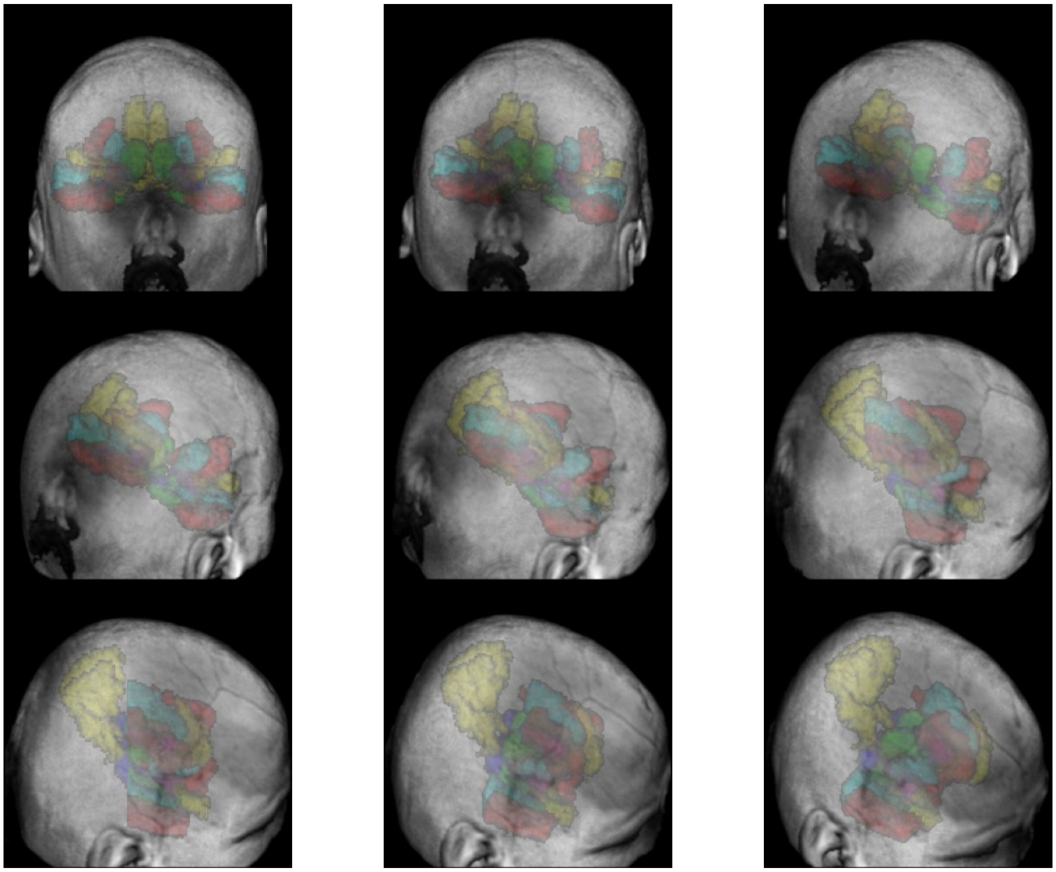

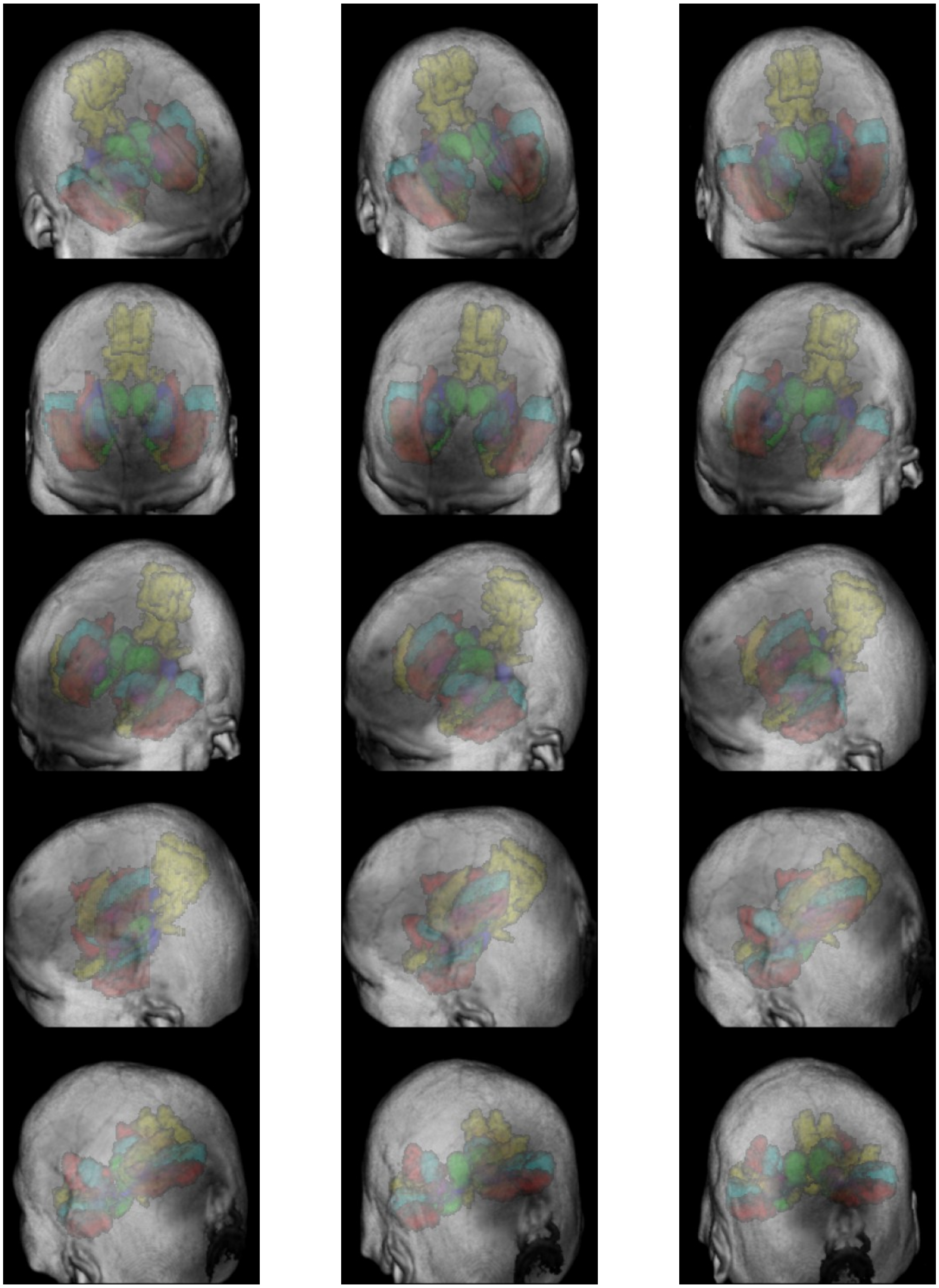

Figure 3.6 3D rendering of the anatomic atlas.

3.3 Creation of Elderly Custom Tissue Class *prior*s

The MNI *a priori* probability images of GM, WM and CSF (see Figure 2.3) are derived from the T1-weighted images of 152 healthy subjects, of which 57% were male, 90% were right handed and with a mean age of 25 years. However, the subjects enrolled in our study are over 65 years old. Previous studies have confirmed that there are significant anatomic differences between young adult brains and aged adult brains. To avoid induce bias errors in the tissue segmentation procedure by using the MNI *a priori* tissue images from young subjects, it is important to create the custom GM, WM and CSF priors specifically suited for the elderly who are being studied.

The procedures used for construction of the custom three tissue priors are depicted schematically in Figure 3.7 and proceeds as follows:

1) Ten health subject's MRI scans are spatial normalized to the new coordinate template which is created in chapter 2, and then re-slicing to a voxel size of 1x1x1mm^3;

2) Segment the re-sliced spatial normalized images to GM, WM and CSF using the MNI priors;

3) Binary these GM, WM and CSF images;

4) Average the binary GM, WM, and CSF images respectively;

5) Apply a 6-mm FWHM Gaussian smoothing kernel to the averaged images to obtain the custom GM, WM, and CSF priors.

The customized GM, WM and CSF priors images are shown in Figure 3.8 in coronal views.

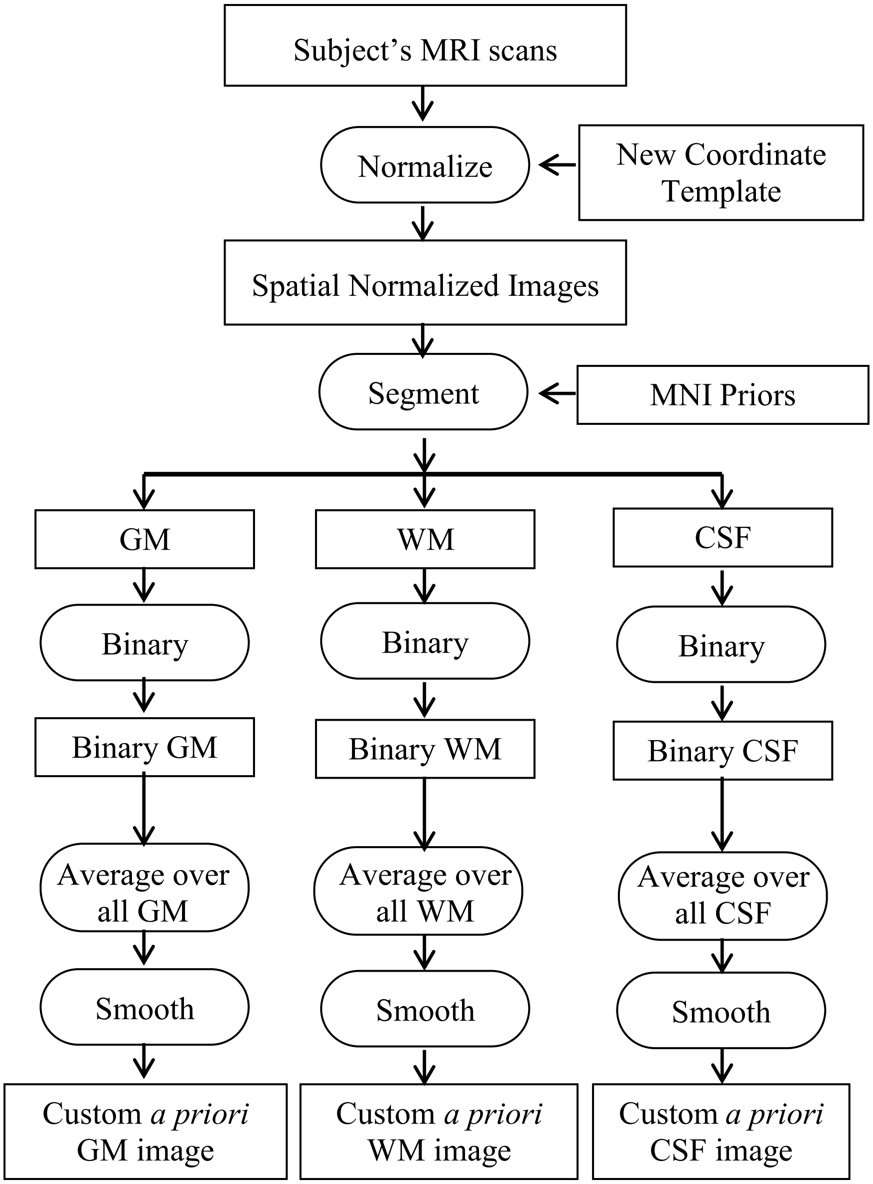

Figure 3.7 Flowchart of creating a customized GM, WM and CSF priors.

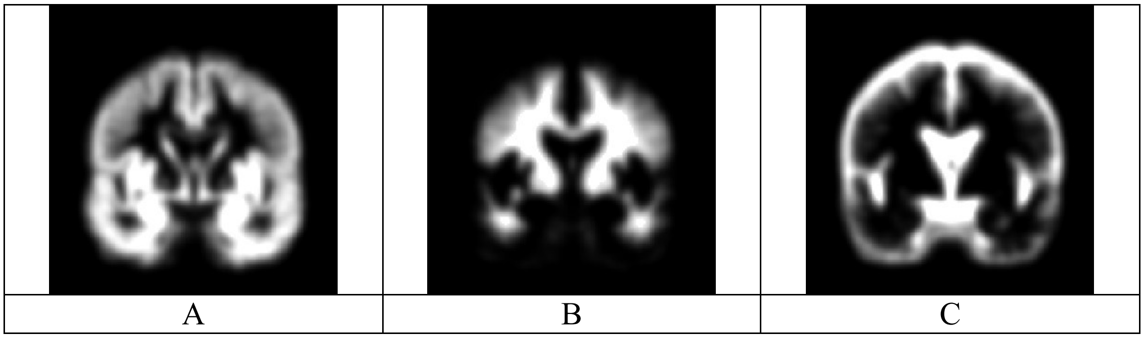

Figure 3.8 Coronal views of the customized GM (A), WM (B) and CSF (C) priors.

Chapter 4 Development of an Automated Area Measure on a Single Coronal Slice

4.1 Visual Rating System

Studies have shown that the neuropathology of AD begins in the medial temporal lobe (Apostolova *et al.*, 2007; Mosconi *et al.*, 2007). With the use of high-resolution quantitative MRI techniques, it is possible to directly visualize the hippocampus and other critical MTL structure in substantial cytoarchitectonic detail (Frisoni *et al.*, 2003).

Visual rating system (VRS) developed in the Wien Center for Alzheimer's Diseases and Memory Disorders at Mount Sinai Medical Center (Miami Beach, Florida) to standardize ratings of atrophy of individual structures of interest (Urs, 2006; Duara *et al.*, 2008, Urs *et al.*, 2009) is a JAVA application. It is user-friendly, easily operated on a PC or radiology console, and does not require special technical support. Ratings of atrophy are given based on 1.5 mm or less thick coronal MRI slices that were reconstructed in the coronal plane perpendicular to the anterior commissure-posterior commissure (AC-PC) line. Ten coronal slices are selected using easily identifiable landmarks for rating of various brain regions. Figure 4.1 shows the interface of VRS. Figure 4.2 shows the high resolution single-subject MR images in standard MNI space to show the locations of five cornel slices at sagittal view image (red lines in left image), and the five coronal slices pCC (Post border of Corpus Callosum), PC (Posterior Commissure), MB (Mammillary Bodies), AC (Anterior Commissure) and aCC (Anterior border of Corpus Callosum) are showing on right side from top to bottom.

VRS ratings are based on a five point scale, with "0" signifying no atrophy, and "4" signifying the most severe atrophy. A library of reference images that define the anatomical boundaries of each brain structure and depict different levels of atrophy are provided from a drop-down menu in the system interface. This facilitates a direct comparison of each structure on the subject's MRI. VRS enables digital entry of atrophy ratings that are automatically saved to an Excel file.

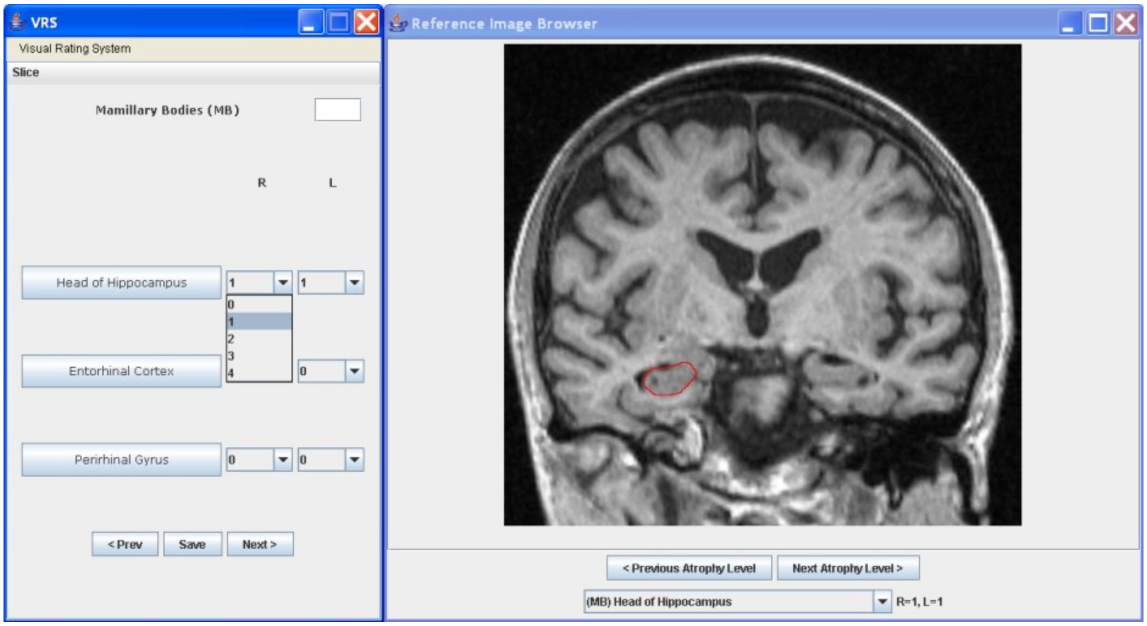

Head of Hippocampus R 1 L 1

Entorhinal Cortex L 0

Perirhinal Gyrus R 0 L 0

(MB) Head of Hippocampus R=1, L=1

Figure 4.1 VRS interface. Window in left side is for inputting the rate of atrophy of brain structure that can be automatically saved to an Excel file. Window in right side is for displaying the reference images that define the anatomical boundaries of each brain structure and depicts different levels of atrophy.

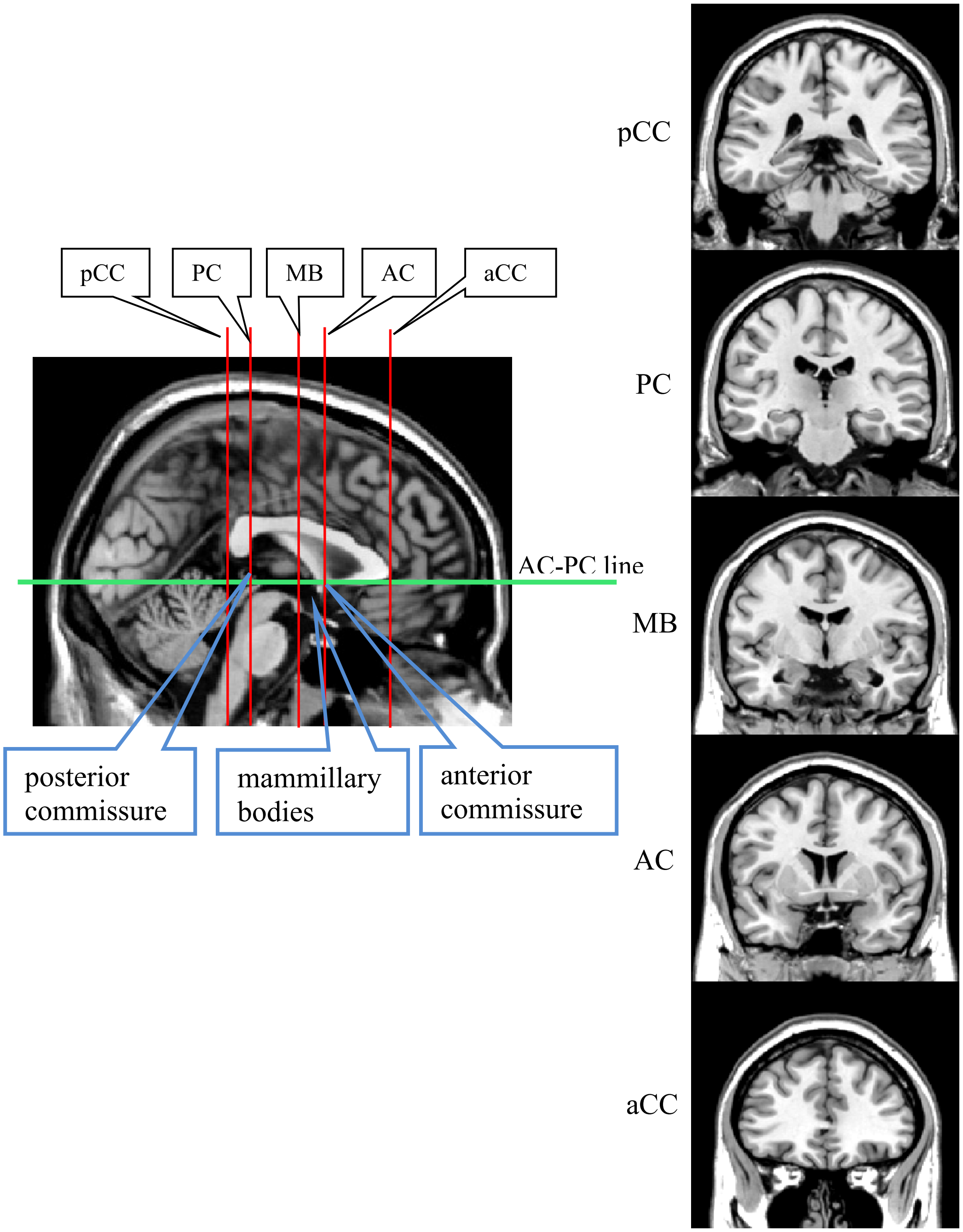

Figure 4.2 The high resolution single-subject MR images in standard MNI space are employed here to show the locations of pCC, PC, MB, AC and aCC coronal slices of VRS (see the red lines on the sagittal brain view image). The pCC, PC, MB, AC and aCC coronal slices are shown on right from top to bottom. pCC = Post border of Corpus Callosum; PC= Posterior Commissure; MB = Mammillary Bodies; AC= Anterior Commissure; aCC= Anterior border of Corpus Callosum. The AC-PC line (see the green lines at sagittal brain view image) goes from the superior surface of the anterior commissure to the center of the posterior commissure, according to the Talairach Atlas rules.

Atrophy first appears in the medial temporal lobe structures in AD patients. Specifically, the earliest pathological changes of AD occur at the Cornu Ammonis (CA) areas CA1 sector of the adjacent head of the hippocampus (Leverenz *et al.*, 1998), which can be visualized on the coronal MB slice that intersects the mammillary bodies (Figure 4.3). In contrast, volumetric analysis focuses on the entire hippocampal structure, averaging the most anterior aspects with the less affected middle and posterior regions of the HPC. In primates, lesions in the entorhinal cortices and CA1 sector of the HPC cause the most severe impairment in memory test performance (Zola-Morgan *et al.*, 1989; 1993). Several studies using MRI have shown that atrophies in the entorhinal cortices and inferior temporal cortex, which is immediately lateral to the perirhinal cortices, in addition to HPC atrophy, are among the earliest structural changes that distinguish mildly impaired AD subjects from cognitively normal elderly individuals (Desikan *et al.*, 2009; Krasuski *et al.*, 1998).

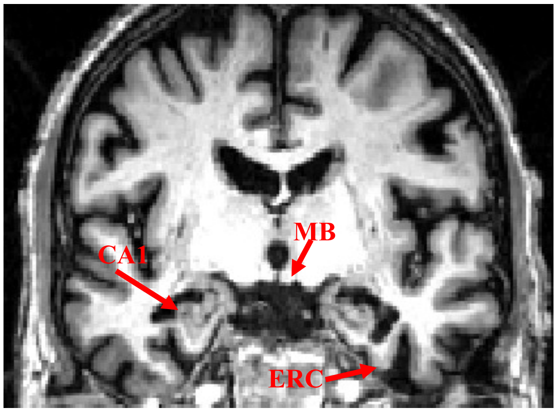

Figure 4.3 Coronal MB slice used for assessment of medial temporal lobe atrophy. CA = Cornu Ammonis; MB = mammillary bodies; ERC = entorhinal cortices.

Since VRS ratings of the MB coronal slice have been shown to be valuable in the assessment of medial temporal lobe atrophy, we aim to develop an automatic method to mimic what is done in the VRS assessment of HPC. The automatic method would initially select the MB slice and then assign a VRS rating to the HPC. Automatic assessment of the atrophy of HPC on MB should reduce inter-rater variability caused by (1) operators who may not agree on which MB slice to select and (2) variance among human raters in assigning atrophy levels.

4.2 Methods

The definition of automated hippocampal area measurement on a single coronal slice is crucial. When neuroimaging experts evaluate hippocampal atrophy, they take into account what a normal hippocampus should look like. Also, experts are aware of nearby adjacent changes (e.g. variation of CSF) resulting from atrophy. Further, the size of the brain is different from individual to individual, and so is the area of the hippocampus, such as the area inside of the red boundaries in Figure 4.4 on a single coronal slice. It is noticed that there is almost no hippocampal temporal horn the area inside of the green boundaries (Figure 4.4.) in the NCI brain. However, there is a usually a large increase in temporal horn size during the transition from MCI than NCI. The increase of the hippocampus temporal horn and the decrease of the hippocampus reinforce the evidence of accelerated MTL atrophy. Therefore, we define a novel ratio RHPA (ratio of hippocampal area) as the measurement,

$$\text{RHPA}=\frac{\text{HP}}{\text{HP}+\text{HP\_TemproalHorn}} \tag{4.1}$$

Where, HP is the number of pixels within the hippocampus (Figure 4.4 Area inside of the red boundaries), and HP_TemporalHorn. The area inside of the green boundaries in

Figure 4.4 is the number of pixels within the anterior temporal horn of the lateral ventricle, which includes CSF.

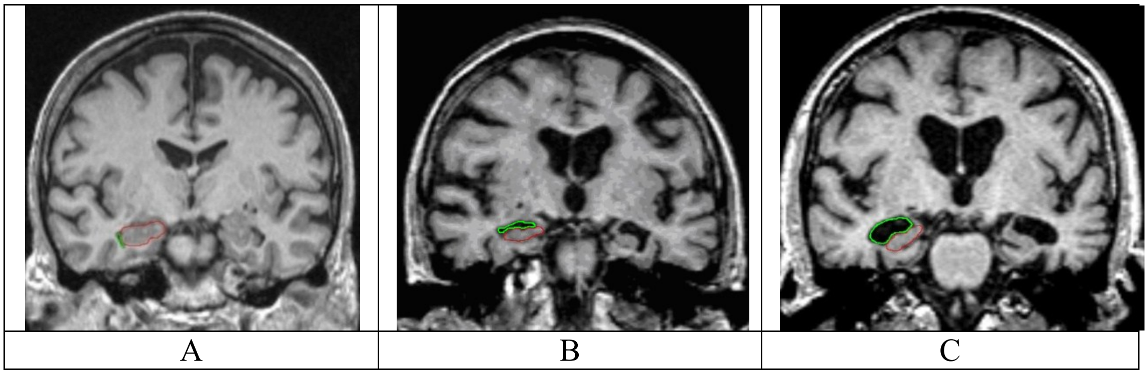

Figure 4.4 Coronal MRI scan (MB slice) of subjects, showing the anatomical boundaries used in RHPA in the right hemisphere for the hippocampus (red) and hippocampus temporal horn (green). (A) NCI; (B) MCI, and (C) AD.

A method was developed to locate the coronal MB slice of a subject's MRI scan automatically. The coronal MB slice is where the mammillary bodies (Figure 4.3. and Figure 4.5.) present and are bigger than in adjacent coronal slices. The coordinates (y_1, y_2, y_3) of the mammillary bodies in coordinate template are known and they can be converted to the individual subject's MRI space based on the spatial normalization parameters (T) (see Figure 4.6).

$$(x_1, x_2, x_3) = T(y_1, y_2, y_3) \tag{4.2}$$

where, (x_1, x_2, x_3) are the coordinates of the mammillary bodies in the individual subject's MRI space. The mammillary bodies, which are transformed from the coordinate space red spots in Figure 4.6 left side, will present on several adjacent coronal slices in Figure 4.6 right side. The MB slice is selected the one with the biggest mammillary bodies area. The equation is given by:

$$(\hat{\mathbf{x}}) = \arg\max_{\mathbf{x}}(\text{area of mammillary bodies }(\mathbf{x})) \tag{4.3}$$

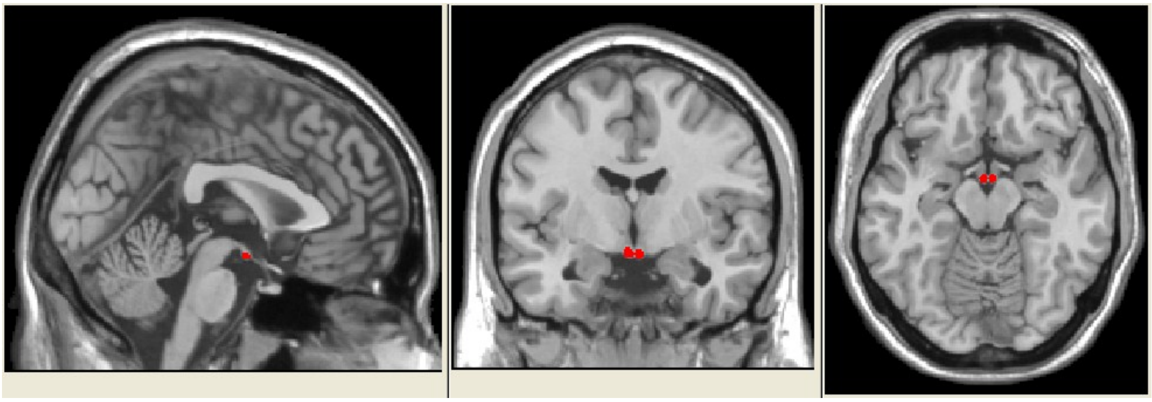

Figure 4.5 Mammillary bodies (red spots) on anatomic template. Fragment of sagittal (left column), coronal (center column), and axial (right column).

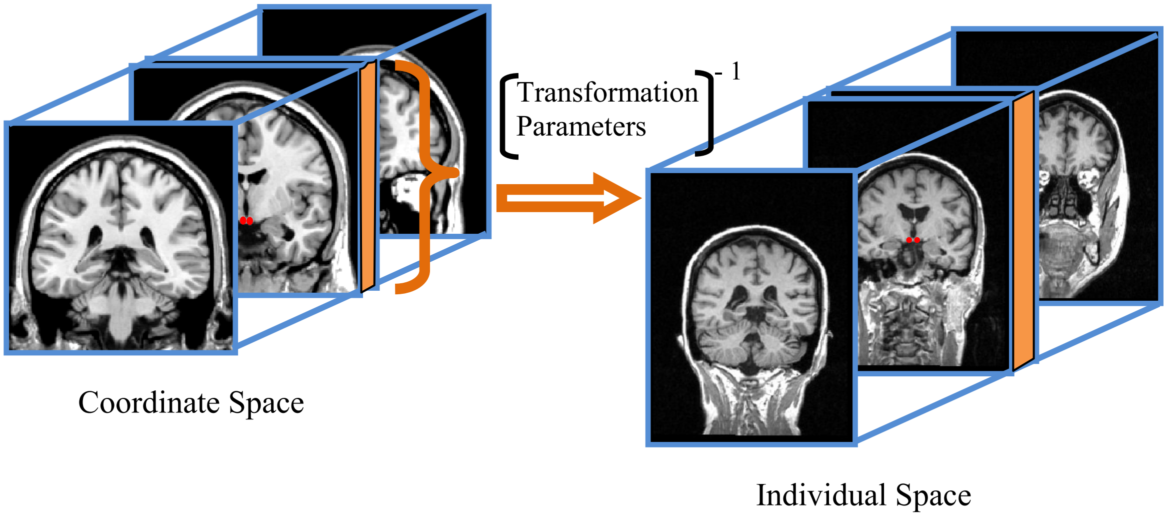

Figure 4.6 Mammillary bodies (red spots) on anatomic template transformed from coodinate space to individual subject's MRI space are present on several adjacent coronal slices. The MB slice is selected the one with biggest mammillary bodies area.

4.3 Results of Automated Choosing MB Slice

Figure 4.7 shows the results of automatically choosing the MB slice on 241 subjects which were chosen by convenience from the Wien Center for Alzheimer's Diseases and Memory Disorders at Mount Sinai Medical Center (Miami Beach, Florida) (see section 5.2). Altogether, in 102 cases the automatic method chose the same slice as the expert human operator and in 91 cases there was a difference of one slice. A difference of one slice may be tolerable, because the thickness of the subjects' MRI scan is 1.5 mm or less. A one slice error will not cause large differences in the measurement of RHPA. Even trained raters will not always agree on what is the MB slice. Nevertheless, there were 48 cases which were off by two slices or more. These cases need to be improved.

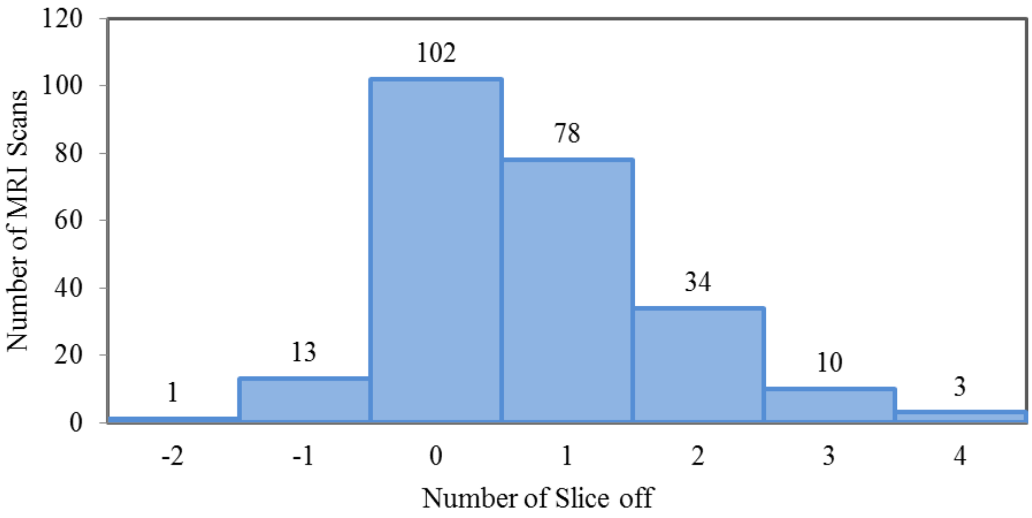

Figure 4.7 The results of automatically choosing MB Slice on 241 subjects. The automatic method chooses the same slice as the expert human operator for 102 cases. And there is one slice difference for 91 cases (13 cases are anterior, 78 cases are posterior to the one chose by the expert human operator). In the rest cases, there are more than two slices off the one that is chosen by the expert human operator.

Chapter 5 Clinical Application of Cognitive Impairment

5.1 Materials and Methods

The atlas-based automated segmentation of ROIs and area measurements on a single coronal slice have been applied to the cross-sectional studies of a large cohort of clinical cognitive impairment subjects with NCI, naMCI, aMCI, and early AD. The methods were tested and validated by the following ways:

1) Atlas-based segmentation on a randomly selected older subject was compared using three template sets: MNI template set (consists of MNI coordinate template and AAL anatomical atlas), template set S (consists of the new coordinate template and AAL anatomical atlas) and template set E (consists of the customized elderly coordinate template and customized elderly anatomical atlas). The correspondence of hippocampus and amygdala volume with manual segmentation was used for validation.

2) Atlas-based segmentation using three template sets (MNI template, template set S and template set E) was performed on 241 subjects. The correlation of regional volumes with the cognitive test MMSE and the clinical dementia rating was used to compare the performance of templates. The ability of the templates to distinguish diagnostic groups was also used as a metric of validation.

3) The automated area measurements on MB slice were compared with VRS ratings from the same slice on a total of 241 subjects. Also, the performance of these automated area measurements were compared with volumetric measurement using template set E.

4) In a subset of 80 subjects, the performance of these atlas-based segmentations using three template sets was compared with Neuroquant^{TM} (CorTechs Labs Inc, La Jolla, CA).

This is a commercial software product that provides full volume segmentation of 10 subcortical brain regions in each hemisphere.

Among the experiments mentioned above, the customized GM, WM and CSF priors is used in the procedure of segmentation three brain tissues when applying the template set E in atlas-based segmentation.

Because brain size differs from one individual to another, the region of interest volume is normalized before conducting statistical analyses. Each region of interest volume is adjusted to the total intracranial volume, which is the sum volume of the gray matter, white matter, and cerebrospinal fluid.

5.2 Subjects and MR Acquisition

Total of 241 male and female subjects, 65 years of age or older, were chosen by convenience from the Wien Center for Alzheimer's Diseases and Memory Disorders at Mount Sinai Medical Center (Miami Beach, Florida). The study was approved by the Mount Sinai Medical Center Institutional Review Board. All subjects and/or a legal representative signed informed consent. All subjects were evaluated with a full battery of neuropsychological tests and a neurological evaluation, which included: 1) Mini-Mental State Examination (MMSE) (Folstein *et al.*, 1975) (MMSE; an MMSE score of 20 or greater was required to enter this study); 2) a neuropsychological test battery (Loewenstein *et al.*, 2000), following the National Alzheimer's Coordinating Center (NACC) protocol (http://www.alz.washington.-edu/), and Three Trial Fuld Object Memory Evaluation (Fuld *et al.*, 1981), Hopkins Verbal Learning Test (Lacritz *et al.*, 2001); and 3) an underwent brain MR imaging. The demographics and clinical characteristics of subjects are displayed in Table 5.1. Group comparisons of means of age, MMSE Score and CDR-sb were examined using one-way analysis of variance (ANOVA). Scheffe' post-hoc procedure was used to examine differences between means. Dichotomous variables gender was analyzed using χ^2 tests (see superscripts in Table 5.1). Statistical analyses were implemented in SPSS 17.0 for Windows software (SPSS Inc, Chicago, IL).

Table 5.1 Demographic variables of diagnostic groups (N=241).

Diagnostic Group	NCI (N=103)	naMCI (N=24)	aMCI (N=68)	AD (N=46)	F-Value
Age Mean (SD)	70.8^{a} (5.3)	75.1^{b} (6.6)	76.8^{b} (5.8)	79.1^{b} (7.1)	26.3*
Gender (% Female)	75.7%	45.8%	51.4%	58.7%	15.4*(χ2)
MMSE Score Mean (SD)	29.1^{a} (1.0)	25.6^{b} (3.1)	26.2^{b} (2.2)	22.3^{c} (3.3)	107.7*
CDR-sb Mean (SD)	0.60^{a} (0.56)	2.09^{b} (1.18)	2.50^{b} (1.74)	5.30^{c} (2.63)	110.0*

NCI= No Cognitive Impairment; naMCI=Non-Amnestic MCI, aMCI=Amnestic MCI. Note: *p<.001; Means with different alphabetic superscripts are statistically significant at p<.05 by the Scheffe' procedure. MMSE= Mini-Mental Status Examination; CDR-sb= Clinical Dementia Rating - sum of boxes

The cognitive and etiological diagnoses were made by consensus conference. The diagnosis of probable AD satisfied the NINCDS-ADRDA criteria for Alzheimer's disease (McKhann *et al.*, 1984). The diagnosis of amnestic MCI (aMCI) satisfied the Petersen criteria (Petersen *et al.*, 1999). The diagnosis of no cognitive impairment (NCI) required that informants reported "no significant decline in cognition or functional ability," and no cognitive test scores were 1.5 SD or more, below the age and education corrected means. The non-amnestic MCI (naMCI) diagnosis required that all memory test scores were higher than 1.5 SD below education-corrected normative values, but one or more non-memory test scores were 1.5 SD or more below normal values.

The subjects’ MRI brain scans were obtained on a 1.5 Tesla MRI machine using: a) proprietary 3-D MPRAGE (Siemens), or 3-D SPGR (General Electric) sequences to acquire contiguous coronal slices that were 1.5 mm or less in thickness. 3-D MPRAGE sequence scans were reconstructed in the coronal plane perpendicular to the AC-PC line. Fluid Attenuated Inversion Recovery (FLAIR) sequences were used to obtain axial slices. FLAIR sequences were as follows: TR/TE (ms) = 9000/109; T1 = 2500ms; flip angle = 150degrees; matrix = 144 × 256; FOV = 230mm; phase FOV = 75%; 20 slices from top of skull to magnum foramen; 5.5mm slices; slice interval 1.9mm; BW = 130 Hz/pixel; phase direction = right to left; acquisition time = 2 min 44 sec.

5.3 Experiment 1: Correspondence of HPC and AMG Volumes Using Manual Segmentation and Atlas–Based Automated Segmentation

An 89-year-old male subject’s MRI scan was randomly chosen to compare the correspondence of the manually delineated hippocampal (HPC) and amygdala (AMG) volume to automated segmentation using three template sets: MNI template set, template S set and template E set.

The automated segments were superimposed on the subject’s MRI scan (see Figure 5.1). Hippocampus is in red and amygdala is in blue. It can be seen by visual inspection that segmentation of the hippocampus and amygdala using the MNI template set results in large errors of anatomical definition, with the hippocampus and amygdale being displaced anteriorly and superiorly in comparison to placement using the template S set and template E set.

Next, several widely used quantitative measures for volume comparisons (the Dice similarity index [D]; False positive error [FP]; False negative error [FN]; Volume similarity coefficient [VS]) were employed to compare the automatic segmentation with the gold standard manual segmentations (Table 5.2). Comparisons of D, FP, FN and VS values for HPC and AMG volumes cross the three template sets were listed in Table 5.2. With few exceptions, the largest errors were found using the MNI template set and the smallest errors were found with template E set; Template S set yielded results that were intermediate between the MNI template and template E set.

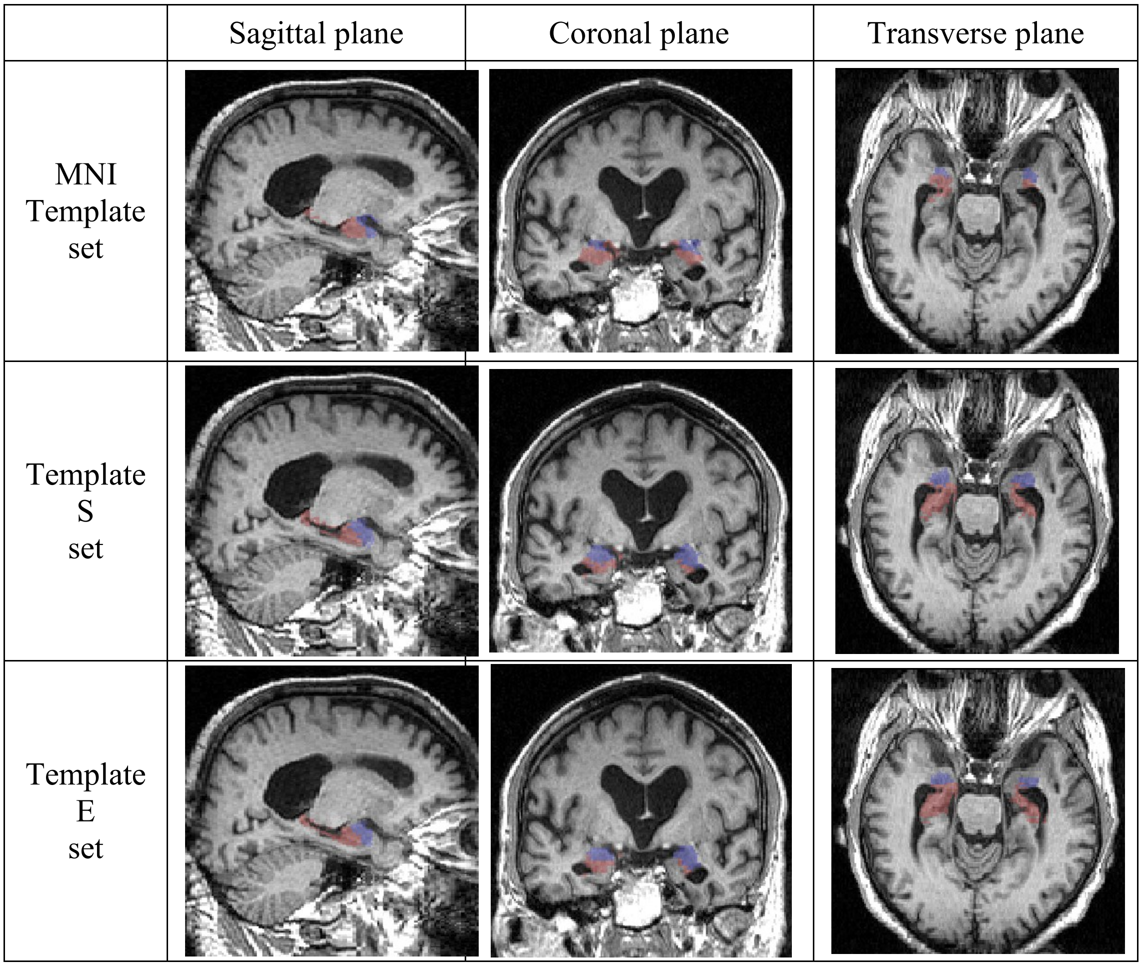

Figure 5.1 An 89-year-old male subject's MRI scan was randomly picked to assess the correspondence of the manually delineated hippocampus and amygdala volume to automated segmentation using MNI Template set, Template S set and Template E set. The automated segments were superimposed on the subject's MRI scan. Hippocampus is

in red, and amygdala is in blue. Visually, the automated delineation of the hippocampus and amygdala using Template S set and Template E set were better than MNI Template set.

Table 5.2 Segmentation quality indices for the three Template Sets

Template	ROI	D	FP	FN	VS
MNI Template Set	Left HPC	0.51	0.42	0.56	0.13
	Right HPC	0.35	0.54	0.75	0.19
	Left AMG	0.61	0.24	0.53	0.25
	Right AMG	0.54	0.42	0.49	0.06
Template S Set	Left HPC	0.77	0.20	0.25	0.05
	Right HPC	0.73	0.22	0.32	0.10
	Left AMG	0.84	0.11	0.20	0.09
	Right AMG	0.81	0.13	0.25	0.11
Template E Set	Left HPC	0.80	0.10	0.19	0.02
	Right HPC	0.73	0.27	0.27	0.01
	Left AMG	0.93	0.10	0.04	0.06
	Right AMG	0.93	0.10	0.04	0.06

ROI = Region of Interest; HPC = Hippocampus; AMG= Amygdala; D= Overlap Ratio; FP = False Positive Ratio; FN = False Negative Ratio; VS =Volume Similarity Index Coefficient;

5.4 Experiment 2: Cross-sectional Studies on 241 Subjects - Volumetric Analysis

In this experiment, three template sets were applied to the automated segmentations of three tissues and 24 brain regions (two more regions: left ventricle and right ventricle for template set E) on a large cohort of subjects with NCI, naMCI, early aMCI, and AD. The demographic variables of subjects are listed in Table 5.1. Pearson Correlation Coefficients were employed to compare volumetric measures to indices of memory and severity of clinical impairment. Comparison of the three methods to classify subjects in different diagnostic groups was conducted by comparison of the area under the receiver operating curve (ROC). This (ROC) analyses was conducted to determine the extent to which volumetric measures could distinguish between NCI,naMCI, aMCI and AD groups.

5.4.1 Comparisons of Normalized Volumes by Diagnostic Groups

Normalized volumes (mean±SD) for the four groups using template set E set, template S set and MNI template set are shown Table 5.3, Table 5.4 and Table 5.5 respectively. Group differences were examined using ANOVA. Post-hoc tests of means by Scheffe' analyzed the effect of four diagnostic groups (NCI, naMCI, MCI and AD) on all these measurements. see superscripts in Table 5.3, Table 5.4 and Table 5.5. Statistical analyses were implemented in SPSS 17.0 for Windows software (SPSS Inc, Chicago, IL).

Data shown in Table 5.4 and Table 5.5 include three tissue types and 24 regions. Those 24 regions are all located in the grey matter and are predefined in AAL. Data shown in Table 5.3 derived from the template S set includes two more regions: left and right ventricles which were included in atlas E, but not in AAL.

In general, normalized volumes using template E show a greater difference of the means between diagnostic groups (based on highest F value), with few exceptions (ParaHippocampal and Thalamus). Template S set yielded results that were intermediate between the MNI template and template E set.

The data derived from template E set and from template S set both show that the "No Cognitive Impairment" (NCI) group has the largest mean hippocampus and amygdala volumes on both sides, and the dementia group has the smallest mean hippocampus and amygdala volumes on both sides. This demonstrates the effect of the severity of disease (presumably AD) on the degree of atrophy seen on MRI scans. In general, using template

S set and template E set, the HPC and AMG volumes are significantly larger in the NCI group than in the other three diagnostic groups ($p<0.05$), and the volumes in the dementia group are smaller than in the others three groups ($p<0.05$). Only the naMCI and aMCI groups do not have significantly different volumes.

Table 5.3 Normalized volumes by diagnostic groups using Template E Set.

	Brain Regions	NCI (N=103)	naMCI (N=24)	aMCI (N=68)	AD (N=46)	F-Value (df=3,237)
Template E Set	GM	458.2^{a}	$431.1^{a,b,c}$	$424.6^{b,c}$	$428.1^{b,c}$	8.9*
	(SD)	(46.5)	(47.6)	(36.7)	(59.5)	
	WM	298.6	298.5	299.6	282.1	3.0
	(SD)	(26.0)	(23.3)	(23.5)	(59.8)	
	CSF	243.2^{a}	270.4^{b}	275.8^{b}	289.8^{b}	17.8*
	(SD)	(42.3)	(39.6)	(36.2)	(40.1)	
	Hippocampus L	2.99^{a}	2.73^{b}	2.59^{b}	2.26^{c}	52.5*
	(SD)	(0.29)	(0.33)	(0.33)	(0.46)	
	Hippocampus R	2.80^{a}	2.51^{b}	2.38^{b}	2.12^{c}	35.5*
	(SD)	(0.38)	(0.30)	(0.37)	(0.49)	
	Amygdala L	0.96^{a}	$0.93^{a,b}$	0.91^{b}	0.81^{c}	36.5*
	(SD)	(0.07)	(0.08)	(0.08)	(0.11)	
	Amygdala R	0.98^{a}	$0.92^{b,c}$	$0.91^{b,c}$	0.86^{c}	22.9*
	(SD)	(0.09)	(0.09)	(0.08)	(0.11)	
	ParaHippocampal L	1.83	1.77	1.76	1.65	4.8
	(SD)	(0.29)	(0.22)	(0.24)	(0.29)	
	ParaHippocampal R	2.49^{a}	$2.37^{a,b}$	2.36^{b}	2.39^{b}	8.9*
	(SD)	(0.31)	(0.23)	(0.28)	(0.30)	
	Insula L	5.26^{a}	4.77^{b}	4.80^{b}	4.74^{b}	16.8*
	(SD)	(0.45)	(0.49)	(0.46)	(0.74)	
	Insula R	5.14^{a}	4.67^{b}	4.70^{b}	4.72^{b}	15.1*
	(SD)	(0.47)	(0.46)	(0.42)	(0.67)	
	Fusiform L	1.38^{a}	1.36^{a}	1.32^{a}	1.22^{b}	10.1*
	(SD)	(0.19)	(0.15)	(0.14)	(0.19)	
	Fusiform R	1.85^{a}	1.78^{a}	1.77^{a}	1.66^{b}	9.0*
	(SD)	(0.22)	(0.18)	(0.17)	(0.24)	
	Precuneus L	6.41	6.13	6.07	5.94	5.0
	(SD)	(0.75)	(0.86)	(0.72)	(0.83)	
	Precuneus R	5.97^{a}	$5.61^{a,b}$	5.41^{b}	5.52^{b}	9.2*
	(SD)	(0.71)	(0.73)	(0.65)	(0.89)	
	Putamen L	2.50	2.35	2.33	2.36	2.7
	(SD)	(0.35)	(0.44)	(0.35)	(0.65)	
	Putamen R	2.20	2.03	2.03	2.06	3.6
	(SD)	(0.30)	(0.34)	(0.31)	(0.56)	

	Thalamus L (SD)	2.45^{a} (0.33)	2.21^{b} (0.32)	2.18^{b} (0.31)	2.06^{b} (0.36)	18.7*
	Thalamus R (SD)	2.32^{a} (0.35)	2.09^{b} (0.33)	$2.00^{b,c}$ (0.27)	1.85^{c} (0.38)	25.7*
	Temporal_Sup L (SD)	2.99^{a} (0.42)	2.68^{b} (0.27)	2.65^{b} (0.29)	2.53^{b} (0.38)	21.9*
	Temporal_Sup R (SD)	4.12^{a} (0.58)	3.61^{b} (0.53)	3.56^{b} (0.48)	3.45^{b} (0.55)	23.1*
	Temporal_Pole_Sup L (SD)	2.52^{a} (0.32)	$2.41^{a,b}$ (0.30)	2.26^{b} (0.39)	1.94^{c} (0.57)	24.2*
	Temporal_Pole_Sup R (SD)	2.53^{a} (0.31)	$2.45^{a,b}$ (0.30)	2.30^{b} (0.37)	2.04^{c} (0.52)	19.1*
	Temporal_Mid L (SD)	4.88^{a} (0.63)	$4.56^{a,b}$ (0.40)	$4.50^{a,b}$ (0.39)	4.47^{b} (0.64)	9.5*
	Temporal_Mid R (SD)	4.05^{a} (0.44)	$3.89^{a,b}$ (0.30)	3.77^{b} (0.36)	3.73^{b} (0.56)	8.0*
	Temporal_Inf L (SD)	4.93^{a} (0.51)	$4.65^{a,b}$ (0.48)	4.67^{b} (0.40)	4.46^{b} (0.72)	9.4*
	Temporal_Inf R (SD)	5.01 (0.59)	4.85 (0.33)	4.81 (0.43)	4.69 (0.70)	4.0
	Ventricl L (SD)	10.9 (2.83)	12.4 (3.1)	13.21 (3.0)	13.8 (3.1)	13.7*
	Ventricl R (SD)	9.0 (2.5)	10.23 (3.2)	11.0 (3.0)	11.6 (2.6)	12.7*

NCI= No Cognitive Impairment; naMCI=Non-Amnestic MCI, aMCI=Amnestic MCI
Note: Volumes and SD are expressed as 1/000 of intracranial volume.
*p<.001; Means with different alphabetic superscripts are statistically significant at p<.05 by the Scheffe' procedure.

Table 5.4 Normalized volumes by diagnostic groups using Template S Set.

	Brain Regions	NCI (N=103)	naMCI (N=24)	aMCI (N=68)	AD (N=46)	F-Value (df=3,237)
Template S Set	GM (SD)	445.4^{a} (38.1)	$423.8^{a,b}$ (51.6)	419.4^{b} (37.6)	421.9^{b} (61.4)	5.9*
	WM (SD)	300.9 (24.0)	298.4 (26.4)	299.5 (23.5)	282.9 (59.4)	3.3
	CSF (SD)	253.7^{a} (41.2)	$277.7^{a,b}$ (47.2)	281.1^{b} (38.6)	295.1^{b} (41.1)	12.9*
	Hippocampus L (SD)	2.58^{a} (0.24)	2.38^{b} (0.30)	2.26^{b} (0.27)	1.97^{c} (0.41)	48.5*
	Hippocampus R (SD)	2.46^{a} (0.28)	$2.28^{a,b}$ (0.28)	2.13^{b} (0.34)	1.90^{c} (0.44)	33.5*
	Amygdala L (SD)	0.78^{a} (0.07)	$0.76^{a,b}$ (0.10)	0.74^{b} (0.07)	0.69^{c} (0.09)	18.1*

	Amygdala R (SD)	0.81^{a} (0.07)	$0.77^{a,b,c}$ (0.09)	$0.76^{b,c}$ (0.07)	$0.72^{b,c}$ (0.10)	16.8*
	Insula L (SD)	5.02^{a} (0.50)	4.59^{b} (0.54)	4.61^{b} (0.48)	4.51^{b} (0.72)	13.6*
	Insula R (SD)	4.80^{a} (0.44)	4.39^{b} (0.50)	4.40^{b} (0.47)	4.36^{b} (0.60)	14.4*
	ParaHippocampal L (SD)	2.40 (0.30)	2.31 (0.33)	2.33 (0.32)	2.20 (0.35)	4.2
	ParaHippocampal R (SD)	2.85 (0.30)	2.71 (0.29)	2.76 (0.34)	2.67 (0.37)	3.6
	Fusiform L (SD)	5.96^{a} (0.54)	$5.64^{a,b}$ (0.61)	5.73^{b} (0.51)	5.75^{b} (0.81)	6.1*
	Fusiform R (SD)	6.12^{a} (0.58)	$5.75^{a,b}$ (0.59)	$5.86^{a,b}$ (0.53)	5.75^{b} (0.81)	5.5
	Precuneus L (SD)	7.11^{a} (0.74)	$6.81^{a,b}$ (1.07)	6.71^{b} (0.83)	6.62^{b} (1.00)	5.0
	Precuneus R (SD)	6.39^{a} (0.73)	$6.12^{a,b}$ (0.84)	5.81^{b} (0.71)	$6.01^{a,b}$ (1.18)	7.0*
	Putamen L (SD)	2.50 (0.44)	2.35 (0.56)	2.34 (0.48)	2.42 (0.95)	1.1
	Putamen R (SD)	2.57 (0.42)	2.39 (0.51)	2.43 (0.49)	2.54 (0.94)	1.2
	Thalamus L (SD)	2.43^{a} (0.36)	2.18^{b} (0.35)	2.15^{b} (0.32)	2.10^{b} (0.53)	11.5*
	Thalamus R (SD)	2.30^{a} (0.38)	2.05^{b} (0.36)	1.98^{b} (0.29)	1.92^{b} (0.51)	15.2*
	Temporal_Sup L (SD)	5.13^{a} (0.56)	4.70^{b} (0.63)	4.68^{b} (0.55)	4.62^{b} (0.86)	10.9*
	Temporal_Sup R (SD)	6.62^{a} (0.77)	6.00^{b} (0.98)	5.94^{b} (0.75)	5.96^{b} (1.05)	12.0*
	Temporal_Pole_Sup L (SD)	3.12^{a} (0.43)	3.05^{a} (0.42)	2.77^{b} (0.53)	2.39^{c} (0.66)	24.0*
	Temporal_Pole_Sup R (SD)	3.01^{a} (0.39)	2.95^{b} (0.44)	$2.69^{a,b}$ (0.53)	2.40^{c} (0.57)	20.0*
	Temporal_Mid L (SD)	11.62^{a} (1.05)	10.74^{b} (1.13)	10.85^{b} (1.02)	10.84^{b} (1.89)	7.9*
	Temporal_Mid R (SD)	10.09 (0.85)	9.53 (0.88)	9.49 (0.93)	9.73 (1.66)	5.0
	Temporal_Inf L (SD)	8.63^{a} (0.65)	$8.21^{a,b}$ (0.80)	8.25^{b} (0.64)	8.04^{b} (1.02)	8.2*
	Temporal_Inf R (SD)	9.34 (0.66)	8.96 (0.68)	8.98 (0.74)	8.96 (1.14)	4.4

NCI= No Cognitive Impairment; naMCI=Non-Amnestic MCI, aMCI=Amnestic MCI
Note: Volumes and SD are expressed as 1/000 of intracranial volume.
*p<.001; Means with different alphabetic superscripts are statistically significant at p<.05 by the Scheffe' procedure.

Table 5.5 Normalized volumes by diagnostic groups using MNI Template Set.

	Brain Regions	NCI (N=103)	naMCI (N=24)	aMCI (N=68)	AD (N=46)	F-Value (df=3,237)
MNI Template Set	GM (SD)	429.5 (40.7)	409.0 (45.4)	409.8 (51.1)	404.6 (43.8)	4.7
	WM (SD)	304.5 (23.9)	308.0 (25.3)	306.1 (26.3)	300.4 (42.1)	0.5
	CSF (SD)	266.0^{a} (40.9)	283.0^{a,b} (36.9)	284.1^{a,b} (48.2)	295.0^{b} (40.6)	5.7*
	Hippocampus L (SD)	2.00^{a} (0.26)	1.86^{a,b} (0.31)	1.75^{b} (0.26)	1.52^{c} (0.33)	32.5*
	Hippocampus R (SD)	1.83^{a} (0.28)	1.66^{a,b} (0.31)	1.58^{b} (0.32)	1.43^{b,c} (0.39)	19.7*
	Amygdala L (SD)	0.65^{a} (0.06)	0.62^{a,b} (0.06)	0.61^{b} (0.08)	0.57^{c} (0.10)	13.9*
	Amygdala R (SD)	0.76 (0.06)	0.72 (0.06)	0.73 (0.07)	0.73 (0.10)	3.4
	Insula L (SD)	4.40^{a} (0.43)	4.17^{a,b} (0.42)	4.09^{b} (0.41)	3.96^{b} (0.61)	11.7*
	Insula R (SD)	4.27^{a} (0.38)	3.93^{b} (0.46)	3.90^{b} (0.48)	3.83^{b} (0.56)	14.7*
	ParaHippocampal L (SD)	2.25^{a} (0.20)	2.18^{a,b} (0.22)	2.21^{a} (0.28)	2.04^{b} (0.30)	7.8*
	ParaHippocampal R (SD)	2.88^{a} (0.22)	2.81^{a,b} (0.23)	2.79^{a,b} (0.27)	2.66^{b} (0.34)	7.5*
	Fusiform L (SD)	5.48^{a} (0.54)	5.20^{a,b} (0.55)	5.19^{b} (0.42)	5.03^{b} (0.61)	9.0*
	Fusiform R (SD)	5.74^{a} (0.59)	5.41^{a,b} (0.60)	5.42^{b} (0.54)	5.36^{b} (0.78)	6.0*
	Precuneus L (SD)	6.01 (0.82)	5.88 (1.10)	5.84 (1.05)	5.78 (1.01)	0.8
	Precuneus R (SD)	5.59 (0.64)	5.44 (0.74)	5.18 (0.71)	5.29 (0.86)	5.0
	Putamen L (SD)	2.09 (0.38)	2.04 (0.55)	1.99 (0.43)	1.97 (0.55)	1.1
	Putamen R (SD)	2.19 (0.35)	2.07 (0.42)	2.08 (0.42)	2.07 (0.61)	1.5
	Thalamus L (SD)	2.24^{a} (0.35)	1.99^{b} (0.35)	1.95^{b} (0.35)	1.79^{b} (0.38)	20.1*
	Thalamus R (SD)	2.32^{a} (0.34)	2.09^{b} (0.31)	2.02^{b} (0.30)	1.86^{b} (0.38)	23.5*
	Temporal_Sup L (SD)	4.90^{a} (0.59)	4.32^{b} (0.53)	4.38^{b} (0.71)	4.21^{b} (0.55)	18.6*

	Temporal_Sup R (SD)	5.77^{a} (0.75)	5.20^{b} (0.88)	5.33^{b} (1.10)	5.21^{b} (0.83)	6.5*
	Temporal_Pole_Sup L (SD)	2.25^{a} (0.38)	$2.06^{a,b}$ (0.41)	2.03^{b} (0.47)	1.89^{b} (0.53)	8.1*
	Temporal_Pole_Sup R (SD)	2.21^{a} (0.34)	$2.07^{a,b}$ (0.37)	1.95^{b} (0.52)	1.84^{b} (0.56)	8.8*
	Temporal_Mid L (SD)	10.71^{a} (1.01)	$10.01^{a,b}$ (1.11)	10.14^{b} (1.20)	9.90^{b} (1.45)	6.9*
	Temporal_Mid R (SD)	9.97^{a} (1.03)	$9.33^{a.b}$ (1.15)	9.17^{b} (1.39)	9.01^{b} (1.27)	9.7*
	Temporal_Inf L (SD)	7.44 (0.68)	7.18 (0.71)	7.19 (0.55)	7.15 (0.93)	2.8
	Temporal_Inf R (SD)	8.70 (0.70)	8.28 (0.78)	8.38 (0.77)	8.36 (1.06)	3.7

NCI= No Cognitive Impairment; naMCI=Non-Amnestic MCI, aMCI=Amnestic MCI
Note: Volumes and SD are expressed as 1/000 of intracranial volume.
*p<.001; Means with different alphabetic superscripts are statistically significant at p<.05 by the Scheffe' procedure.

5.4.2 Correlation with Clinical Evaluations: MMSE and CDR-sb

Three Tissues and 24 or 26 ROI

Within all diagnostic groups, bivariate correlation (Pearson's r) coefficients were used to examine the relationship between normalized three tissues and 24 or 26 ROIs volumes and the measures of clinical status: neuropsychological test MMSE scores and the Clinical Dementia Rating scale (CDR-sb). The results of these analyses are shown in Figure 5.2 and Figure 5.3. As shown in Figure 5.2, the correlations of MMSE scores, a measure of global cognitive function, with volumetric measures (except left parahippocampal volume), were significantly greater for Template E than for the corresponding volumes measures by the MNI Template or the Template S (p<.05). Taken together, volumetric measures using the Template E set were more highly correlated with cognitive test scores and severity of clinical symptoms than the volumetric measures using the MNI Template or the Template S. As for the correlations of Clinical Dementia Rating scale (CDR-sb), similar results were obtained and are shown in Figure 5.3.

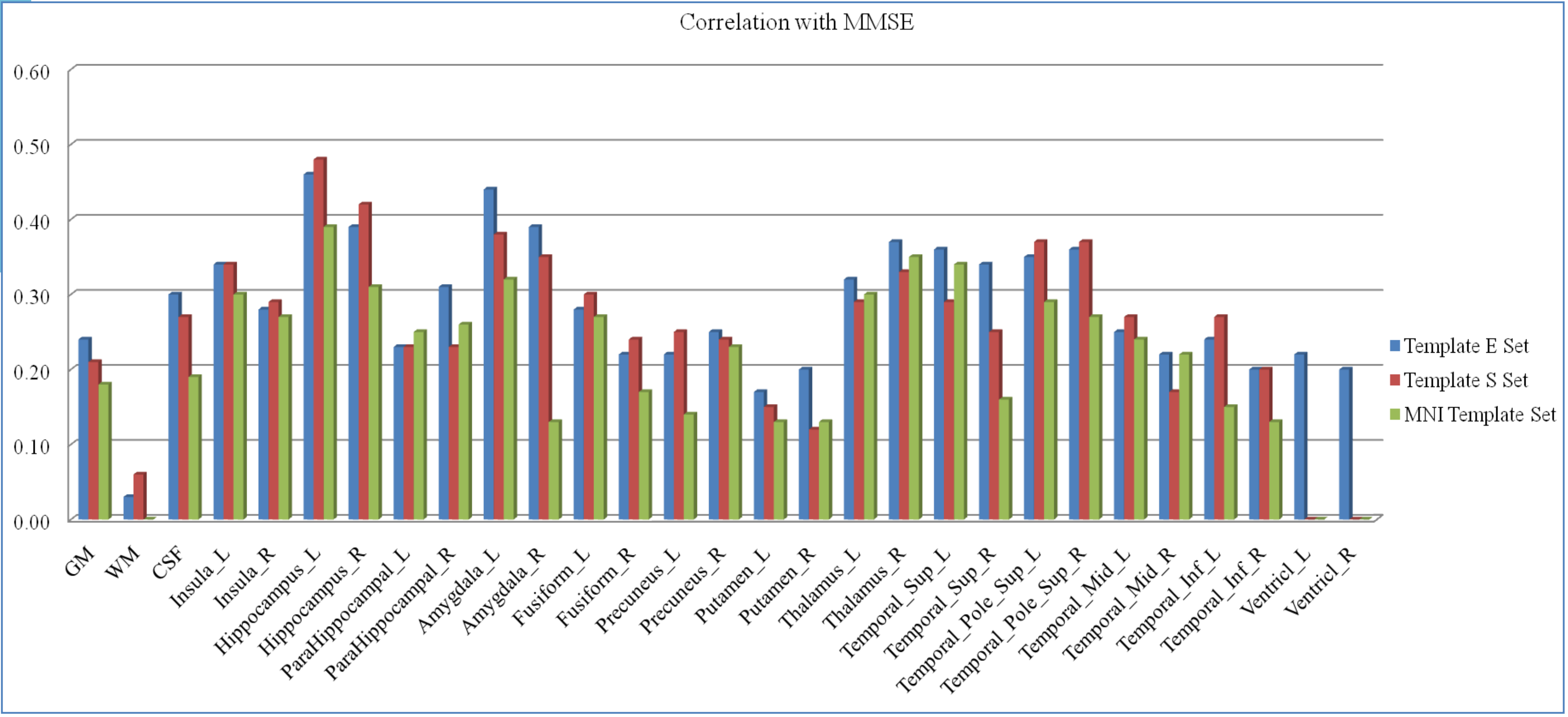

Figure 5.2 The correlations of the Mini Mental State Examination (MMSE) scores with volumetric measures of three tissues and 26 regions using three template sets.

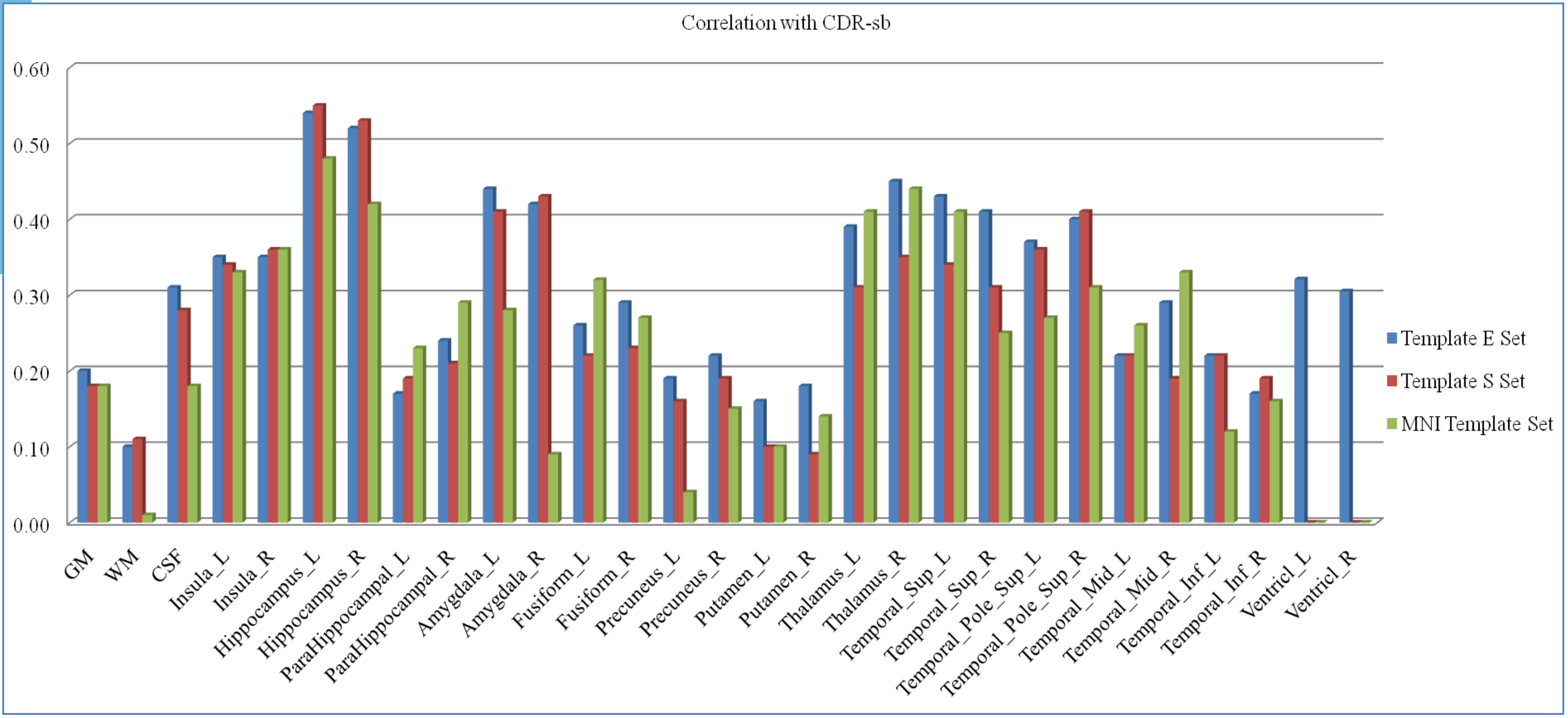

Figure 5.3 The correlations of the Clinical Dementia Rating – “sum of boxes” (CDR-sb) scales with volumetric measures of three tissues and 26 regions using three template sets.

Hippocampal and Amygdaloid Complex

Atrophy of medial temporal structures, such as hippocampus and amygdala, is one of the best-established signs of AD (Duyckaerts *et al.*, 2008; Hamalainen *et al.*, 2007, Chupin *et al.*, 2007). Post-mortem studies report early neuropathological lesions and neuronal loss in hippocampus and amygdala (Duyckaerts *et al.*, 2008). Studies have shown that the combined MRI based volumetric measurement of hippocampus and amygdala improved the accuracy in distinguishing diagnosis groups (Pantel *et al.*, 1997; Hampel *et al.*, 2002). Here, we examined the relationship between normalized hippocampal and amygdaloid complex with the clinical measures MMSE and CDR-sb by bivariate correlation analysis (Pearson's r). The results are shown in Figure 5.4 and Figure 5.5.

Left and right hippocampal and amygdaloid complex volumes based on template S set showed higher correlations with MMSE score (Figure 5.4) (left: R=0.488, F=74.7; right: R=0.425, F=52.8) than these volumes based on the MNI Template (left: R=0.419, F=48.3; right: R=0.307, F=24.9). Volumes based on the Template S set were similar to those of Template E set (left: R=0.487, F=74.4; right: R=0.405, F=46.9).

As for the correlations with CDR-sb scales, left and right hippocampal and amygdaloid complex volumes based on template S set also showed higher negative correlations (Figure 5.5) (left: R=0.559; F=108.4; right: R=0.538; F=97.3) compared to volumes based on the MNI Template (left: R=0.484; F=73.2; right: R=0.407; F=47.6). Volumes based on the Template S set were similar to those of Template E set (left: R=0.558; F=108.3; right: R=0.528; F =92.4).

	Left	Right
Template E Set	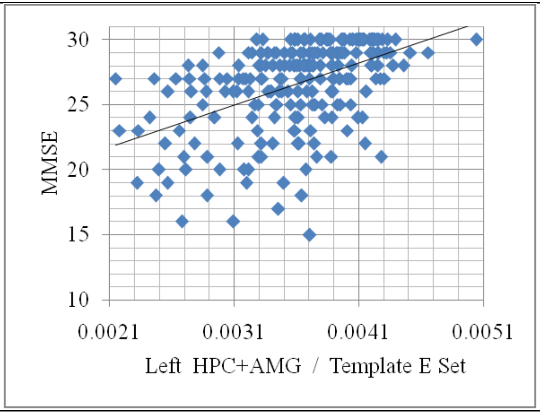	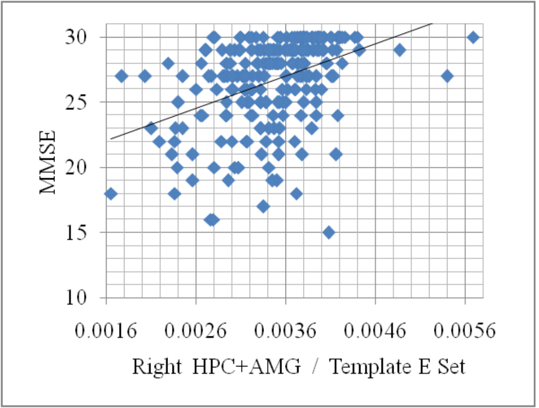
	R=.488; F=74.7*	R=.425; F=52.8
Template S Set	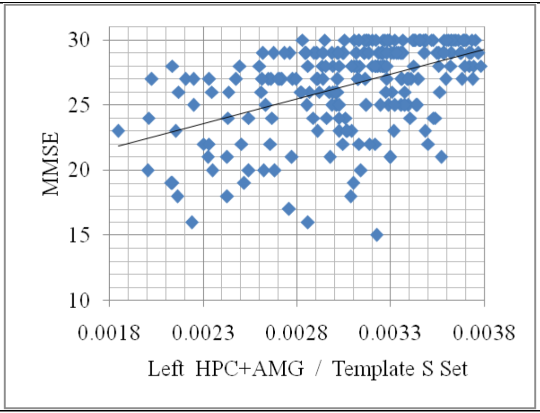	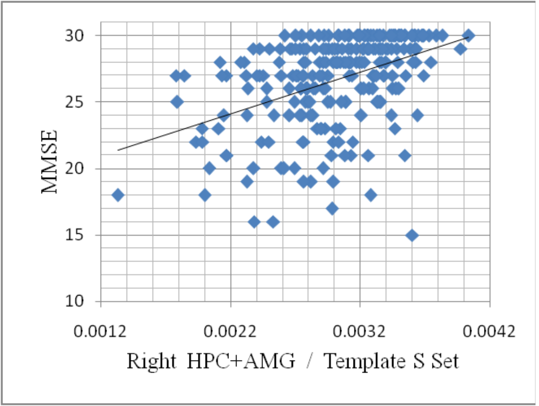
	R=.487; F=74.4	R=.405; F=46.9*
MNI Template Set	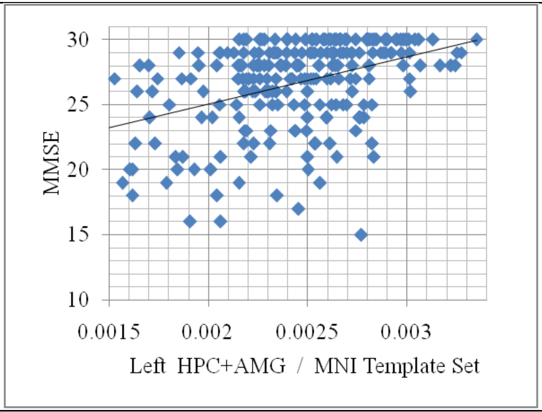	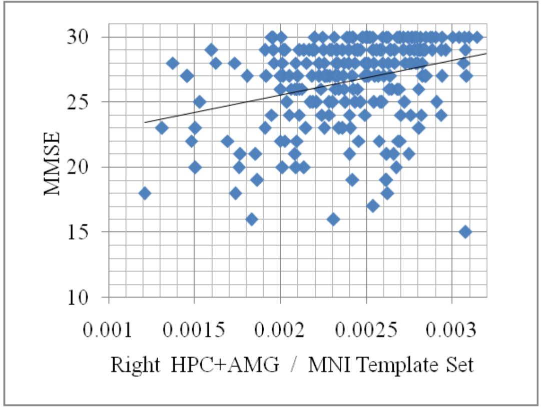
	R=.410; F=48.3	R=.307; F=24.9

Figure 5.4 Correlation between hippocampal and amygdaloid complex volume and MMSE scores within all diagnosis groups. The regression lines are indicated. HPC = Hippocampus; AMG= Amygdala.

	Left	Right
Template E Set	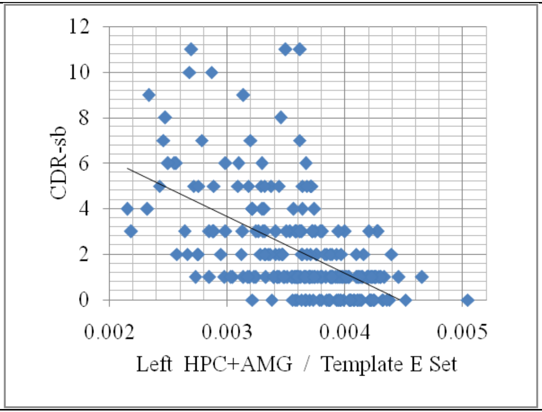	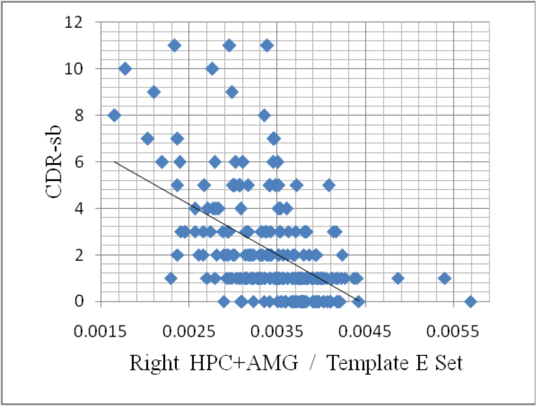
	R=.559; F=108.4	R=.538; F=97.3
Template S Set	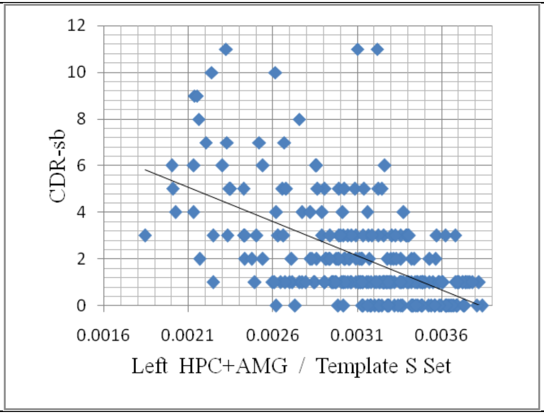	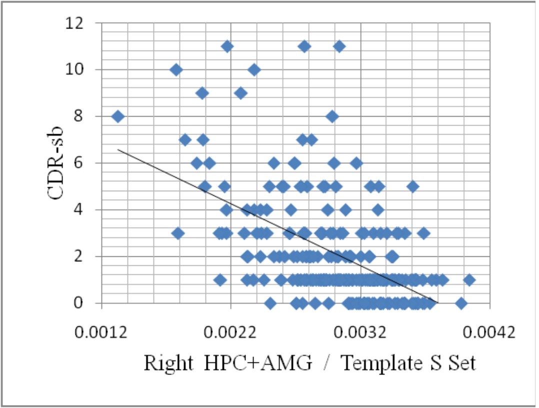
	R=.558; F=108.3	R=528; F =92.4
MNI Template Set	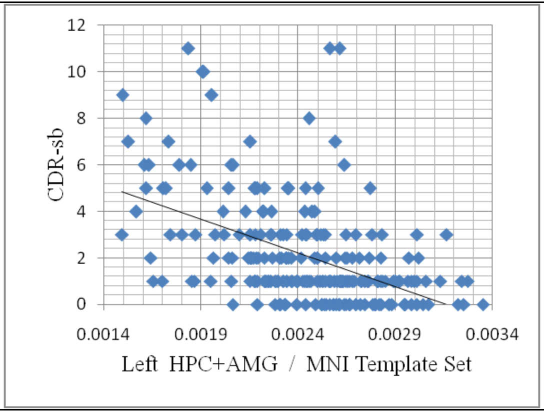	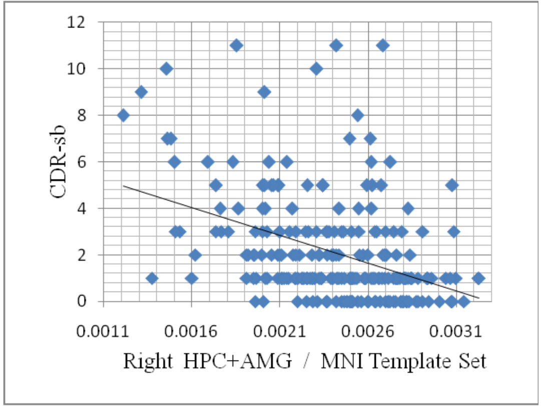
	R=.484; F=73.2	R=.407; F=47.6

Figure 5.5 Correlation between hippocampal and amygdaloid complex volume and CDR-sb scales within all diagnosis groups. The regression lines are indicated. HPC = Hippocampus; AMG= Amygdala.

5.4.3 Ability to Distinguish Diagnostic Groups

The accuracy of discrimination among diagnostic groups with ROI volumetric measures using three template sets was assessed in the total group by computing areas under the curve (AUC) of receiver-operating characteristics (ROC). The ROC curve is a frequently used measure of the effectiveness of diagnostic tests in discriminating between groups of individuals.

In discriminating between AD patients and “No Cognitive Impairment” (see Figure 5.6), the highest area under the curve of the ROC was 0.90 for left hippocampus using template E set. The second highest AUC was 0.89 for left amygdale using template E set. With few exceptions (right insula, left parahippocampal, left thalamus and middle temporal), volumetric analysis using template E shown higher AUC compared with template E or MNI template S.

In discriminating between aMCI and “No Cognitive Impairment” (see Figure 5.7), the highest area under the curve of the ROC was 0.82 for left hippocampus using template E set. With few exceptions (fusiform, right superior temporal pole, right middle temporal, right inferior temporal), volumetric analysis using template E shown higher AUC compared with template E or MNI template S.

These analyses showed that the new template E set was superior to the MNI template set in general.

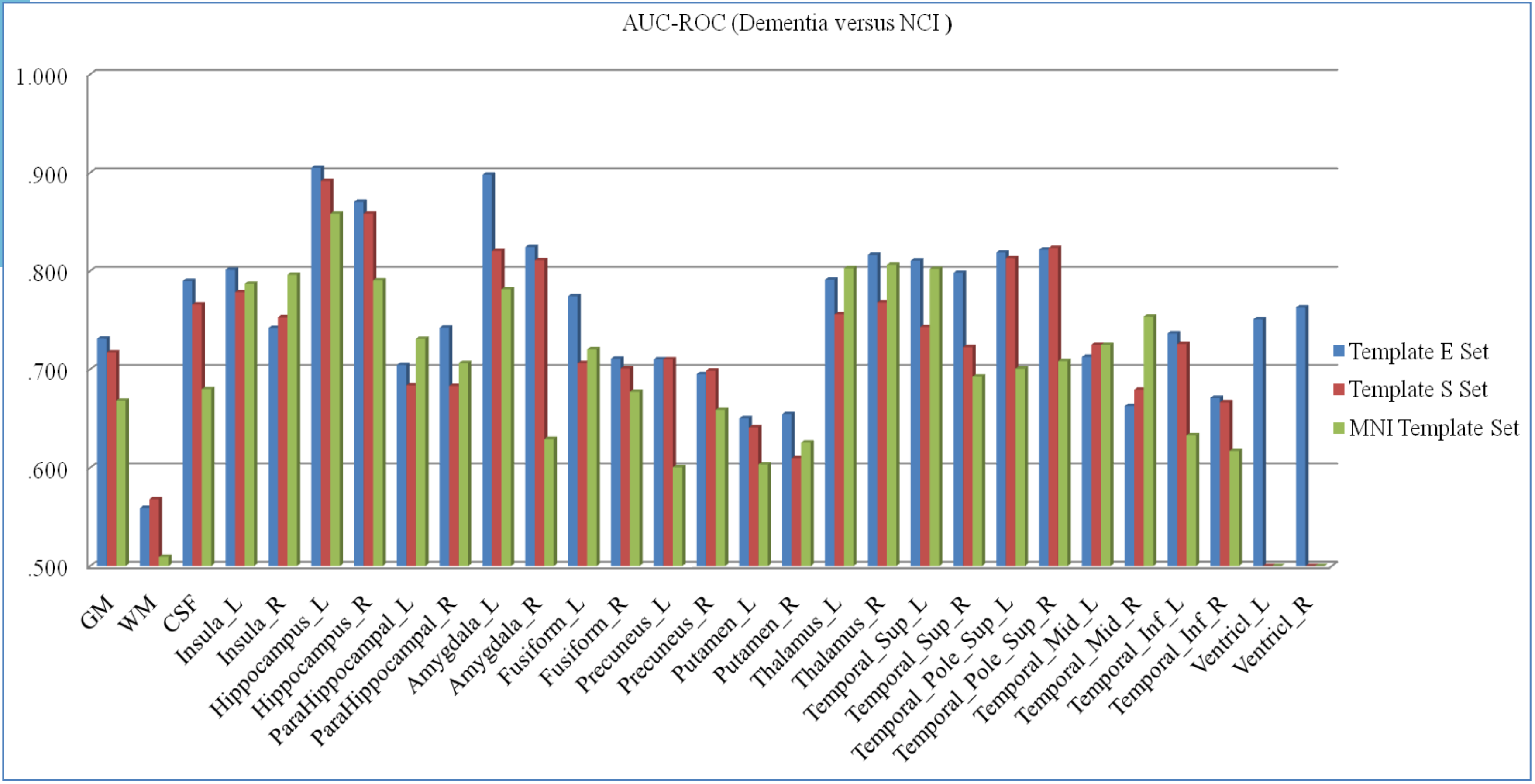

Figure 5.6 Area Under the Curve for the ROC for three tissues and 26 regions volumetric measures, for AD versus NCI.

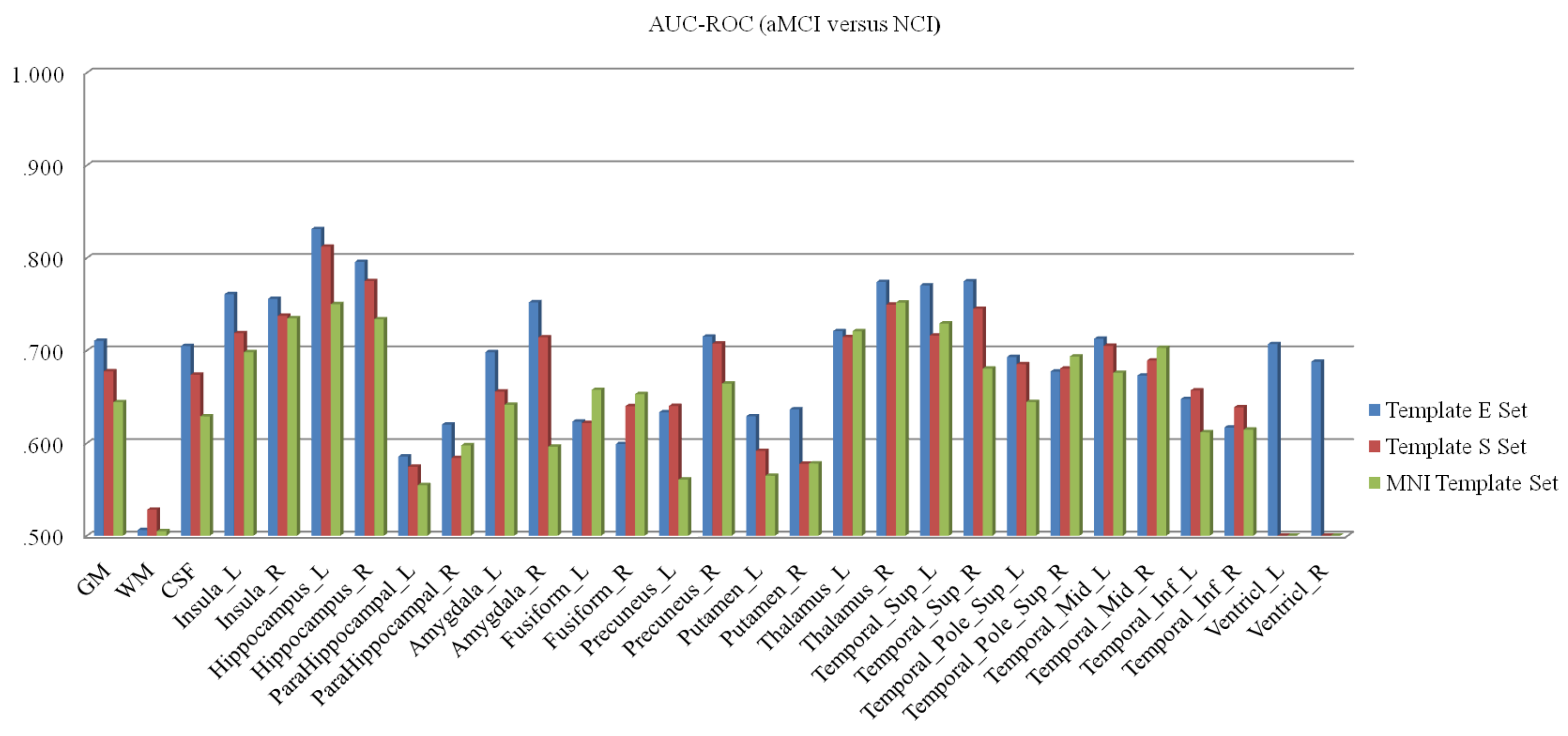

Figure 5.7 Area Under the Curve for the ROC for three tissues and 25 regions volumetric measures, for aMCI versus NCI.

5.5 Experiment 3: Cross-sectional Studies on 241 Subjects – Volumetric, Automated Area and VRS

5.5.1 Comparisons of Means by Diagnostic Groups Using RHPA, VRS of HPC and HPC Volumes

We applied this automated area measurement method to the 241 subjects. The results (RHPA) were compared with VRS hippocampal scores (VRS_HPC) and normalized hippocampal volumes (HPC_Vol) using template set E. Group comparisons of means were analyzed using one-way ANOVA. Statistical results (mean±SD) of RHPA, VRS_HPC scores and HPC_Vol are shown in Table 5.6.

RHPA measures for the "No Cognitive Impairment" group have the largest mean, while the AD group has the smallest mean ratio on both sides. VRS_HPC mean scores for "No Cognitive Impairment" are the highest and for the AD group are lowest on both sides. HPC_Vol measures on both sides show a larger difference of the means between diagnostic groups, and has the highest F values for both sides compared with RHPA or VRS_HPC.

All three measurements show the effect of AD on the degree of atrophy on MRI. Post-hoc tests of means by Scheffe' analyzed the effect of diagnostic group on all these measurements (see superscripts in Table 5.6).

Table 5.6 Values (mean±SD) of RHPA, VRS_HPC and HPC_Vol in all diagnostic groups

Diagnostic Group	NCI (N=103)	naMCI (N=24)	aMCI (N=68)	AD (N=46)	F-Value (df=3,237)
RHPA L (SD)	0.83^{a} (0.09)	$0.79^{a,b}$ (0.08)	0.73^{b} (0.13)	0.65^{c} (0.17)	24.6*
RHPA R (SD)	0.87^{a} 0.10	$0.84^{a,b}$ (0.11)	$0.75^{b,c}$ (0.17)	0.68^{c} (0.19)	20.8*
VRS_HPC L (SD)	0.55^{a} (0.654)	0.75^{a} (0.608)	1.41^{b} (1.011)	2.30^{c} (1.209)	45.1*
VRS_HPC R (SD)	0.59^{a} (0.694)	$0.96^{a,c}$ (0.859)	$1.60^{b,c}$ (1.161)	2.07^{b} (1.200)	30.3*
HPC_Vol L (SD)	2.99^{a} (0.29)	2.73^{b} (0.33)	2.59^{b} (0.33)	2.26^{c} (0.46)	52.5*
HPC_Vol R (SD)	2.80^{a} (0.38)	2.51^{b} (0.30)	2.38^{b} (0.37)	2.12^{c} (0.49)	35.5*

NCI= No Cognitive Impairment; naMCI=Non-Amnestic MCI, aMCI=Amnestic MCI
RHPA: automated area measurements; VRS_HPC: VRS hippocampus scores on coronal MB slice; HPC_Vol: normalized hippocampus volumes. Volumes and SD are expressed as 1/000 of intracranial volume.
*p<.001; Means with different alphabetic superscripts are statistically significant at p<.05 by the Scheffe' procedure.

5.5.2 Correlation with Clinical Evaluations: MMSE and CDR-sb

Within all diagnostic groups, the relationship between RHPA values, VRS_HPC scores and normalized hippocampus volumes, and the relationships between these three measures with MMSE or CDR-sb were examined by bivariate correlational analysis (Pearson's r). The results of that analysis are displayed in Table 5.7 and Table 5.8.

Table 5.7 shows that these three approaches for assessing hippocampal atrophy are strongly correlated. With respect to the left hippocampus, the correlation coefficient is -0.671 (p<0.001) between RHPA values and VRS_HPC; 0.716 (p<0.001) between RHPA values and HPC_Vol; -0.689 (p<0.001) between VRS_HPC and HPC_Vol. For right hippocampus, the correlation coefficient is -0.801 (p<0.001), 0.492 (p<0.001). and -0.685 (p<0.001) respectively (Table 5.7).

Table 5.7 Correlations between RHPA, VRS_HPC and HPC_Vol within all diagnostic groups.

Correlation Coef.	RHPA L	RHPA R	VRS_HPC L	VRS_HPC R	HPC_Vol L	HPC_Vol R
RHPA L	1	.513*	-.671*	-.583*	.498*	.492*
RHPA R	.513*	1	-.622*	-.801*	.664*	.716*
VRS_HPC L	-.671*	-.622*	1	.728*	-.689*	-.603*
VRS_HPC R	-.583*	-.801*	.728*	1	-.626*	-.685*
HPC_Vol L	.716*	.664*	-.689*	-.626*	1	.852*
HPC_Vol R	.498*	.492*	-.603*	-.685*	.852*	1

RHPA: automated area measurements; VRS_HPC: VRS hippocampus scores on coronal MB slice; HPC_Vol: normalized hippocampus volumes.
*. Correlation is significant at the 0.001 level (1-tailed).

The correlations of atrophy measures from these three methods with a cognitive test (MMSE) and the clinical dementia rating score (CDR-sb) scores, are showing in Table 5.8. Compared with automatic area measures and hippocampus volumes, VRS_HPC scores show higher correlations (left is 0.506 (p<0.001), right is 0.456 (p<0.001)) with MMSE and higher correlations (left is 0.582 (p<0.001), right is 0.527 (p<0.001)) with CDR-sb.

5.5.3 Ability to Distinguish Diagnostic Groups

The ability of RHPA, VRS_HPC and HPC_Vol to distinguish the diagnostic groups NCI, naMCI, aMCI and AD were compared using area under the curve (AUC) for the receiver operating characteristics (ROC) (Table 5.9).

Table 5.8 Correlations between RHPA, VRS_HPC or HPC_Vol with MMSE and CDR-sb within all diagnostic

Correlation Coef.	MMSE	CDR-sb
RHPA L	.381*	-.372*
RHPA R	.340*	-.450*
VRS_HPC L	-.506*	.582*
VRS_HPC R	-.456*	.527*
HPC_Vol L	.461*	-.540*
HPC_Vol R	.385*	-.520*

RHPA: automated area measurements; VRS_HPC: VRS hippocampus scores on coronal MB slice; HPC_Vol: normalized hippocampus volumes.
*. Correlation is significant at the 0.001 level (1-tailed).

Table 5.9 Ability of RHPA, VRS_HPC and HPC_Vol in distinguishing diagnostic groups. Areas under curve for receiver operator characteristics (AUC-ROC)

AUC-ROC	AD versus NCI	aMCI versus NCI
RHPA L	.828	.728
RHPA R	.816	.719
VRS_HPC L	.875	.757
VRS_HPC R	.846	.757
HPC_Vol L	.905	.831
HPC_Vol R	.870	.796

NCI= No Cognitive Impairment; aMCI=Amnestic MCI
RHPA: automated area measurements; VRS_HPC: VRS hippocampus scores on coronal MB slice; HPC_Vol: normalized hippocampus volumes.

Table 5.9 shows a comparison of these three approaches for assessing hippocampal atrophy in distinguishing diagnostic groups. The results show that hippocampal volumes are the most robust for distinguishing aMCI from Mild AD, and aMCI from NCI.

Overall, the automatic area measure RHPA is inferior to hippocampus volumetric measures or VRS hippocampus scores from the coronal MB slice.

5.6 Experiment 4: Comparison with NeuroQuant^{TM}

The NeuroQuant^{TM} is a commercial software package (CorTechs Labs Inc, La Jolla, CA), which provides a full volume segmentation of 10 subcortical brain regions in each hemisphere, including hippocampus, amygdale, putamen, thalamus, pallidum, caudate, cerebellum, and brain stem. It has been validated against manual segmentation methods and on the basis of those studies received Food and Drug Administration 510K approval for clinical use in measuring volumes of brain structures in MR images (Kovacevic *et al.*, 2009; Brewer *et al.*, 2009). The automated segmentation of structures algorithm is similar to FreeSurfer (Fischl *et al.*, 2002), which is based on surface deformations and employs Markov random fields to approximate the posterior distribution for anatomic labelings at each voxel in the brain. It utilizes a predefined probabilistic brain atlas which was designed to better represent the aged population (Kovacevic *et al.*, 2009; Brewer *et al.*, 2009).

The results of automated atlas-based segmentation using three template sets are compared with NeuroQuant^{TM} on 72 clinical MRI scans of subjects with NCI, aMCI and AD.

The statistical comparisons of mean, correlations with clinical evaluations CDR-sb or MMSE and the ability to distinguish diagnostic group are shown in Table 5.10, Figure 5.8 and Figure 5.9.

Table 5.10 Normalized volumes by diagnostic groups.

	Brain Region	NCI (N=21)	aMCI (N=26)	AD (N=25)	F-Value (df=2,69)
NeuroQuant TM	Hippocampus L (SD)	2.39^a (0.26)	2.14^b (0.24)	1.87^c (0.34)	19.2*
	Hippocampus R (SD)	2.54^a (0.36)	2.16^b (0.31)	1.91^b (0.46)	15.1*
	Amygdala L (SD)	1.08^a (0.10)	0.91^b (0.15)	0.77^c (0.17)	23.2*
	Amygdala R (SD)	1.09^a (0.19)	0.87^b (0.18)	0.84^b (0.22)	11.0*
	Putamen_L (SD)	3.11 (0.30))	2.82 (0.39)	2.75 (0.59)	3.8
	Putamen_R (SD)	2.89 (0.31)	2.67 (0.34)	2.56 (0.58)	3.4
	Thalamus_L (SD)	5.19 (0.79)	5.19 (0.42)	5.16 (0.67)	0.1
	Thalamus_R (SD)	5.35 (0.76)	5.26 (0.43)	5.20 (0.81)	0.3
Template set E	Hippocampus L (SD)	3.00^a (0.30)	2.54^b (0.34)	2.25^c (0.42)	21.7*
	Hippocampus R (SD)	2.78^a (0.40)	2.28^b (0.41)	2.11^b (0.51)	13.2*
	Amygdala L (SD)	0.95^a (0.06)	0.89^b (0.06)	0.83^c (0.11)	12.1*
	Amygdala R (SD)	0.95^a (0.09)	0.88^b (0.09)	0.87^b (0.11)	4.5
	Putamen_L (SD)	2.47 (0.27)	2.32 (0.33)	2.31 (0.67)	0.8
	Putamen_R (SD)	2.13 (0.23)	2.04 (0.31)	2.03 (0.58)	0.4
	Thalamus_L (SD)	2.40^a (0.37)	2.21^a (0.26)	2.20^b (0.35)	8.0*
	Thalamus_R (SD)	2.27^a (0.39)	2.02^b (0.24)	1.76^c (0.35)	13.9*

NCI= No Cognitive Impairment; aMCI=Amnestic MCI. * $p<0.001$
Note: Volumes and SD are expressed as 1/000 of intracranial volume.
Means with different alphabetic superscripts are significantly different from each other at $p<0.05$ by the Scheffe' procedure.

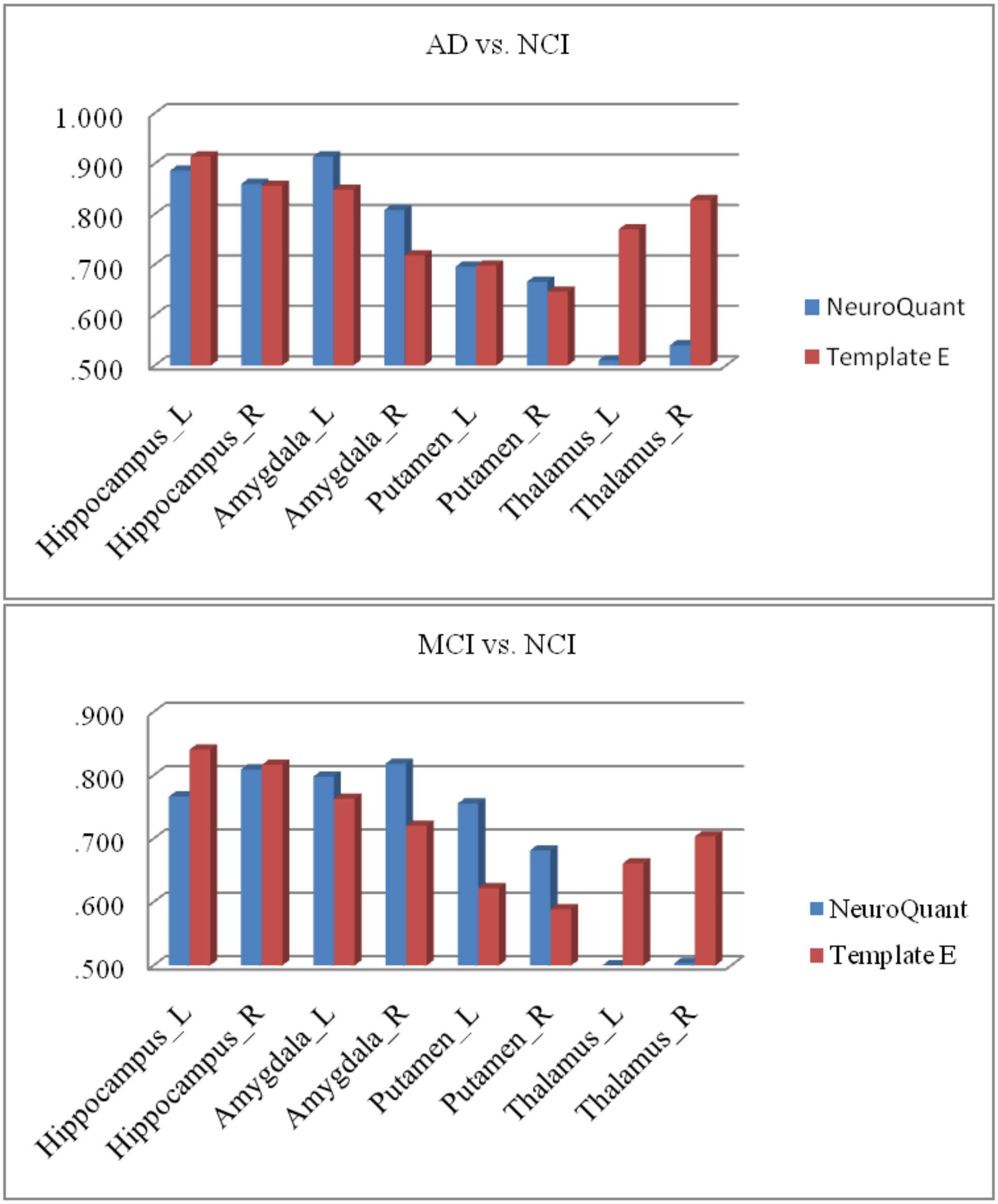

Figure 5.8 (Top) AUC-ROC for AD versus NCI. AUC-ROC for hippocampus and putamen are similar using NeuroQuant^{TM} or template E set volumetric analysis. However, template E set performs better than NeuroQuant^{TM} for the right (R) and left (L) thalamus. (Bottom) AUC-ROC for MCI versus NCI. The AUC-ROC for right amygdale, left and right putamen are higher for NeuroQuant^{TM} than using template E set volumetric analysis, but the opposite is true for the thalamus. AUC-ROC: Area Under the Curve for the receiver operator characteristics.

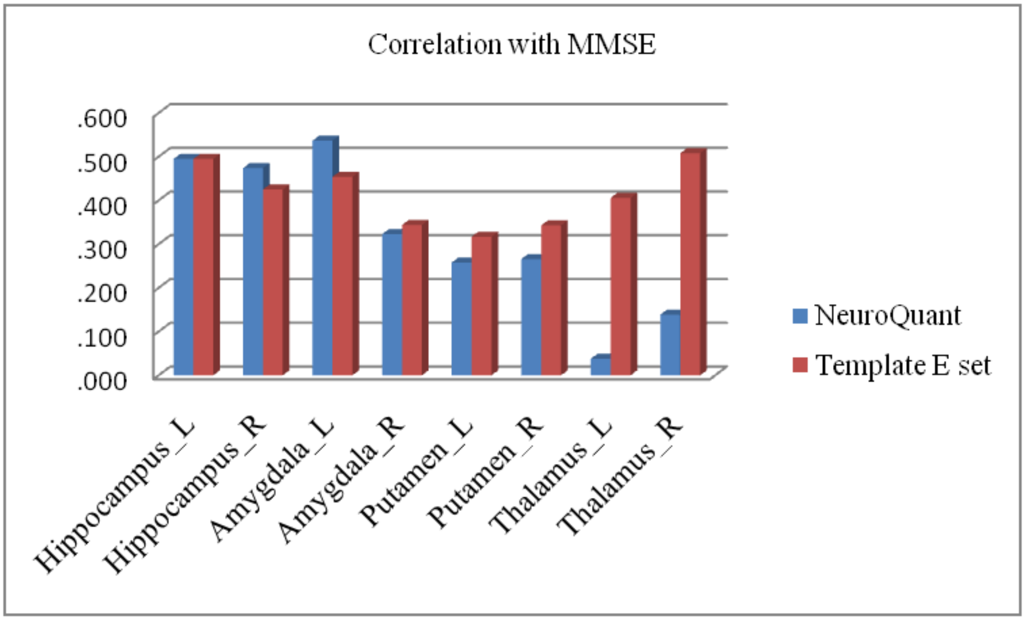

Figure 5.9 The correlations of the Mini Mental State Examination (MMSE) scores with volumetric measures using three template sets.

Chapter 6 Discussion and Conclusion

The initial results from the study that compared the VRS-MTA method with the volumetric analysis using IBASPM with the MNI template (Shen *et al.*, 2011b) show clearly that the conventionally used standard template lacks accuracy in anatomical segmentation. As a result, the MNI template has reduced sensitivity and specificity for distinguishing AD and normal control subjects. This stimulated the motivation of this study to improve templates so as to allow continued use of atlas based methods with IBASPM for volumetric analysis and to achieve higher accuracy in segmentation. The value of IBASPM for volumetric analysis, which is an atlas-based approach, as opposed to other voxel-by-voxel approaches, such as Freesurfer, lies on the fact that it is operationally much less demanding in terms of computational effort and, as a result, allows the processing of images in a fraction of the time required by the Freesurfer software.

6.1 Discussion

This study demonstrates that replacing the MNI Template Set, which consists of a brain atlas definition AAL (Tzourio-Mazoyer *et al.*, 2002) and a coordinate template (the MNI Template), by the Template S Set, which consists of the same atlas definition AAL (Tzourio-Mazoyer *et al.*, 2002) and a new coordinate template derived from single-subject image, has improved the accuracy of anatomical segmentation of the ROIs, such as HPC and AMG (Shen *et al.*, 2011b). The improved segmentation is evaluated by the measures of correspondence between the manual and the automated segmentations (by using both templates) of the structures most affected by Alzheimer's disease. A further improvement in accuracy of segmentation can be seen when the Template S Set is replaced by the Template E Set, which consists of a custom-defined atlas, drawn on an elderly subject's brain which has been transformed to MNI space, and a coordinate template which has also been derived from the same image, and custom tissue class priors which has been created from the study population. The improved accuracy of segmentation when using these novel templates is reflected by the ability to better discriminate subjects with NCI from those with aMCI subjects and probable AD. Furthermore, the correlations of ROIs volumes to the MMSE and CDR-sb scores across subject groups are improved when replacing the MNI Template Set by the Template S set, and even more by the Template E Set.

The comparison between the commercial software NeuroQuant^{TM} and the atlas-based segmentation by using the Template E Set has shown that both methods performed equivalently in most brain regions. However, NeuroQuant^{TM} is superior at amygdala and putamen volume analysis, and the new method is superior at hippocampus and thalamus volume analysis, all based on discrimination between diagnostic groups and in higher correlations with clinical data MMSE or CDR-sb.

In general, the "gold standard" method of obtaining the volumes of a brain structure on MRI scans has been considered to be the use of manual segmentation (den Heijer *et al.*, 2006; Basso *et al.*, 2006; Chupin *et al.*, 2007). Mean volumes of the HPC, obtained using the Template E Set (3.03 for the left HPC), underestimated by about 9% results obtained using manual segmentation-based approaches for HPC volumes in elderly cognitively normal subjects (Sánchez-Benavides *et al.*, 2010) (3.34 for the left HPC). Mean volumes of the HPC reported using the commercial software Neuroquant^{TM}, Freesurfer-based program (2.39 for the left HPC) underestimated by about 28%, and those using IBASPM with the MNI template (1.99 for the left HPC) underestimated by about 40% of the volumes of the left HPC obtained by manual segmentation. Nevertheless, HPC volumes obtained using the MNI Template Set are equivalent to those obtained using a variety of automated or semi-automated methods that have been reported in the literature (Teipel *et al.*, 2006 Mori *et al.*, 1997).

In this study, the automatic hippocampal area measurement on a single coronal slice (MB slice) was able to discriminate diagnostic groups and had strong correlations with clinical data. However, it is inferior to hippocampus volumetric data or VRS hippocampus scores because this measurement is the ratio of the area of hippocampus to hippocampus temporal horn on a single coronal slice. Generally speaking, in the high resolution MRI scan setting there are around 0 to 200 pixels of hippocampus and 0 to 100 pixels of hippocampus temporal horn on the MB slice. A small error in measurement will affect the RHPA ratio. Finally, the inaccuracy of choosing MB slice will also result in the error of RHPA. Using multiple slices, such as including one anterior and one posterior slice, may improve this method.

Research studies employing SPM5 or IBASPM to perform volumetric analysis have long relied on the MNI Template Set ignoring the fact that the coordinate MNI template is not from the same "source" as where the anatomical atlas AAL is defined. There usually exist a big variance between AAL and the anatomical characteristics of the to-be-segmented brain MRI, which will result in less accuracy of the segmentation. However, the results of this study suggest that a customized atlas associated with corresponding template, derived from an aged subject, may be particularly important to produce accurately automated segmentation. Another factor that may need to be taken into account for customizing atlases and templates is that the disease “states” affect the anatomy of the brain. This study demonstrated that the use of an elderly subject’s brain for creating the atlas and template for atlas-based segmentation not only improves the accuracy of measurement of the volume of the hippocampus, but also enhances the applicability for distinguishing NCI from aMCI and AD.

Another important contribution of this study is the comparison between different template sets and their resultant ROIs volumes by analyzing metrics for distinguishing between NCI and aMCI, and NCI and AD. A further way of comparing template set was to analyze the correlations of scores of cognition (MMSE) and functional ability (CDR-sb) to ROIs volumes. Atrophy of the MTL structures, such as entorhinal cortex, HPC and AMG, is an early and reliable indicator of the development of neurofibrillary pathology in the brain, characterizing of the neurodegenerative stage of Alzheimer’s disease. It has been shown in this and many previous studies that increasing severity of atrophy of the HPC and AMG is associated with the severity of cognitive and functional impairment in patients with aMCI and AD. It has been shown by this study that the measurement of HPC and AMG volume, obtained through the use of the Template E Set, resulted in better distinctions between diagnostic groups than those obtained using the Template S Set and the MNI template Set because of higher accuracy in the measurement of HPC and AMG volumes.

6.2 Conclusion

Using atlas-based segmentation, the accuracy of ROIs segmentation is dependent on: (1) correspondence of the coordinate template with the anatomical atlas; (2) deformation field estimation; (3) anatomical characteristics of the to-be-segmented brain MRI reflection in the anatomical atlas. Using manual segmentation as gold standard to validate the automated segmentation obtained through the use of three different template sets, we can concluded that the automated segmentation using an atlas-based approach associated with the template derived from the aged subject, assessing elderly normal or cognitively impaired subjects, yields the most accurate results while the least accurate results occur when the template sets are based on a young male. The reasons for the high accuracy of the Template E Set for obtaining HPC volumes are self-evident, because it is not generally recognized that the template employed for obtaining regional brain volumes should be customized so that the template can optimally approximate the anatomy of the target brain(s) to be segmented.

In summary, this study has shown that fully automated atlas-based segmentation can be customized so as to make the measurement of regional volumes more accurate for certain target groups of subjects, such as those who are elderly with degenerative diseases. We can further compare the automated segmentation, using different atlases and templates, to manual segmentation done in all the NCI, aMCI and AD subjects. Nevertheless, the results of this study show that convenient, atlas-based approaches to performing MRI volumetry can be optimized for research and clinical purposes by customizing the anatomical atlases and corresponding spatial coordinate templates, so as to account for the age and disease state of the subject to be assessed.

REFERENCES

Alemán-Gómez Y., Melie-García L., and Valdés-Hernandez P. (2006). "IBASPM: toolbox for automatic parcellation of brain structures," 12th annual meeting of the organization for human brain mapping, June 11–15. Florence, Italy. Available on CD-Rom in NeuroImage, Vol. 27, No.1

Allen J.S., Bruss J., Brown C.K. and Damasio H. (2005). "Normal neuroanatomical variation due to age: the major lobes and a parcellation of the temporal region," Neurobiol Aging. 26, 1245-1260.

Apostolova L.G., and Thompson P.M. (2007). "Brain mapping as a tool to study neurodegeneration," Neurotherapeutics 4, 387-400.

Ashburner J., Friston K.J. (1997). "Multimodal image coregistration and partitioning--a unified framework," Neuroimage 6, 209-217.

Ashburner J., Friston K.J. (1999). "Nonlinear spatial normalization using basis functions," Hum Brain Mapp 7, 254-266.

Ashburner J., and Friston K.J. 2009, Functional Imaging Voxel Based Morphometry Laboratory, London, UK Elsevier Ltd.

Assal F., and Cummings J.L. (2002). "Neuropsychiatric symptoms in the dementias," Current Opinion in Neurology 15, 445-450.

Barnes, J., Foster, J., Boyes, R.G., Pepple, T., Moore, E.K., Schott, J.M., Frost, C. (2008). "A comparison of methods for the automated calculation of volumes and atrophy rates in the hippocampus," Neuroimage 40, 1655-1671.

Barnes J., Whitwell J.L., Frost C., Josephs K.A., Rossor M., and Fox N.C. (2006). "Measurements of the amygdala and hippocampus in pathologically confirmed Alzheimer disease and frontotemporal lobar degeneration," Arch Neurol. 63, 1434-1439.

Basso M., Yang J., Warren L., MacAvoy M.G., Varma P., Bronen R.A., and van Dyck C.H. (2006). "Volumetry of amygdala and hippocampus and memory performance in Alzheimer's disease," Psychiatry Research: Neuroimaging 146, 251-261.

Bobinski M., de Leon M.J., Wegiel J., Desanti S., Convit A., Saint Louis L.A., Rusinek H., and Wisniewski H.M. (2000). "The histological validation of post mortem magnetic resonance imaging-determined hippocampal volume in Alzheimer's disease," Neuroscience 95, 721-725.

Braak H., and Braak E. (1997). "Diagnostic criteria for neuropathologic assessment of Alzheimer's disease," Neurobiol Aging 18, S85-88.

Braak H., and Braak E. (1991). “Neuropathological staging of Alzheimer-related changes,” Acta Neuropathol 82, 239-259.

Braak H., and Braak E. (1995). “Staging of Alzheimer's disease-related neurofibrillary changes,” Neurobiology of Aging 16, 271-278.

Brewer J.B., Magda S., Airriess C., and Smith M.E. (2009). “Fully-automated quantification of regional brain volumes for improved detection of focal atrophy in Alzheimer disease,” AJNR Am J Neuroradiol 30, 578-580.

Burns A., Lawlor B. and Craig S. (2002). “Rating scales in old age psychiatry,” Br. J. Psychiatry. 180, 161-167.

Carmichael O.T., Aizenstein H.A., Davis S.W., Becker J.T., Thompson P.M., Meltzer C.C., and Liu Y. (2005). “Atlas-based hippocampus segmentation in Alzheimer’s disease and mild cognitive impairment,” NeuroImage 27, 979-990.

Chao L.L., Mueller S.G., Buckley S.T., Peek K., Raptentsetseng S., Elman J., Yaffe K., Miller B.L., Kramer J.H., Madison C., Mungas D., Schuff N., and Weiner M.W. (2010). “Evidence of neurodegeneration in brains of older adults who do not yet fulfill MCI criteria,” Neurobiol Aging 31, 368-377.

Chupin M., Mukuna-Bantumbakulu A.R., Hasboun D., Bardinet E., Baillet S., Kinkingnéhun S., Lemieux L., Dubois B. and Garnero L. (2007). “Anatomically constrained region deformation for the automated segmentation of the hippocampus and the amygdala: method and validation on controls and patients with Alzheimer's disease,” Neuroimage 34, 996-1019.

Collins D.L., Holmes C., Peters T., and Evans A. (1995). “Automatic 3D model-based neuroanatomical segmentation,” Hum Brain Mapp 3, 190-208.

Collins D.L., Zijdenbos A.P., Barré W.F.C., and Evans A.C. 1999, ANIMAL +INSECT: improved cortical structure segmentation, In: Kuba A, Samal M, Todd-Pokropek A, editors. Proc. of the Annual Symposium on Information Processing in Medical Imaging. Lect Notes Comput Sci. New York: Springer; 210-223.

Colliot O., Chételat G., Chupin M., Desgranges B., Magnin B., Benali H., Dubois B., Garnero L., Eustache F. and Lehéricy S. (2008). “Discrimination between Alzheimer disease, mild cognitive impairment, and normal aging by using automated segmentation of the hippocampus,” Radiology 248, 194-201.

Crystal H., Dickson D., Fuld P., Masur D., Scott R., Mehler M., Masdeu J., Kawas C., Aronson M., and Wolfson L. (1988). “Clinico-pathologic studies in dementia: nondemented subjects with pathologically confirmed Alzheimer's disease,” Neurology 11, 1682-1687.

de Jong L.W., van der Hiele K., Veer I.M., Houwing J.J., Westendorp R.G., Bollen E.L., de Bruin P.W., Middelkoop H.A., van Buchem M.A. and van der Grond J. (2008). “Strongly reduced volumes of putamen and thalamus in Alzheimer's disease: an MRI study,” Brain 131, 3277-3285.

de Leon M.J., George A.E., Golomb J., Tarshish C., Convit A., Kluger A., De Santi S., McRae T., Ferris S.H., Reisberg B., Ince C., Rusinek H., Bobinski M., Quinn B., Miller D.C., and Wisniewski H.M. (1997). “Frequency of hippocampal formation atrophy in normal aging and Alzheimer's disease,” Neurobiol Aging 18, 1-11.

de Leon M.J., Mosconi L., Blennow K., DeSanti S., Zinkowski R., Mehta P.D., Pratico D., Tsui W., Saint Louis L.A., Sobanska L., Brys M., Li Y., Rich K., Rinne J., Rusinek H. (2007). “Imaging and CSF studies in the preclinical diagnosis of Alzheimer's disease,” Ann N Y Acad Sci. 1097, 114-145.

De Meyer G., Shapiro F., Vanderstichele H., Vanmechelen E., Engelborghs S., De Deyn P.P., Coart E., Hansson O., Minthon L., Zetterberg H., Blennow K., Shaw L. and Trojanowski J.Q. (2010). “Alzheimer's Disease Neuroimaging Initiative. Diagnosis-independent Alzheimer disease biomarker signature in cognitively normal elderly people,” Arch Neurol. 67, 949-956.

den Heijer T., Geerlings M.I., Hoebeek F.E., Hofman A., Koudstaal P.J. and Breteler M.M. (2006). “Use of hippocampal and amygdalar volumes on magnetic resonance imaging to predict dementia in cognitively intact elderly people,”. Arch Gen Psychiatry 63, 57-62.

De Santi S., de Leon M.J., Rusinek H., Convit A., Tarshish C.Y., Roche A., Tsui W.H., Kandil E., Boppana M., Daisley K., Wang G.J., Schlyer D. and Fowler J. (2001). “Hippocampal formation glucose metabolism and volume losses in MCI and AD,” Neurobiol Aging 22, 529-539.

Desikan R.S., Cabral H.J., Hess C.P., Dillon W.P., Glastonbury C.M., Weiner M.W., Schmansky N.J., Greve D.N., Salat D.H., Buckner R.L., and Fischl B. (2009). “Automated MRI measures identify individuals with mild cognitive impairment and Alzheimer's disease,” Brain 132, 2048-2057.

Devanand D.P., Liu X., Tabert M.H., Pradhaban G., Cuasay K., Bell K., de Leon M.J., Doty R.L., Stern Y. and Pelton G.H. (2008). “Combining early markers strongly predicts conversion from mild cognitive impairment to Alzheimer's disease,” Biol Psychiatry 64, 871-879.

Dice L.R. (1945). “Measure of the amount of ecological association between species,” Ecology 26, 297-302.

Duara R., Loewenstein D.A., Potter E., Appel J., Greig M.T., Urs R., Shen Q., Raj A., Small B., Barker W., Schofield E., Wu Y. and Potter H. (2008). “Medial temporal lobe atrophy on MRI scans and the diagnosis of Alzheimer disease,” Neurology 71, 1986-1992.

Duara R., Loewenstein D.A., Greig-Custo M.T., Raj A., Barker W., Potter E., Schofield E., Small B., Schinka J., Wu Y. and Potter H. (2010). “Diagnosis and staging of mild cognitive impairment, using a modification of the clinical dementia rating scale: the mCDR,” Int J Geriatr Psychiatry 25, 282-289.

Du A.T., Schuff N., Kramer J.H., Rosen H.J., Gorno-Tempini M.L., Rankin K., Miller B.L., and Weiner M.W. (2007). “Different regional patterns of cortical thinning in Alzheimer’s disease and frontotemporal dementia,” Brain 130, 1159-1166.

Duyckaerts C., Potier M.C. and Delatour B. (2008). “Alzheimer disease models and human neuropathology: similarities and differences,” Acta Neuropathol. 115, 5-38.

Fan Y., Batmanghelich N., Clark C.M., and Davatzikos C. (2008). “Alzheimer's Disease Neuroimaging Initiative. Spatial patterns of brain atrophy in MCI patients, identified via high-dimensional pattern classification, predict subsequent cognitive decline,” Neuroimage. 39, 1731-1743.

Firbank M.J., Barber R., Burton E.J. and O'Brien J.T. (2008). “Validation of a fully automated hippocampal segmentation method on patients with dementia,” Hum Brain Mapp. 29, 1442-1449.

Fischl B., Salat D., Busa E., Albert M., Dieterich M., Haselgrove C., van der Kouwe A., Killiany R., Kennedy D., Klaveness S., Montillo A., Makris N., Rosen B. and Dale A.M. (2002). “Whole brain segmentation. Automated labeling of neuroanatomical structures in the human brain,” Neuron 33, 341-355.

Folstein M., Folstein S. and McHugh P. (1975). “Mini-Mental State: a practical method for grading the cognitive state of patients for the physician,” J Psychiatr Res. 12, 189-198.

Fradinger E.A. and Bitan G. (2005). “En route to early diagnosis of Alzheimer’s disease – Are we there yet,” Trends in Biotechnology 23, 531-533.

Frisoni G.B., Scheltens P., Galluzzi S., Nobili F.M., Fox N.C., Robert P.H., Soininen H., Wahlund L.O., Waldemar G. and Salmon E. (2003). “Neuroimaging tools to rate regional atrophy, subcortical cerebrovascular disease, and regional cerebral blood flow and metabolism: consensus paper of the EADC,” J Neurol Neurosurg Psychiatry 74, 1371-1381.

Fuld P.A. 1981, Fuld Object-Memory Evaluation. Wood Dale, IL: Stoelting Co.

Galton C.J., Patterson K., Xuereb J.H. and Hodges J.R. (2000). “Atypical and typical presentations of Alzheimer's disease: a clinical, neuropsychological, neuroimaging and pathological study of 13 cases,” Brain 123, 484-498.

García-Vázquez V. Reig S., Janssen J., Pascau J., Rodriguez-Ruano A., Udias A., Chamorro J., Vaquero J.J., Desco M. (2008). “Use of IBASPM atlas-based automatic segmentation toolbox in pathological brains: effect of template selection,” Nuclear Science Symposium Conference Record, NSS '08. IEEE

Graves A.B., Mortimer J.A., Larson E.B., Wenzlow A., Bowen J.D. and McCormick W.C. (1996). “Head circumference as a measure of cognitive reserve: association with severity of impairment in Alzheimer's disease,” Br J Psychiatry 169, 86-92.

Graves A.B. 2004, Alzheimer’s Disease and Vascular Dementia, Nelson, Tanner, Van Den Eeden & McGuire (Eds). Neuroepidemiology: From Principles to Practice. New York. Oxford University Press. 102-130.

Grober E., Lipton R.B., Hall C. and Crystal H. (2000). “Memory impairment on free and cued selective reminding predicts dementia,” Neurology 54, 827-832.

Gold G., Bouras C., Canuto A., Bergallo M.F., Herrmann F.R., Hof P.R., Mayor P.A., Michel J.P. and Giannakopoulos P. (1994). “Clinicopathological validation study of four sets of clinical criteria for vascular dementia. ABlacker D, Albert MS, Bassett SS, Go RC, Harrell LE, Folstein MF. Reliability and validity of NINCDS-ADRDA criteria for Alzheimer's disease. The National Institute of Mental Health Genetics Initiative,” Arch Neurol 51, 1198-1204.

Gosche K.M., Mortimer J.A., Smith C.D., Markesbery W.R. and Snowdon D.A. (2001). “An automated technique for measuring hippocampal volumes from MR imaging studies,” AJNR Am J Neuroradiol 22, 1686-1689.

Haller, J.W., Banerjee, A., Christensen, G.E., Gado, M., Joshi, S.C., Miller, M.I., Sheline, Y.I., Vannier, M.W. and Csernansky, J.G. (1997). “Three-dimensional hippocampal MR morphometry with high-dimensional transformation of a neuroanatomical atlas,” Radiology 202, 504-510.

Hampel H., Teipel S.J., Bayer W., Alexander G.E., Schwarz R., Schapiro M.B., Rapoport S.I. and Moller H.J. (2002). “Age transformation of combined hippocampus and amygdala volume improves diagnostic accuracy in Alzheimer’s disease,” J Neurol Sci 194, 15-19.

Hansson O., Zetterberg H., Buchhave P., Londos E., Blennow K. and Minthon L. (2006). “Association between CSF biomarkers and incipient Alzheimer's disease in patients with mild cognitive impairment: a follow-up study,” The Lancet Neurology 5, 228-234.

Hasan K.M. (2009). “A questionable gold standard for hippocampus volume and asymmetry,” Neuroradiology 51, 201-202.

Hayashi T., Wada A., Uchida N. and Kitagaki H. (2009). “Enlargement of the hippocampal angle: a new index of Alzheimer disease,” Magn Reson Med Sci. 8, 33-38.

Heckemann R.A., Hajnal J.V., Aljabar P., Rueckert D. and Hammers A. (2006). “Automatic anatomical brain MRI segmentation combining label propagation and decision fusion,” Neuroimage 33, 115-126.

Hogervorst E., Bandelow S., Combrinck M., Irani S.R. and Smith A.D. (2003). “The validity and reliability of 6 sets of clinical criteria to classify Alzheimer's disease and vascular dementia in cases confirmed post-mortem: added value of a decision tree approach,” Dement Geriatr Cogn Disord 16, 170-180.

Howieson D.B., Dame A., Camicioli R., Sexton G., Payami H. and Kaye J.A. (1997). “Cognitive markers preceding Alzheimer's dementia in the healthy oldest old,” J Am Geriatr Soc 45, 584-589.

Ishii K., Soma T., Kono A.K., Sasaki H., Miyamoto N., Fukuda T. and Murase K. (2006). “Automatic volumetric measurement of segmented brain structures on magnetic resonance imaging,” Radiat Med. 24, 422-430.

Jack C.R., Dickson D.W., Parisi J.E., Xu Y.C., Cha R.H., O'Brien P.C., Edland S.D., Smith G.E., Boeve B.F., Tangalos E.G., Kokmen E. and Petersen R.C. (2002). “Antemortem MRI findings correlate with hippocampal neuropathology in typical aging and dementia,” Neurology 58, 750-757.

Jack C.R. Jr, Shiung M.M., Gunter J.L., O’Brien P.C., Weigand S.D., Knopman D.S., Boeve B.F., Ivnik R.J., Smith G.E., Cha R.H., Tangalos E.G. and Petersen R.C. (2004). “Comparison of different MRI brain atrophy rate measures with clinical disease progression in AD,” Neurology 62, 591-600.

Jack C.R. Jr, Weigand S.D., Shiung M.M., Przybelski S.A., O'Brien P.C., Gunter J.L., Knopman D.S., Boeve B.F., Smith G.E. and Petersen R.C. (2008). “Atrophy rates accelerate in amnestic mild cognitive impairment,” Neurology 70, 1740-1752.

Jarvenpaa T., Laakso M.P., Rossi R., Koskenvuo M., Kaprio J., Raiha I., Kurki T., Laine M., Frisoni G.B. and Rinne J.O. (2004). “Hippocampal MRI volumetry in cognitively discordant monozygotic twin pairs,” J Neurol Neurosurg Psychiatry 75, 116-120.

Julkunen V., Niskanen E., Muehlboeck S., Pihlajamäki M., Könönen M., Hallikainen M., Kivipelto M., Tervo S., Vanninen R., Evans A. and Soininen H. (2009). “Cortical thickness analysis to detect progressive mild cognitive impairment: a reference to Alzheimer's disease,” Dement Geriatr Cogn Disord 28, 404-412.

Kantarci K., Petersen R.C., Przybelski S.A., Weigand S.D., Shiung M.M., Whitwell J.L., Negash S., Ivnik R.J., Boeve B.F., Knopman D.S., Smith G.E. and Jack C.R. Jr. (2008). “Hippocampal volumes, proton magnetic resonance spectroscopy metabolites, and cerebrovascular disease in mild cognitive impairment subtypes,” Arch Neurol. 65, 1621-1628.

Karas G., Sluimer J., Goekoop R., van der Flier W., Rombouts S.A., Vrenken H., Scheltens P., Fox N. and Barkhof F. (2008). “Amnestic mild cognitive impairment: structural MR imaging findings predictive of conversion to Alzheimer disease,” AJNR Am J Neuroradiol 29, 944-949.

Khachaturian Z.S. (1985). “Diagnosis of Alzheimer's disease,” Arch Neurol. 42, 1097-1105.

Klein A., Andersson J., Ardekani B.A., Ashburner J., Avants B., Chiang M.C., Christensen G.E., Collins D.L., Gee J., Hellier P., Song J.H., Jenkinson M., Lepage C., Rueckert D., Thompson P., Vercauteren T., Woods R.P., Mann J.J. and Parsey R.V. (2009). “Evaluation of 14 nonlinear deformation algorithms applied to human brain MRI registration,” Neuroimage 46, 786-802.

Klein, S., van der Heide, U.A., Lips, I.M., van Vulpen, M., Staring, M., Pluim, J.P., (2008). Automatic segmentation of the prostate in 3D MR images by atlas matching using localized mutual information. Med. Phys. 35, 1407-1417.

Kordower J.H., Chu Y., Stebbins G.T., DeKosky S.T., Cochran E.J., Bennett D. and Mufson E.J. (2001). “Loss and atrophy of layer II entorhinal cortex neurons in elderly people with mild cognitive impairment,” Ann Neurol 49, 202-213.

Kovacevic S., Rafii M.S. and Brewer J.B. (2009). “Alzheimer's Disease Neuroimaging Initiative. High-throughput, fully automated volumetry for prediction of MMSE and CDR decline in mild cognitive impairment,” Alzheimer Dis Assoc Disord 23, 139-145.

Kraepelin E. 1910, Psychiatrie. Ein Lehrbuch für Studierende und Ärzte. II. Band, Klinische Psychiatrie, Johann Ambrosius Barth, Leipzig

Kramer J.H., Schuff N., Reed B.R., Mungas D., Du A.T., Rosen H.J., Jagust W.J., Miller B.L., Weiner M.W. and Chui H.C. (2004). “Hippocampal volume and retention in Alzheimer's disease,” J Int Neuropsychol Soc. 10, 639-643.

Krasuski J.S., Alexander G.E., Horwitz B., Daly E.M., Murphy D.G., Rapoport S.I. and Schapiro M.B. (1998). “Volumes of medial temporal lobe structures in patients with Alzheimer's disease and mild cognitive impairment (and in healthy controls),” Biol Psychiatry 43, 60-68.

Kukull W.A., Larson E.B., Reifler B.V., Lampe T.H., Yerby M.S. and Hughes J.P. (1990). “The validity of 3 clinical diagnostic criteria for Alzheimer's disease,” Neurology 40, 1364-1369.

Lacritz L.H., Cullum C.M., Weiner M. and Rosenberg R.N. (2001). “Comparison of the hopkins verbal learning test-revised to the California verbal learning test in Alzheimer's disease,” Appl Neuropsychol 8, 180-184.

Laurent B, Dubois B. (2006), “The SFN International Meeting Alzheimer's Disease and Dementia,” Rev Neurol (Paris) 162, 899-900.

Lehéricy S., Marjanska M., Mesrob L., Sarazin M. and Kinkingnehun S. (2007). “Magnetic resonance imaging of Alzheimer's disease,” Eur Radiol. 17, 347-362.

Leverenz J.B. and Raskind M.A. (1998). “Early amyloid deposition in the medial temporal lobe of young Down syndrome patients: a regional quantitative analysis,” Exp Neurol. 150, 296-304.

Loewenstein D.A., Barker W.W., Harwood D.G., Luis C., Acevedo A., Rodriguez I. and Duara R. (2000). “Utility of a modified mini-mental state examination with extended delayed recall in screening for mild cognitive impairment and dementia among community dwelling elders,” Int J Geriatr Psychiatry 15, 434-440.

Manly J.J., Touradji P, Tang MX, Stern Y. (2003), “Literacy and memory decline among ethnically diverse elders,” J Clin Exp Neuropsychol 25, 680-689.

McGeer EG, McGeer PL. (2001), “Innate immunity in Alzheimer's disease: a model for local inflammatory reactions,” Molecular Interventions 1, 22-29.

Mayer-Gross W., Slater E., Roth N. 1969, Clinical Psychiatry. 2nd edn., Tindall & Carsell, London.

McKhann G., Drachman D., Folstein M., Katzman R., Price D., Stadlan E.M. (1984). “Clinical diagnosis of Alzheimer’s disease: report of the NINCDS-ADRDA Work Group under the auspices of the Department of Health and Human Services Task Force on Alzheimer’s disease,” Neurology 34, 939-944.

Miller A.K.H., Alston R.L. and Corsellis J.A.N. (1980). “Variation with age in the volumes of grey and white matter in the cerebral hemispheres,” Neuropath Appl Neurobiol 6, 119-132.

Mirra S.S., Heyman A., McKeel D., Sumi S.M., Crain B.J., Brownlee L.M., Vogel F.S., Hughes J.P., van Belle G. and Berg L. (1991). “The Consortium to Establish a Registry for Alzheimer's Disease (CERAD). Part II. Standardization of the neuropathologic assessment of Alzheimer's disease,” Neurology 41, 479-486.

Morey R.A., Petty C.M., Xu Y., Hayes J.P., Wagner H.R. 2nd, Lewis D.V., LaBar K.S., Styner M. and McCarthy G. (2009). "A comparison of automated segmentation and manual tracing for quantifying hippocampal and amygdala volumes," Neuroimage 45, 855-866.

Mori E., Yoneda Y., Yamashita H., Hirono N., Ikeda M. and Yamadori A. (1997). "Medial temporal structures relate to memory impairment in Alzheimer's disease: an MRI volumetric study," J Neurol Neurosurg Psychiatry 63, 214-221.

Mortimer J.A., Snowdon D.A. and Markesbery W.R. (2003). "Head circumference, education and risk of dementia: findings from the Nun Study," J Clin Exp Neuropsychol 25, 671-679.

Mosconi L., Brys M., Glodzik-Sobanska L., De Santi S., Rusinek H. and de Leon M.J. (2007). "Early detection of Alzheimer's disease using neuroimaging," Exp Gerontol. 42, 129-138.

Müller M.J., Greverus D., Dellani P.R., Weibrich C., Wille P.R., Scheurich A., Stoeter P. and Fellgiebel A. (2005). "Functional implications of hippocampal volume and diffusivity in mild cognitive impairment," Neuroimage 28, 1033-1042.

Nagy Z., Esiri M.M., Hindley N.J., Joachim C., Morris J.H., King E.M., McDonald B., Litchfield S., Barnetson L., Jobst K.A. and Smith A.D. (1998). "Accuracy of clinical operational diagnostic criteria for Alzheimer's disease in relation to different pathological diagnostic protocols," Dement Geriatr Cogn Disord 9, 219-226.

Pantel J., Schroder J., Schad L.R., Friedlinger M., Knopp M.V., Schmitt R., Geissler M., Bluml S., Essig M. and Sauer H. (1997). "Quantitative magnetic resonance imaging and neuropsychological functions in dementia of the Alzheimer type," Psychol Med. 27, 221-229

Peters F., Collette F., Degueldre C., Sterpenich V., Majerus S. and Salmon E. (2009). "The neural correlates of verbal short-term memory in Alzheimer's disease: an fMRI study," Brain 132, 1833-1846.

Petersen R.C., Smith G.E., Waring S.C., Ivnik R.J., Tangalos E. and Kokmen E. (1999). "Mild Cognitive Impairment: clinical characterization and outcome," Arch Neurol 56, 303-308.

Petersen RC, Morris JC. 2003, Clinical features. In: RC Petersen edn. Mild cognitive impairment: Aging to Alzheimer's disease. New York: Oxford University Press, 15-39.

Petersen R.C. (2004). "Mild cognitive impairment as a diagnostic entity," J Intern Med. 256, 183-194.

Petrella J.R., Coleman R.E. and Doraiswamy P.M. (2003). “Neuroimaging and early diagnosis of Alzheimer disease: A look to the future,” Radiology 226, 315-336.

Pope S.K., Shue V.M. and Beck C. (2003). “Will a healthy lifestyle help prevent Alzheimer's disease?” Annu Rev Public Health 24, 111-132.

Rodionov R., Chupin M., Williams E., Hammers A., Kesavadas C. and Lemieux L. (2009). “Evaluation of atlas-based segmentation of hippocampi in healthy humans,” Magn Reson Imaging 27, 1104-1109.

Rueckert D., Sonoda L.I., Hayes C., Hill D.L.G., Leach M.O. and Hawkes D.J. (1999). “Nonrigid registration using free-form deformations: Application to breast mr images," IEEE Tr.Med. Im. 18, 712-720.

Salamon G., Salamon N., Johnson N., Mongkolwat P., Gitelman D., Weintraub S., Mesulam M. and Russell E. (2004). “Magnetic resonance studies in Alzheimer's dementia. What routine scanning shows,” Rev Neurol (Paris) 160, 63-73.

Sánchez-Benavides G., Gómez-Ansón B., Sainz A., Vives Y., Delfino M. and Peña-Casanova J. (2010). “Manual validation of FreeSurfer's automated hippocampal segmentation in normal aging, mild cognitive impairment, and Alzheimer Disease subjects,” Psychiatry Res 181, 219-225.

Scheltens P., Launer L.J., Barkhof F., Weinstein H.C. and van Gool W.A. (1995). “Visual assessment of medial temporal lobe atrophy on magnetic resonance imaging: interobserver reliability,” J Neurol. 242, 557-560.

Schneider J.A., Wilson R.S., Bienias J.L., Evans D.A. and Bennett D.A. (2004). “Cerebral infarctions and the likelihood of dementia from Alzheimer disease pathology,” Neurology 62, 1148-1155.

Schofield P.W., Mosesson R.E., Stern Y. and Mayeux R. (1995). "The age at onset of Alzheimer's disease and an intracranial area measurement. A relationship,” Arch Neurol 52, 95-98.

Seixas F.L., Saade D.C.M, Conci A., de Souza A.S., Tovar-Moll F. and Bramatti I. (2010). “Anatomical brain MRI segmentation methods: volumetric assessment of the hippocampus,” IWSSIP 2010-17th International Conference on Systems, Signals and Image Processing. 247-250.

Shen Q., Loewenstein D., Potter E., Zhao W., Appel J., Greig M., Raj A., Acevedo A., Schofield E., Barker W., Wu Y., Potter H. and Duara R. (2011a). “Volumetric and visual rating of MRI scans in the diagnosis of amnestic MCi and Alzheimer’s Disease,” Alzheimers Dement. In press.

Shen Q., Zhao W., Loewenstein D., Potter E., Greig M., Raj A., Barker W., Potter H., Duara R. (2011b). “Comparing new templates and atlas-based segmentations in the volumetric analysis of brain MRIs for diagnosing Alzheimer’s disease,” Alzheimers Dement. Under review.

Silverman W., Wisniewski H.M., Bobinski M. and Wegiel J. (1997). “Frequency of stages of Alzheimer-related lesions in different age categories,” Neurobiol Aging18, 377-379.

Small B.J, Mobly J.L., Laukka E.J., Jones S. and Backman L. (2003). “Cognitive deficits in preclinical Alzheimer's disease,” Acta Neurol Scand Suppl. 179, 29-33.

Snowdon D.A., Greiner L.H., Mortimer J.A., Riley K.P., Greiner P.A., Markesbery W.R. (1997). “Brain infarction and the clinical expression of Alzheimer disease,” The Nun Study. JAMA 277, 813-817.

Sperling, R., (2007). “Functional MRI studies of associative encoding in normal aging, mild cognitive impairment, and Alzheimer’s disease,” Ann. N. Y. Acad. Sci. 1097, 146-155.

Stern Y., Gurland B., Tatemichi T.K., Tang M.X., Wilder D. and Mayeux R. (1994). “Influence of education and occupation on the incidence of Alzheimer's disease,” JAMA 271, 1004-1010.

Stern Y. (2003). “The concept of cognitive reserve: a catalyst for research,” J Clin Exp Neuropsychol. 25, 589-593.

Tae W.S., Kim S.S., Lee K.U., Nam E.C. and Kim K.W. (2008). “Validation of hippocampal volumes measured using a manual method and two automated methods (FreeSurfer and IBASPM) in chronic major depressive disorder,” Neuroradiology 50, 569-581.

Tapiola T., Pennanen C., Tapiola M., Tervo S., Kivipelto M., Hänninen T., Pihlajamäki M., Laakso M.P., Hallikainen M., Hämäläinen A., Vanhanen M., Helkala E.L., Vanninen R., Nissinen A., Rossi R., Frisoni G.B. and Soininen H. (2008). “MRI of hippocampus and entorhinal cortex in mild cognitive impairment: a follow-up study,” Neurobiol Aging 29, 31-38.

Tatemichi T.K., Desmond D.W., Stern Y., Paik M., Sano M. and Bagiella E. (1994). “Cognitive impairment after stroke: frequency, patterns, and relationship to functional abilities,” J Neurol Neurosurg Psychiatry 57, 202-207.

Teipel S.J., Pruessner J.C., Faltraco F., Born C., Rocha-Unold M., Evans A., Möller H.J. and Hampel H. (2006). “Comprehensive dissection of the medial temporal lobe in AD: measurement of hippocampus, amygdala, entorhinal, perirhinal and parahippocampal cortices using MRI,” J Neurol. 253, 794-800.

Tzourio-Mazoyer N., Landeau B., Papathanassiou D., Crivello F., Etard O., Delcroix N., Mazoyer B. and Joliot M. (2002). “Automated anatomical labelling of activations in spm using a macroscopic anatomical parcellation of the MNI MRI single subject brain,” Neuroimage 15, 273-289.

Uotani C., Sugimori K. and Kobayashi K. (2006). “Association of minimal thickness of the medial temporal lobe with hippocampal volume, maximal and minimal hippocampal length: volumetric approach with horizontal magnetic resonance imaging scans for evaluationof a diagnostic marker for neuroimaging of Alzheimer’s disease,” Psychiatry Clin Neurosci. 60, 319-326.

Urs R. 2006, Visual and Semi Automated Rating Systems to detect Mild Cognitive Impairment and Alzheimer’s disease. Master thesis

Urs R., Potter E., Barker W., Appel J., Loewenstein D.A., Zhao W. and Duara R. (2009). “Visual rating system for assessing magnetic resonance images: a tool in the diagnosis of mild cognitive impairment and Alzheimer disease,” J Comput Assist Tomogr. 33, 73-78.

van der Lijn F., den Heijer T., Breteler M.M. and Niessen W.J. (2008). “Hippocampus segmentation in MR images using atlas registration, voxel classification, and graph cuts,” NeuroImage 43, 708-720.

Wu M., Rosano C., Lopez-Garcia P., Carter C.S., Aizenstein H.J. (2007). “Optimum template selection for atlas-based segmentation,” Neuroimage 34, 1612-1618.

Xu W., Qiu C., Winblad B. and Fratiglioni L. (2007). “The effect of borderline diabetes on the risk of dementia and Alzheimer’s disease,” Diabetes 56, 211-216.

Zamrini E., De Santi S., and Tolar M. (2004). “Imaging is superior to cognitive testing for early diagnosis of Alzheimer's disease,” Neurobiol Aging 25, 685-691.

Zola-Morgan S., Squire L.R., Amaral D.G. and Suzuki W.A. (1989). “Lesions of perirhinal and parahippocampal cortex that spare the amygdala and hippocampal formation produce severe memory impairment,” J Neurosci. 9, 4355-4370.

Zola-Morgan S., Squire L.R., Clower R.P. and Rempel N.L. (1993). “Damage to the perirhinal cortex exacerbates memory impairment following lesions to the hippocampal formation,” J Neurosci. 13, 251-265.